Atomic Conformational Dynamics and Actin-Crosslinking Function of Alpha-Actinin Revealed by SimHS-AFMfit

Kien Xuan Ngo[1,5,6,*], Takashi Sumikama[1, 6,*], Rémi Vuillemot[2,*], Han Gia Nguyen[1], Taro QP Uyeda[3], Ngan Thi Phuong Le[4], Sergei Grudinin[2,*]

[1]Nano Life Science Institute (WPI-NanoLSI), Kanazawa University, Kanazawa, Japan.

[2]Univ. Grenoble Alpes, CNRS, Grenoble INP, LJK, 38000 Grenoble, France.

[3]Faculty of Advanced Science and Engineering, Waseda University, Shinjuku, Japan.

[4]Center for Bioscience and Biotechnology, University of Science, Vietnam National University, Ho Chi Minh City, Vietnam

[5]Lead contact

[6]These authors contributed equally.

*Corresponding author: Kien Xuan Ngo, Takashi Sumikama, Rémi Vuillemot, Sergei Grudinin

Email:

ngoxuankien@staff.kanazawa-u.ac.jp (K.X.N.)

sumi@staff.kanazawa-u.ac.jp (T.S.)

remi.vuillemot@univ-grenoble-alpes.fr (R.V.)

sergei.grudinin@univ-grenoble-alpes.fr (S.G.)

31 **Graphical Abstract**

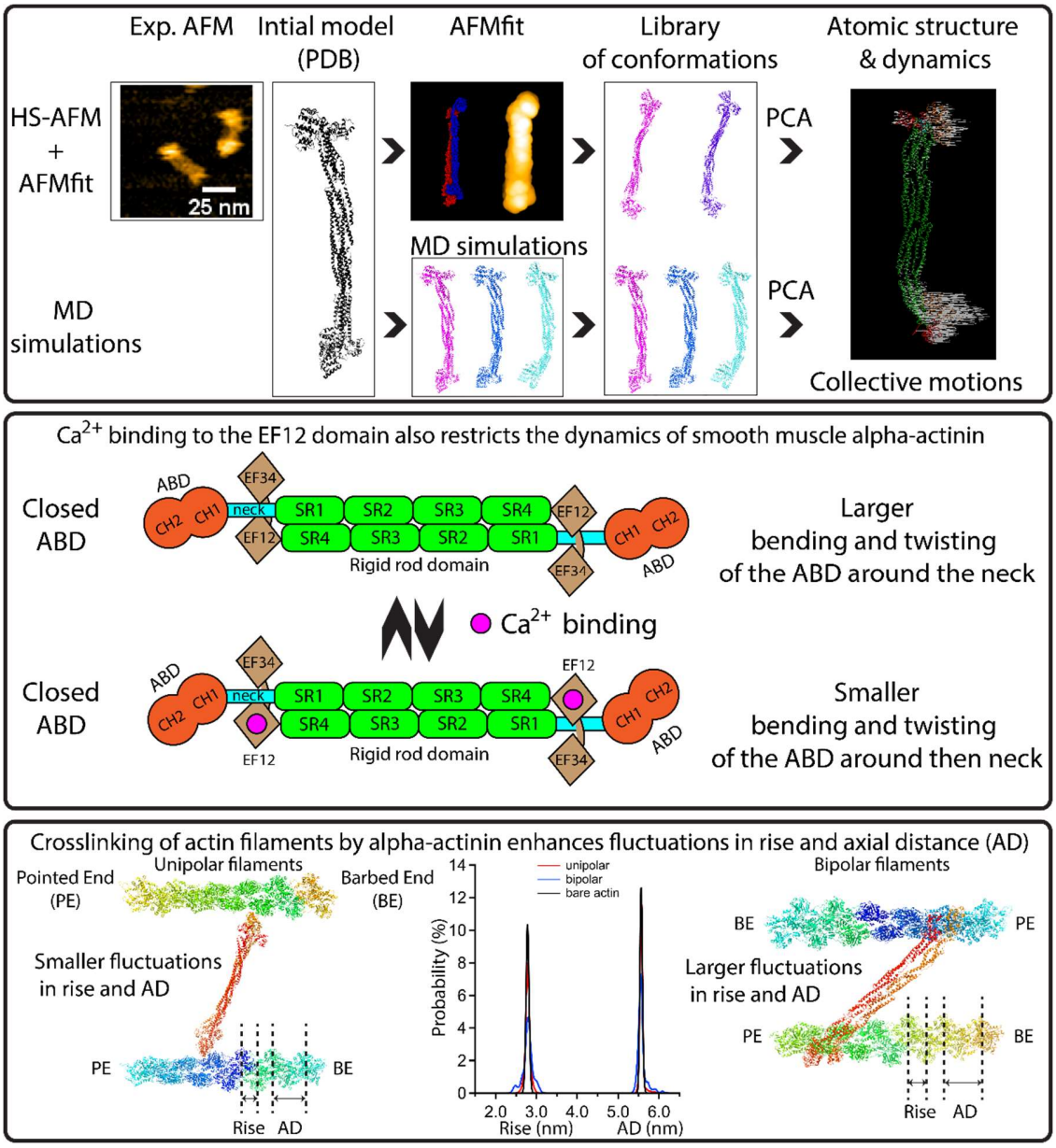

32

33

34

35

36

37

38

Summary

Alpha-actinin is a crucial actin-binding protein involved in cellular functions like muscle contractility, mechanosensation, and cell division. Studying its atomic structure and dynamics is challenging due to protein complexity and imaging limitations. To address this, we developed **SimHS-AFMfit**, integrating high-speed AFM (HS-AFM), AFMfit (a flexible fitting technique), and molecular dynamics (MD) simulations. This approach successfully converted 2D AFM images into 3D atomic conformations, revealing the atomic conformational dynamics of Ca^{2+}-bound and unbound alpha-actinin. Using principal component analysis, we classified and quantified protein motions such as twisting and bending. HS-AFM and MD simulations further characterized the fluctuations of rise and axial distance (AD) between adjacent protomers in actin filament crosslinking models, identifying structural features that regulate myosin II and cofilin binding. These findings enhance our understanding of alpha-actinin's role in actin filament modulation and provide insights for studying more complex protein assemblies, such as contractile rings.

Keywords:

Alpha-actinin, Actin, Cofilin, Myosin II, unipolar-bipolar crosslinking, HS-AFM, AFMfit, MD Simulations, SimHS-AFMfit, PCA.

Introduction

Alpha-actinin is a key protein in the organization of the actin cytoskeleton and is crucial for maintaining the mechanical properties of cells. In humans, alpha-actinin isoforms 2 and 3, which are believed to be Ca^{2+} insensitive, are integral to the function of striated muscle and are regulated by phosphoinositides[1–6]. In contrast, non-muscle alpha-actinin isoforms 1 and 4 are Ca^{2+}-sensitive[7–9]. Previous studies have elucidated the atomic structure of these muscle and non-muscle alpha-actinin isoforms via techniques such as X-ray scattering[7–9]; however, these methods often fail to capture the dynamic conformational changes of these molecules. An understanding of these changes is crucial for elucidating the role of alpha-actinin in actin filament crosslinking and the associated structural changes under unipolar and bipolar crosslinking states.

Actin is one of the most highly conserved eukaryotic proteins; when formed into filaments, actin plays a crucial role in various cellular processes, including morphogenesis, motility, division, intracellular transport, and membrane deformation in the cytosol[10]. These filaments also contribute to the nuclear functions such as transcriptional regulation, chromatin remodeling, and DNA repair[11]. Consequently, a key goal in biology and biophysics is to elucidate the molecular mechanisms governing the functional differentiation of the actin filaments within the cells. Actin filaments are right-handed helices, and their subunits are arranged in a way that generates two distinct pitches: a major pitch and a minor pitch. The major pitch represents the overall helical turn or a half helix of the filament and spans approximately 36 nm or approximately 13 subunits (6.5 protomer pairs) in the canonical actin filament[12–17]. The minor pitch, on the other hand, refers to the smaller, localized helical twist between adjacent G-actin subunits within one turn of the major helix and is approximately 5.5 nm[13–16]. These two structural features are fundamental to the establishment of the mechanical properties of the actin filaments[18,19], influencing their flexibility and stability[20,21]. Moreover, they play essential roles in regulating the binding interactions of proteins such as cofilin and myosin II, V, debrin, fimbrin, and Rng2-CHD[17,22–31].

The primary challenge in studying protein dynamics at atomic resolutions in real time using atomic force microscopy (AFM) lies in bridging gaps at the temporal and spatial scales. While high-speed AFM (HS-AFM) can capture the dynamics of the two-dimensional (2D) surface structures of proteins with optimal performance in just a few tens of milliseconds (~20 ms/frame) and at nanometer scales (1 nm in the x–y plane; ~0.1 nm in the z–direction)[22,25,32–38], conventional molecular dynamics (MD) simulations typically explore atomic structures over much shorter time scales, from femtoseconds to microseconds[39–41]. Protein dynamics span a wide range of temporal scales (fs-μs), reflecting movements from atomic vibrations to molecular tumbling and larger collective motions that can be observed with nuclear magnetic resonance (NMR)[42,43] and MD simulations[40,44–48]. However, HS-AFM is particularly valuable for investigating slower processes, such as protein folding and conformational changes induced by drugs or protein interactions, which occur over temporal scales ranging from milliseconds to seconds. Traditional MD simulations face challenges in modeling large and complex biological systems because of computational constraints. However, recent advancements have substantially extended their capabilities, allowing the simulation of larger biomolecular systems over longer timescales[49–52]. HS-AFM complements these advancements by enabling high-speed imaging of complex protein surface structures and dynamics and provides detailed insights into their functional activities[53]. NMR can simultaneously resolve the atomic structures and interactional dynamics but remains limited by the protein size, even with recent advancements in in-cell NMR. AFMfit utilizes an iterative fitting process that progressively modifies an input 3D atomic model (e.g., those obtained from a protein data bank, PDB or models from MD simulations) to match the 2D molecular surface images captured from multiple experimental AFM observations. AFMfit mutually explores the rigid and flexible degrees of freedom via the fast Fourier transform (FFT) and the nonlinear rigid block normal-mode analysis (NOLB-NMA) methods, respectively[54–56]. Overcoming the discrepancies in temporal and spatial resolution between the experimental AFM data and simulation data would enable

120 a thorough comparison of these two types of data in dynamic atomic structural
121 biology.
122 In this study, our goal was to explore the atomic conformational dynamics and
123 actin-crosslinking function of alpha-actinin through a multidimensional approach.
124 Thus, we developed an innovative workflow (SimHS-AFMfit) to transform the 2D
125 AFM images into three-dimensional (3D) atomic conformations by integrating HS-
126 AFM with the normal mode-based flexible fitting algorithm AFMfit[57] and MD
127 simulations[40,44–46]; this strategy partially bridges the spatial and temporal gaps
128 between the experimental AFM data and MD simulations. This enabled the
129 interpretation of the HS-AFM data with the 3D atomic models and overcame the
130 limitations of direct visualization techniques. MD simulations have extended our
131 understanding of protein dynamics by capturing atomic structural transitions on the
132 nanosecond timescale, providing complementary insights into molecular flexibility
133 and stability[58].
134 To validate our methodology, we applied it to smooth muscle alpha-actinin, which
135 is a key cytoskeletal protein that plays a crucial role in crosslinking actin filaments
136 and interacts with other regulatory proteins. We examined the atomic structure and
137 conformational changes of alpha-actinin in both the Ca^{2+}-bound and Ca^{2}-unbound
138 states. To expand our understanding of the general role of alpha-actinin in the
139 dynamics and function of muscle, stress fibers, and contractile rings, we applied
140 our methodology to actin filaments crosslinked with and without alpha-actinin.
141 Specifically, we aimed to use our approach to investigate (i) the contribution of
142 alpha-actinin to the spatial organization of the actin filament protomers and their
143 conformational changes and (ii) the interactions between the actin filaments and
144 alpha-actinin and regulatory proteins such as the myosin II head (S1) and cofilin in
145 the unipolar and bipolar crosslinking models.
146 Our SimHS-AFMfit was used to quantify the flexibility and domain motions of
147 alpha-actinin across various conformations, including twisting, bending, and
148 rotation motions in alpha-actinin. HS-AFM and MD simulations were also used to
149 explore the atomic conformations of the actin filaments in unipolar and bipolar

150 crosslinking models and further elucidated the role of alpha-actinin in regulating
151 the binding of S1 and cofilin in solutions containing ATP and with or without Ca^{2+},
152 which mimic the minimal system of sarcomeres, stress fibers, and contractile
153 rings[59–64]. The key findings included the fluctuations in the rise and AD of the actin
154 protomers in unipolar and bipolar crosslinking models, and residue–contact maps
155 were attained. Ultimately, we aimed to improve our understanding of the biological
156 roles of alpha-actinin and actin filament in muscle, stress fibers, contractile rings,
157 and focal adhesions, including their functions in unipolar and bipolar crosslinking
158 models; their physical impacts when interacting with actin regulatory proteins such
159 as cofilin and myosin II; and their contributions to cellular mechanics, with broader
160 implications for cytoskeletal research.
161

162 **Results**

163 **Overview of the methodology for integrating HS-AFM with AFMfit and MD**
164 **simulations**

165 The focus of this study was to understand how proteins change their atomic
166 structure and how these conformational changes are related to their functions.
167 Equally crucial, however, is understanding the protein dynamics, such as folding
168 and interaction processes since these processes directly influence the biological
169 roles of proteins. HS-AFM can provide insights into the dynamic structural changes
170 in proteins during their functional processes in solution[53,65,66]. While it has high
171 temporal resolution, HS-AFM lacks the atomic spatial resolution of cryo-electron
172 microscopy (cryo-EM). Therefore, one of the major challenges with AFM lies in
173 interpreting its low-resolution, 2D surface images into detailed 3D atomic
174 conformations.
175 The innovative aspect of this research lies in the combination of three methods:
176 HS-AFM, AFMfit (a method for fitting AFM images), and MD simulations to create
177 SimHS-AFMfit (**Figure 1**). By integrating these techniques, we can achieve a more
178 comprehensive view of the 3D atomic structure of proteins and their dynamic
179 changes during their functional activities.

180 Our methodology was used to analyze the conformational changes in the Ca^{2+}-
181 bound and Ca^{2+}-unbound alpha-actinin over milliseconds to seconds and to
182 determine the atomic conformational dynamics of this protein. Alpha-actinin is an
183 antiparallel homodimer with a molecular weight exceeding 200 kDa. In the domain
184 composition and structure of chicken gizzard smooth muscle alpha-actinin (PDB:
185 1SJJ)[6], alpha-actinin consist of the following: an N-terminal actin binding domain
186 (ABD), in which the two calponin homology 1 and 2 (CH1, CH2) domains are in
187 extensive contact; a central region containing four spectrin-like repeat (SR1-SR4)
188 or rod domains; and a C-terminal calmodulin-like domain (CaMD) that includes two
189 pairs of EF-hand motifs (EF12 and EF34), and the EF12 domain is responsible for
190 Ca^{2+} binding. The two ABDs undergo a 90-degree rotation, enabling alpha-actinin
191 to crosslink the actin filaments in nearly any orientation[6] (**Figure 1A, B**).
192 We used SimHS-AFMfit to generate libraries of atomic models in different
193 conformations for both Ca^{2+}-bound and Ca^{2+}-unbound alpha-actinin through a
194 workflow (**Figure 1C**); this provided insights into their atomic structures and
195 collective motions over time. First, alpha-actinin molecules were gently
196 immobilized on mica, and AFM data were collected with a typical imaging rate of
197 100 ms per frame. We then processed the HS-AFM videos with AFMfit, starting
198 with a reference atomic model derived from the MD simulations. Specifically,
199 AFMfit fit this reference model to the experimental AFM data by generating
200 pseudo-AFM images derived from this reference model over two fitting steps. The
201 first step was a rigid fitting step in which the reference model was rigidly aligned
202 with the AFM experimental data to obtain an optimal pose using an exhaustive
203 search algorithm based on the FFT. In the second flexible fitting step, the aligned
204 models were flexibly deformed using the NOLB technique[54] to obtain the optimal
205 elastic alignment of the atomic models to multiple AFM observations. By applying
206 this iterative process to our alpha-actinin AFM data, we obtained the corresponding
207 conformational libraries for the protein (see the Supplementary Methods).
208 Simultaneously, the same initial protein model (PDB: 1SJJ)[6] was used as the
209 starting point for the MD simulations (see the Supplementary Methods); these were

210 conducted over a timescale of 500 nanoseconds and similarly produced a set of
211 conformation libraries for alpha-actinin.
212 Both the AFMfit and MD simulation-based atomic conformations were then
213 analyzed with principal component analysis (PCA); this enabled the interpretation
214 of these conformational ensembles as the conformational dynamics of the atomic
215 structure of the protein, surpassing X-ray scattering and cryo-EM methods.

216 **Ca^{2+} binding affects smooth muscle alpha-actinin length flexibility**

217 First, we employed state-of-the-art HS-AFM to obtain high spatiotemporal
218 resolution images of alpha-actinin. Two-dimensional molecular surface images of
219 the individual Ca^{2+}-bound and Ca^{2+}-unbound alpha-actinin molecules on mica
220 were continuously recorded under near-physiological conditions at an imaging rate
221 of 100 ms per frame (**Figure 2, Video S1**). To distinguish the conformational
222 dynamics between these two states, we tracked the positions (x, y, and z
223 coordinates) of the two ABD spheres on opposite sides of multiple alpha-actinin
224 molecules over sequential frames and calculated the distance between their peak
225 heights (Pseudo AFM alpha-actinin-PDB: 1SJJ in **Figures 1B, 2A, 2B**). HS-AFM
226 revealed that the length flexibility of alpha-actinin decreased in the presence of
227 Ca^{2+} compared with its absence. From the 2D HS-AFM dataset, the mean ± SD
228 heights and lengths were 6.3 ± 0.9 nm (N = 7236) and 25.2 ± 2.3 nm (N = 3516)
229 for Ca^{2+}-bound alpha-actinin and 5.5 ± 0.8 nm (N = 4043) and 25.6 ± 3.6 nm (N =
230 2016) for Ca^{2+}-unbound alpha-actinin. The results revealed statistically significant
231 differences ($p < 0.05$) in the height and length distributions between the Ca^{2+}-
232 bound and Ca^{2+}-unbound alpha-actinin (**Figure 2C**).
233 The HS-AFM data in **Figure 2C** were compared with those obtained by the AFMfit
234 and MD simulations (**Figure 2D, Table S1**). From the 3D AFMfit dataset, the
235 lengths were 24.7 ± 0.9 nm (N = 1466) for Ca^{2+}-bound and 25.2 ± 1.4 nm (N =
236 1140) for Ca^{2+}-unbound alpha-actinin. Similarly, in the 3D MD simulation dataset,
237 the corresponding values were 25.4 ± 0.6 nm (N = 500) for the Ca^{2+}-bound alpha-
238 actinin and 24.1 ± 0.7 nm (N = 500) for the unbound alpha-actinin (**Figure 2D**).
239 Specifically, the Ca^{2+}-bound state yielded a narrower distribution of length,

240 indicating that the binding of Ca^{2+} to the EF12 domain constrained the molecular
241 dynamics of alpha-actinin. The length distributions obtained from the AFMfit and
242 MD simulations were noticeably similar (**Figure 2D**); these results supported the
243 reliability of SimHS-AFMfit, despite their narrower distributions when compared
244 directly with the 2D HS-AFM data.

245 **HS-AFM analysis of the structures of the unipolar actin filaments crosslinked**
246 **with alpha-actinin in the presence or absence of S1 or cofilin**

247 Having demonstrated the positional distributions of alpha-actinin in the bound and
248 unbound states with Ca^{2+}, we next employed HS-AFM to capture the changes in
249 the structure of the unipolar crosslinking model in the presence of S1, ATP, and
250 $CaCl_2$ (**Figures 3, S1, Video S2**). The unipolar crosslinking configuration, in which
251 the actin filaments shared the same polarity (**Table S2**), was identified by
252 examining the persistent binding of S1 to the actin filaments; the persistent binding
253 occurred when ATP was gradually depleted and was explained in captions **Figure**
254 **S1B** and **Video S2**[3,22,67]. Our semiautomatic method was previously developed to
255 precisely measure the half-helical pitch (HHP), the number of protomer pairs per
256 HHP, and the mean axial distance (MAD) between the adjacent protomers along
257 the same long-pitch strand[25] and was employed for these analyses (**Figures 3A,**
258 **S1A**). These parameters changed over time (**Figures 3B, S1B, C**), indicating that
259 HHP, the number of actin protomer pairs per HHP, and the MAD values of actin
260 filaments in the unipolar crosslinking configuration in the presence of ATP and S1
261 were not static but rather dynamic. Consequently, these parameters were
262 characterized by broad distributions: HHP (36.3 ± 2.3 nm, N = 1055); number of
263 protomer pairs per HHP (5.5 pairs/HHP [5.4%], 6.5 pairs/HHP [80.3%], 7.5
264 pairs/HHP [13.8%], and 8.5 pairs/HHP [0.5%], N = 6956.5); and MAD (5.5 ± 0.3
265 nm, N = 1055) (**Figure 3C**). In the presence of ATP but not S1, the mean HHP in
266 the filaments crosslinked by alpha-actinin was 36.5 ± 2.8 nm (N = 4270) (**Figure**
267 **S2, Video S3**); these results were similar to those observed in the presence of
268 both S1 and ATP (**Figure 3C**). These results indicated that the HHP of the actin
269 filaments in unipolar crosslinking models underwent intrinsic thermal fluctuations

around a mean value, driven by changes in the number of protomer pairs per HHP and MAD. Under ATP-nearly depleted conditions, S1 persistently associated with the actin filaments in these unipolar crosslinking models (**Figure S1B, Video S2**).

Alpha-actinin inhibits the shortening of major pitch and cofilin binding and the formation of mature cofilin clusters

The HHP and MAD values obtained in this study (**Figures 3, S1, S3, Videos S2-S3**) were compared with those of the control actin filaments (specifically, those without alpha-actinin crosslinking) investigated in our previous studies (e.g., HHP: 36.8 ± 4.3 nm, MAD: 4.3–5.6 nm)[22,25]; here, the physical mechanisms by which crosslinking with alpha-actinin affected the helical twists of the actin filaments upon interaction with S1 or with no S1 interaction were further investigated.

To further explore the physical effects of alpha-actinin on the helical twists of the actin filaments, we initially induced crosslinking between the actin filaments and alpha-actinin in the presence of ATP and $MgCl_2$. Cofilin was then added at a final concentration of 600 nM; this concentration was significantly greater than its binding affinity (k_d) of 5–10 nM for bare actin filaments[68], and the results were compared with those of the actin filaments with cofilin but without the alpha-actin crosslinking (**Figure S3, Table S3, Video S4**). The kinetics of the peak height and HHP fluctuations were analyzed using the same approach as in our previous studies[22,25] (**Figures S3A, B**). In our experiments, the crosslinked filaments were arranged with the same polarity, as determined by the similar crosslinking angles of alpha-actinin[3]. The mean peak height and HHP values of the actin segments crosslinked with alpha-actinin and bound with cofilin (cofilactin-actinin clusters) were 9.9 ± 1.1 nm (N = 2514) and 33.0 ± 4.6 nm (N = 2003), respectively; however, the corresponding values of the mature cofilactin clusters without alpha-actinin crosslinking, which served as the control, were significantly different ($p < 0.05$), with values of 10.7 ± 1.0 nm (N = 425) and 29.7 ± 3.0 nm (N = 300), respectively (**Figure S3C, Table S3**). Two key findings emerged from these experiments: (i) Alpha-actinin significantly inhibited the super twisting of the half helices. Specifically, the major pitches of the half helices of the actin segments crosslinked

300 by alpha-actinin were unable to undergo the shortening induced by the immature
301 cofilactin-actinin clusters; this was reflected by their greater HHP values relative to
302 those of the mature cofilactin clusters without the alpha-actinin crosslinking (HHP:
303 33.0 ± 4.6 nm vs. 29.7 ± 3.0 nm). (ii) Alpha-actinin strongly inhibited the cofilin
304 binding and the formation of the mature cofilin clusters since the peak height of
305 immature clusters of cofilactin-actinin (9.9 ± 1.1 nm) was significantly lower (p <
306 0.05) than that of the mature cofilactin clusters (10.7 ± 1.0 nm) (**Table S3**);
307 however, these values were significantly greater (p < 0.05) than that of the bare
308 actin segments (8.6 ± 0.8 nm), as identified in our previous study[22].

309 **Myosin II and cofilin competitively bind to long and short half helices to**
310 **facilitate cluster formation**

311 The debate on how the actin filaments adopted different conformations to regulate
312 the functions and localizations of various actin-binding proteins (ABPs) within cells
313 is ongoing[17]. To further address this issue, HS-AFM was used to observe the
314 competitive binding of S1 and cofilin to the actin filaments in a buffer containing
315 ADP and ATP. The actin filaments were gently immobilized on a lipid membrane
316 in F-buffer initially containing 1 mM ADP, 0.01 mM ATP, 0.5 mM $MgCl_2$ and 300
317 nM S1, followed by the addition of 100 nM cofilin (**Figure S4, Video S5**). Under
318 high-ADP and low-ATP conditions, S1 transiently associated with the actin
319 filaments and dissociated from the actin filaments, whereas cofilin actively sought
320 binding sites to form clusters. The transient interaction of S1 with the actin
321 filaments consumed ATP, and since ATP became depleted, stable S1 clusters
322 formed; however, these S1 clusters were spatially segregated from the cofilin
323 clusters (**Figure S5, Videos S5, S6**) on the same actin filaments. Analysis of the
324 peak heights and HHPs in the mature S1-actin and cofilactin segment clusters
325 (**Figure S5A**) revealed that the S1 clusters (14.9 ± 1.4 nm (N = 1051) and 33.9 ±
326 4.4 nm (N = 805)) contained higher and longer HHPs than the cofilin clusters (10.5
327 ± 1.0 nm (N = 935) and 25.7 ± 3.6 nm (N = 767)), as assessed by the statistical
328 significance (p < 0.05) (**Figures S5B, C; Table S4**). These findings indicated that
329 S1 and cofilin preferentially bound long and short half helices, respectively, when

330 their stable clusters were formed. Interestingly, these clusters remained
331 segregated on the same actin filaments under ATP-depleted conditions, likely
332 because long HHPs, which supported stable S1 binding; these represented stable
333 half helices similar to those in well-defined or canonical actin filaments, whereas
334 the shorter HHPs, which accommodated the cofilin clusters, corresponded to the
335 constrained and less stable half helices. However, the specific features of the actin
336 filaments that governed the accommodation of S1 and cofilin before and after ATP
337 depletion remained elusive when only HS-AFM, which is a technique that provided
338 the 2D surface structures with nanometer and millisecond resolution, was used.
339 Further exploration of the structural differences among the actin filaments of the
340 different configurations, such as the degree of helical twisting, the number of
341 protomer pairs per HHP, the rise, and the ADs, was crucial for understanding how
342 these properties regulated the binding and functions of different ABPs.

343 **Investigating alpha-actinin dynamics at the atomic level via SimHS-AFMfit**
344 Our HS-AFM–based analyses helped elucidate some of the characteristics of
345 alpha-actinin, including its fluctuations in height and length over time, as well as its
346 actin-crosslinking functions. However, these conventional AFM analyses were
347 unable to reveal the critical insights into the conformational dynamics of the atomic
348 structure and domain interactions of alpha-actin, such as its bending, rotation, and
349 twisting motions. An understanding of these dynamics is essential for
350 understanding the mechanical influence of alpha-actinin on the structure,
351 dynamics, and function of the actin filaments. Thus, we created SimHS-AFMfit
352 through the integration of HS-AFM with AFMfit and MD simulations to further
353 explore the dynamics and atomic structure of alpha-actinin. We employed AFMfit
354 to convert the 2D molecular surfaces of alpha-actinin obtained from HS-AFM into
355 3D atomic conformations (**Figures 4, S6, Videos S7, S8**). Using this approach,
356 we generated libraries of the conformations for the Ca^{2+}-bound and Ca^{2+}-unbound
357 alpha-actinin (**Figure 4A**). These conformations were subsequently aligned to
358 compare the dynamics of the two states according to both the AFMfit analyses and
359 the MD simulations. The distribution of the positions of Cα was broader in the
360 AFMfit analyses than in the MD simulations (**Figure 4A**); this likely occurred
361 because the 100-millisecond-scale HS-AFM measurements captured more
362 extensive molecular movements than the 0.5-microsecond MD simulations.
363 Additionally, substrate interactions that occurred during the AFM analysis, which
364 were not present in the MD simulation results, could influence the dynamics of
365 alpha-actinin.
366 The root mean square fluctuation (RMSF), which is a commonly used metric for
367 evaluating the flexibility and mobility of atoms or residues in proteins, was
368 employed to quantify the deviation of each Cα atom from its average position using
369 the conformational libraries generated with the AFMfit and MD simulations (**Figure**
370 **4B**). The results revealed the dynamic motions of CH1-CH2 within the ABD, neck,
371 and EF12-EF34 domains, whereas the rod (SR1-SR4) domains exhibited relatively
372 high rigidity. Despite the differences estimated in the fluctuation magnitude, both

373 the AFMfit and the MD simulation results consistently demonstrated that compared
374 with the unbound state, the Ca^{2+} binding significantly reduced the motion of the
375 CH1-CH2 and EF12-EF34 domains near the neck.
376 Next, we quantitatively analyzed the dynamic movements of the individual domains
377 at the atomic level by focusing on the distances between CH1 and CH2 within the
378 ABD and between EF12 and EF34 within the CaMD (**Figure S7, Table S5**). On
379 the basis of this analysis, the domain distances were classified as either rigid or
380 flexible. For rigid domains with minimal distance fluctuations, AFMfit confirmed that
381 the ABD had the smallest conformation, and the CH1–CH2 distances for the Ca^{2+}-
382 bound and Ca^{2+}-unbound states were 2.45 ± 0.01 nm and 2.46 ± 0.01 nm,
383 respectively, and these values were consistent with those from previous structural
384 studies[5] (**Figures S7A, B**). Similarly, for the Ca^{2+}-bound and Ca^{2+}-unbound states,
385 the CH1–EF34 distances were 3.06 ± 0.01 nm and 3.07 ± 0.02 nm, respectively,
386 whereas the CH2–EF34 distances were 3.63 ± 0.01 nm and 3.63 ± 0.02 nm,
387 respectively. For flexible domains with larger distance fluctuations, AFMfit
388 demonstrated that Ca^{2+} binding significantly reduced the magnitude of fluctuations
389 relative to the unbound state. Specifically, the CH1-EF12 distances were 3.89 ±
390 0.16 nm and 3.76 ± 0.21 nm for the Ca^{2+}-bound and Ca^{2+}-unbound states,
391 respectively. Similarly, the CH2–EF12 distances were 4.58 ± 0.06 nm and 4.53 ±
392 0.09 nm, whereas the EF12–EF34 distances were 2.81 ± 0.05 nm and 2.73 ± 0.07
393 nm, respectively.
394 The results from the MD simulations corroborated the molecular dynamics of Ca^{2+}-
395 bound and Ca^{2+}-unbound alpha-actin obtained with AFMfit, revealing similar trends
396 at the atomic level (**Figures S7A, C, D; Table S5**). While the AFMfit had greater
397 magnitudes of the domain fluctuations than MD simulations, both methods
398 consistently demonstrated that the Ca^{2+} binding to the EF12 domain reduced the
399 degree of fluctuations in the alpha-actinin dynamics. Our SimHS-AFMfit
400 simultaneously captured and described the atomic conformations and dynamics of
401 alpha-actinin, partially bridging temporal and spatial gaps between the
402 experimental AFM data and MD simulations. This approach surpassed the

403 limitations of previous static structural studies based on X-ray scattering[5,7–9] and
404 cryo-EM[6].

405 **Classifying the dynamic conformations of alpha-actinin via PCA**

406 PCA is a statistical method used to reduce the dimensionality of a dataset while
407 retaining its most significant variations. It is highly effective in identifying and
408 classifying the collective motions of individual protein domains using principal
409 components (PCs).

410 First, we determined the ensemble of the atomic motions of the Ca^{2+}-bound and
411 Ca^{2+}-unbound alpha-actinin by analyzing the libraries of the conformations
412 obtained from both the AFMfit and MD simulations and projected these motions
413 onto a common PCA space (**Figure 5A, Videos S9-S11**). The eigenvalues of
414 principal component 1 (PC1), PC2, and PC3 were used to determine the
415 percentage contribution of each motion. PC1 (36%) primarily captured the
416 ensemble of the opposite-direction bending motions or neck rotation, PC2 (20%)
417 represented same-direction bending motions or neck bending, and PC3 (15%)
418 described a combination of opposite-direction bending and twisting motions.

419 To compare the data obtained from the AFMfit and MD simulations, we projected
420 the conformational libraries of the Ca^{2+}-bound and Ca^{2+}-unbound alpha-actinin
421 generated from both the AFMfit analyses and MD simulations onto a common PCA
422 space and plotted the distributions of PC1 versus PC2 and PC1 versus PC3
423 (**Figure 5B**). For the Ca^{2+}-bound state, PC1 from the AFMfit conformational
424 libraries captured a broad and symmetric distribution of opposite-direction
425 bending, whereas that from the MD simulation libraries demonstrated a narrower
426 and more asymmetric distribution. In contrast, for the Ca^{2+}-unbound state, PC1
427 from the AFMfit libraries exhibited an asymmetric distribution, whereas that of the
428 MD simulation libraries demonstrated a more symmetric pattern; these results
429 highlighted the different spectral characteristics between the two methods.

430 Despite the differences in the fluctuation magnitude exhibited between the AFMfit
431 analyses and MD simulations (**Figure 4**), the PC2 value derived from both the
432 AFMfit analyses and MD simulations consistently captured the motions of both the

433 Ca^{2+}-bound and the Ca^{2+}-unbound states; these results indicated the overlapping
434 spectra between the two methods. A similar trend was observed for PC3, which
435 captured comparable fluctuation spectra in the Ca^{2+}-bound state for both methods.
436 However, for the Ca^{2+}-unbound state, PC3 exhibited distinct fluctuation spectra
437 between the two approaches. Therefore, PCA successfully analyzed and
438 categorized the physical motions in the Ca^{2+}-bound and Ca^{2+}-unbound alpha-
439 actinin using PC1, PC2, and PC3; these PCs were derived from the conformations
440 generated via AFMfit analysis and the MD simulations (**Figures 4, 5**). Across all
441 results, the eigenvectors represented by the white arrows in SR1 and SR4 were
442 small, whereas those in SR2 and SR3 showed almost no motion; these results
443 confirmed the rigidity of the rod domain. In contrast, prominent eigenvectors were
444 observed in CH1–CH2 within the ABD, in EF12–EF34, and in the neck domain,
445 indicating relatively high flexibility in these regions (**Figures 4A, 5A**). In summary,
446 our SimHS-AFMfit demonstrates an outstanding ability to capture and categorize
447 the atomic conformational dynamics of the Ca^{2+}-bound and Ca^{2+}-unbound alpha-
448 actinin.
449 To better capture the collective motions of the molecules, we also analyzed the
450 bending and twisting angles of the ABD relative to the rod domain in both the Ca^{2+}-
451 bound and Ca^{2+}-unbound alpha-actinin. As described above, PCA of the
452 conformations confirmed the rigidity of the rod domain (SR2-SR3). With reference
453 to a vector defined along the Cα positions within the SR2-SR3 domain (**Figure**
454 **S8**), the bending angles were measured relative to the center of mass of the Cα
455 atoms in the CH1, CH2, EF12, and EF34 domains near the neck in chain 1 (red)
456 and chain 2 (blue) (**Figure S8A**). To measure the twisting angles, the vectors were
457 defined by linking the centers of mass of the Cα atoms between the EF12-EF34
458 and CH1-CH2 domains, and the angles of these vectors were measured relative
459 to the SR2-SR3-aligned reference vector (**Figure S8B**). The distributions of
460 bending and twisting angles in chain 1 and chain 2, with and without Ca^{2+} binding,
461 were analyzed to more effectively capture the directions of the collective motions,
462 whether in the same or opposite direction. Quantitative measurements of the

463 bending and twisting angles in chains 1 and 2 of the Ca^{2+}-bound and Ca^{2+}-unbound
464 alpha-actinin based on the AFMfit and MD simulations (**Figure S8, Table S6**)
465 confirmed the flexibility of the bending and twisting motions of alpha-actinin.
466 Despite the previously identified differences between the two methods in their
467 ability to estimate the magnitudes of fluctuation, both the AFMfit and the MD
468 simulations showed that Ca^{2+} binding could restrict these motions to some extent.
469 Our approach effectively refined and categorized the impact of Ca^{2+} on physical
470 motions, such as the bending and twisting of smooth muscle alpha-actinin. When
471 the ensemble of conformations obtained using our method was compared with
472 those obtained from other techniques, such as cryo-EM[6], which reported that
473 isoform 2 alpha-actinin was not sensitive to Ca^{2+}, our findings were not only
474 consistent but also provided a better description of its dynamic nature.

475 **Comparing the key principal components derived from the AFMfit and MD**
476 **simulations**

477 To explore the collective motions of alpha-actinin using a multidimensional
478 approach such as SimHS-AFMfit, we separately projected the conformational
479 libraries of the Ca^{2+}-bound and Ca^{2+}-unbound alpha-actinin generated from the
480 AFMfit analyses and MD simulations onto PCA spaces. We then plotted and
481 compared the key PCs (PC1, PC2, and PC3) that described the collective motions
482 of the domains of alpha-actinin via the same eigenvectors (**Figures S9, S10,**
483 **Videos S12-S15**).

484 For the conformation libraries derived with AFMfit (**Figure S9A, Videos S12, S13**),
485 PC1, PC2, and PC3 characterized the physical motions of Ca^{2+}-bound alpha-
486 actinin as opposite-direction bending (neck rotation), twisting, and opposite-
487 direction bending (neck rotation), respectively. In contrast, for Ca^{2+}-unbound
488 alpha-actinin, PC1, PC2, and PC3 corresponded to opposite-direction bending
489 (neck rotation), same-direction bending (neck bending), and opposite-direction
490 bending (neck rotation), respectively.

491 Similarly, for the MD simulation-based libraries (**Figure S9B, Videos S14-S15**),
492 PC1, PC2, and PC3 characterized same-direction bending (neck bending),

493 opposite-direction bending (neck rotation), and a combination of twisting and
494 rotation, respectively, in the Ca^{2+}-bound alpha-actinin. In the unbound state, these
495 PCs corresponded to same-direction bending (neck bending), opposite-direction
496 bending (neck rotation), and twisting, respectively.
497 Based on the eigenvectors derived from the conformation libraries obtained with
498 AFMfit for both the bound and unbound states (**Figures S10A, B**), PC1 and PC3
499 consistently captured the opposite-direction bending motions or neck rotations,
500 despite the differences in the fluctuation magnitudes between the AFMfit and MD
501 simulations; these results indicated a high degree of spectral overlap in the
502 conformations derived with the two methods. However, PC2 exhibited distinct
503 behaviors between the states and captured the twisting motions in the Ca^{2+}-bound
504 state and same-direction bending motions or neck rotations in the Ca^{2+}-unbound
505 state, highlighting a significant spectral difference between the two methods.
506 Similarly, based on eigenvectors derived from the conformation libraries obtained
507 from the MD simulations for both the bound and unbound states (**Figures S10C,**
508 **D**), PC1 and PC2 consistently captured the same-direction and opposite-direction
509 bending motions in the Ca^{2+}-bound and unbound states, respectively, despite the
510 differences in the fluctuation magnitudes between the AFMfit and MD simulations;
511 these results further indicated strong spectral overlap. In contrast, PC3 showed
512 distinct behaviors for the two states and captured a combination of twisting and
513 bending motions in the Ca^{2+}-bound state and primarily twisting motions in the Ca^{2+}-
514 unbound state; these results indicated that the two methods revealed significant
515 spectral differences. In summary, SimHS-AFMfit could effectively capture and
516 classify the physical motions of alpha-actinin within various common PCA spaces.
517 The interpretation was further validated by separately analyzing the correlations
518 among PC1, PC2, and PC3 and the bending and twisting angles in chains 1 and
519 2 (**Figures S11, S12, Videos S12-S15**). In both the Ca^{2+}-bound and Ca^{2+}-unbound
520 states derived from AFMfit, PC1 and PC3 demonstrated strong positive and
521 negative linear correlations with the bending angles of the two chains (**Figure**
522 **S11**); these results confirmed opposite-direction bending between them (**Figure**

523 **S9A, Videos S12-S13**). Conversely, PC2 exhibited a strong linear correlation with
524 the twisting angle in the Ca^{2+}-bound state and confirmed the role of this PC in
525 capturing the twisting motion. However, in the Ca^{2+}-unbound state, the correlations
526 between PC2 and the bending angles for chains 1 and 2 were very similar; these
527 results indicated that this PC captured the same-direction bending motions for this
528 conformation (**Figures S9A, S11, Video S12-S13**).
529 In both the Ca^{2+}-bound and Ca^{2+}-unbound states derived from the MD simulations,
530 PC1 exhibited strong negative linear correlations with the bending angles of both
531 chains (**Figure S12**) and indicated the same-direction bending in the two
532 conformations (**Figure S9B, Videos S14-S15**). In contrast, PC2 demonstrated
533 strong negative and positive linear correlations with the bending angles in the two
534 chains; these results indicated opposite-direction bending in the Ca^{2+}-bound and
535 Ca^{2+}-unbound states, whereas PC3 was weakly correlated with the two bending
536 angles and was largely sensitive to the twisting angle; thus, this PC captured a
537 combination of twisting and bending motions in the Ca^{2+}-bound state and primarily
538 twisting motion in the Ca^{2+}-unbound state (**Figures S9B, S12, Videos S14-S15**).
539 Overall, the AFMfit and MD simulations consistently identified the key motions in
540 both the Ca^{2+}-bound and Ca^{2+}-unbound alpha-actinin, although some
541 discrepancies remained due to factors such as differences in the temporal and
542 spatial resolutions or sample fixation between the HS-AFM and MD simulations.
543 AFMfit was shown to be a powerful tool for transforming the 2D surface images
544 obtained from AFM into 3D atomic conformations; however, its integration with
545 complimentary techniques such as MD simulations is crucial for addressing the
546 spatial and temporal gaps in the AFM data.

547 **Analyzing complex protein models using SimHS-AFMfit**

548 In this study, we developed a novel strategy that integrated HS-AFM, AFMfit, and
549 MD simulations (SimHS-AFMfit) to address some limitations in the spatial and
550 temporal resolution of AFM using Ca^{2+}-bound and Ca^{2+}-unbound alpha-actinin.
551 This approach successfully captured the physical motions of individual domains
552 and distinguished the atomic conformational changes in alpha-actinin following
553 binding with Ca^{2+}.

554 However, converting complex 2D AFM images of actin filaments crosslinked to
555 alpha-actinin (**Figures 3, S1, S2, Videos S2, S3**) into 3D atomic conformations
556 with AFMfit remained challenging because of the intricate nature of these protein
557 assemblies, which include both actin filaments and alpha-actinin. By also
558 employing MD simulations, we constructed two models of unipolar and bipolar
559 crosslinking, along with a model of a bare actin filament, and these models were
560 simulated under the same conditions used for alpha-actinin for 100 ns (**Figures 6,**
561 **S13, Videos S16-S20**).

562 We next analyzed the atomic conformational dynamics of Ca^{2+}-unbound alpha-
563 actinin in the unipolar and bipolar models (**Figure S13, Videos S16-S17**). In the
564 unipolar configuration, PC1, PC2, and PC3 primarily captured same-direction
565 (neck bending), opposite-direction (neck rotation), and same-direction (neck
566 bending) motions, respectively, as indicated by the trajectories marked by the
567 white arrows (**Figure S13A, Video S16**). Conversely, in the bipolar model, PC1,
568 PC2, and PC3 corresponded to opposite-direction (neck rotation), same-direction
569 (neck bending), and an unclassified mode predominantly observed in lower ABD
570 movements, respectively (**Figure S13B, Video S17**).

571 Since each actin filament in all the MD simulation models contained 13 fixed
572 protomers (equal to 6.5 promoter pairs/HHP), the fluctuations in the HHP across
573 all conformations were minimal, with values of ~36.2 ± 0.0 nm for bare actin, 36.3
574 ± 0.0 nm for both bipolar-flexible and bipolar-fixed models, and 36.3 ± 0.0 nm for
575 the unipolar-flexible model (**Figure 6A, C; Table S7**). These values aligned with
576 our expectations from previous findings and indicated that the fluctuations in the

577 HHP primarily resulted from the variations in the number of protomers per
578 HHP[25,26,69]. However, the rise values exhibited large fluctuations of varying
579 magnitudes: 2.8 ± 0.1 nm for bare actin, 2.8 ± 0.2 nm and 2.9 ± 0.2 nm for the
580 bipolar-flexible and bipolar-fixed models, respectively, and 2.8 ± 0.1 nm for the
581 unipolar-flexible model. A similar trend was observed in the AD values, with values
582 of 5.6 ± 0.1 nm for bare actin, 5.7 ± 0.2 nm for both bipolar-flexible and bipolar-
583 fixed models, and especially 6.0 ± 0.3 nm for the unipolar-flexible model (**Figure**
584 **6C, Table S7**). Statistical analysis revealed that when comparing the bare actin
585 filaments to those in the unipolar and bipolar models, the AD values were
586 significantly different ($p < 0.05$, *t-test*), whereas the rise values were not
587 significantly different (**Figure 6C, Table S7**). Additionally, the rise values between
588 the bipolar-fixed model and that in bipolar-flexible and unipolar-flexible models
589 were also significantly different ($p < 0.05$, *t-test*), whereas the rise and AD values
590 were not significantly different when comparing them between bipolar-flexible and
591 unipolar-flexible models.
592 The local residue contact maps between the two ABDs in the alpha-actinin
593 molecule and the actin protomers greatly differed between the unipolar-flexible and
594 bipolar-flexible and bipolar-fixed crosslinking models (**Figure 6D, E; Table S10**).
595 These differences provide a biochemical basis for validating key component
596 interactions that regulate conformational changes in actin filaments across
597 different cellular assemblies.
598 These findings indicated that the fluctuations in rise and AD were intrinsic
599 properties of actin filaments and that binding with alpha-actinin further amplified
600 the AD fluctuations compared with those of bare filaments. The binding of alpha-
601 actinin to actin filaments differed between the unipolar and bipolar models in
602 several aspects, including the residue-level interactions between the alpha-
603 actinin's ABDs and actin filaments, the spacing between the two filaments, and the
604 crosslinking angles of alpha-actinin relative to the filaments (**Figures 6, S14,**
605 **Tables S8-S10**). Consequently, alpha-actinin could exert distinct physical effects,
606 such as neck bending or neck rotation (**Figure S13**), on the actin protomers and

607 cause differential conformational changes, as reflected in the significantly
608 increased AD fluctuations. This prediction was validated by the MD simulations of
609 bipolar-fixed model, which revealed restricted motion of alpha-actinin (**Figure 6,**
610 **Video S20**). This restriction is unlikely to influence the increased fluctuations in
611 rise and AD of filaments, suggesting that alpha-actinin's ABD binding alone (**Table**
612 **S10**) is sufficient to drive these changes.

613 **Discussion**

614 **Alpha-actinin regulates the dynamic conformations and functions of the**
615 **actin filaments by interacting with myosin II while inhibiting cofilin binding**
616 **and cluster formation**

617 In this study, we successfully developed a novel workflow, SimHS-AFM, to convert
618 the 2D AFM images of alpha-actinin into the 3D atomic conformations. This
619 workflow enables the classification of the physical motions of these proteins
620 through PCA (**Figures 4, 5, Videos S7-S15**), including their domain distances and
621 twisting and bending modes (**Figures S7-S12, Videos S12-S15**). We further
622 explored the roles of Ca^{2+} in regulating the conformational changes of smooth
623 muscle alpha-actinin and simulate its actin-crosslinking effects on the dynamics
624 and atomic structure of the actin filaments (**Figures 6, S13, Videos S16-S17**).
625 Additionally, we identify the variations in rise and AD, distinguishing the bare actin
626 filaments (2.8 ± 0.1 nm, 5.6 ± 0.1 nm) from their unipolar (2.8 ± 0.1 nm; 6.0 ± 0.3
627 nm) and bipolar (2.8 ± 0.2 nm, 5.7 ± 0.2 nm) flexible models (**Figure 6C, Table S7,**
628 **Videos S18-S19**). These structural characteristics, including the rise and AD
629 fluctuations as well as distinct residue-level interactions, play critical roles in
630 regulating the excitatory binding of myosin II (S1) and the inhibitory binding of
631 cofilin. These findings increase our understanding of the physical properties and
632 biological functions of alpha-actinin and actin filaments.

633 Additionally, we experimentally investigated the actin-crosslinking with alpha-
634 actinin in unipolar configurations using HS-AFM (**Figures 3, S1-S2, S14, Videos**
635 **S2-S3**). This led to the hypothesis that alpha-actinin crosslinking increased the rise
636 and AD or MAD fluctuations, which aligned with the MD simulation results, and
637 influenced the binding of S1 and cofilin (**Figures 7A, S3, Video S4**).
638 i) Bare actin filaments typically support the normal binding and functional activity
639 of cofilin and S1 (**Figures S4, S5, Videos S5-S6**). The binding and clustering of
640 cofilin tend to shorten the HHP by approximately 25%, reducing the number of the
641 protomer pairs per HHP (usually to 4.5 or 5.5 protomer pairs per HHP)[25,70–72]. In
642 contrast, S1 binding maintains a longer HHP (**Figure 7A**).
643 (ii) When alpha-actinin crosslinks with the actin filaments in the unipolar model,
644 cofilin binding and the formation of the mature cofilin clusters are substantially
645 inhibited, thus preventing the shortening of the HHP (**Figure S3, Video S4**).
646 Moreover, alpha-actinin crosslinking preserves a long HHP without affecting the
647 binding activity of S1 (**Figures 3, 7A, S1, S2, Videos S2-S3**).
648 Our findings indicate that the fluctuations in rise and AD are inherent in the bare
649 actin filaments and that crosslinking with alpha-actinin further strengthens the AD
650 vibrations in both the bipolar and unipolar models. Interestingly, even when all Cα
651 atoms in alpha-actinin were computationally constrained while the other atoms
652 remained flexible, the MD simulations of a bipolar model over 100 ns (**Figure 6C**)
653 reveal that ABD binding to actin filaments alone is sufficient to drive these
654 structural changes. Residue-level contacts play a crucial role in determining the
655 extent of the AD fluctuations (**Figure 6D-E, Table S10, Videos S19-S20**). These
656 results are further supported by our MD simulations, which demonstrate that
657 allowing backbone inflexibility in the Cα atoms of alpha-actinin in the bipolar-fixed
658 crosslinking model result in AD values comparable to those observed in the fully
659 flexible alpha-actinin model, where rotational motions of the ABD around the neck
660 or just strong alpha-actinin's ABD-actin interaction enhance the AD fluctuations in
661 the actin filaments.

662 Notably, previous experimental data have demonstrated that fluctuations in the
663 rise are more pronounced in the bent actin filaments bound to ADP than in those
664 bound to ADP+Pi[73]. Additionally, the mean axial distance (MAD) between two
665 adjacent actin protomers along the same long-pitch strand is greater within the
666 shortened bare half helices (5.0–6.3 nm) than within the typically sized helices
667 (4.3–5.6 nm)[25]. The differences in the fluctuation magnitudes of the AD or MAD
668 induced by the different ABPs, such as alpha-actinin and cofilin, may provide key
669 insights into how these compounds regulate each other's binding or inhibitory
670 effects on the actin filaments.
671 Interestingly, the actin filaments crosslinked with alpha-actinin play distinct roles
672 depending on their crosslinking configuration and location in a cell (**Figure 7B**). In
673 the bipolar model, they are involved primarily in structures such as contractile rings
674 (CRs), stress fibers, and sarcomeres, whereas in the unipolar configuration, they
675 contribute to lamellipodia, filopodia, cortical actin, and microvilli (**Table S2**). Our
676 results indicate that future research should focus on experimentally investigating
677 the atomic conformational dynamics of the actin filaments in unipolar and bipolar
678 crosslinking models, including rise, AD fluctuations, and key residue-interactions
679 (**Table S10**), to gain deeper insights into the functional and spatial differences
680 between these assemblies within the cells.

681 **Advantages of SimHS-AFMfit**

682 Time-resolved cryo-EM is emerging as a powerful tool for investigating protein
683 dynamics and atomic conformations simultaneously[74–76]. Its potential can be
684 further enhanced by integrating approaches such as cryo-EM flexible fitting[77] and
685 computational methods. Additionally, advanced NMR spectroscopy provides
686 complementary insights and captures both structural and dynamic aspects of
687 proteins during interactions[42,43,78,79].
688 While NMR spectroscopy excels in studying protein structure, dynamics, and
689 interactions, it has limitations. Traditional solution-state NMR is most effective for
690 proteins under ~30–50 kDa, although techniques such as transverse relaxation-
691 optimized spectroscopy (TROSY) extend this range to ~100 kDa. Larger proteins

692 suffer from the signal overlap and line broadening because of the slow molecular
693 tumbling and transverse relaxation. Compared with cryo-EM and X-ray
694 crystallography, NMR also has lower sensitivity, and peak overlap complicates
695 resonance assignments in complex systems[43,80–82].
696 In dynamic studies, NMR provides insights into timescales from picoseconds to
697 seconds but struggles with motions faster than 10 ps or slower than seconds to
698 minutes[81,82]. Solid-state NMR remains challenging for membrane proteins
699 because of the need for extensive isotopic labeling and specialized pulse
700 sequences[82]. Additionally, weak or transient interactions can produce signals that
701 are too faint for accurate characterization. Sample preparation and long data
702 acquisition times (hours to days) further risk protein degradation or aggregation[80].
703 While cryo-EM surpasses NMR in resolving large protein complexes (>100 kDa),
704 it is less effective for studying dynamics[83]. However, these techniques can
705 complement each other[84]. Other single-molecule techniques, such as FRET, can
706 complement NMR for fast dynamics[85], but no standalone method can perfectly
707 capture the atomic structures, dynamics, and interactions simultaneously.
708 Despite the inherent limitations of AFM, such as its ability to capture only 2D
709 surface images with a maximum spatial resolution of 1 nm in the x–y plane and 0.1
710 nm in the z dimension, recent advancements in HS-AFM have significantly
711 increased its temporal resolution. Due to these improvements, imaging at
712 timescales of a few tens of milliseconds or faster can be performed and enable a
713 more precise characterization of protein dynamics[53]. HS-AFM has the ability to
714 image large complex protein systems without the need for chemical labeling,
715 enabling the simultaneous capture of nanostructures, dynamics, and protein
716 interactions or assemblies under near-physiological conditions; this capability
717 surpasses those of NMR and cryo-EM. Additionally, by integrating HS-AFM with
718 the AFMfit[57] and MD simulations[47,48] through SimHS-AFMfit, we generated
719 comprehensive libraries of atomic conformations, facilitating the investigation of
720 the physical motions, atomic structures, and functions of alpha-actinin through
721 PCA and providing a robust framework for improving the interpretation of low-

722 resolution experimental AFM and simulated data. For example, the twisting and
723 bending motions of alpha-actinin were cross-validated through the AFMfit and MD
724 simulations, providing deeper insights into the mechanical effects on the actin
725 filaments. Compared with those of bare actin filaments, the SimHS-AFMfit reveals
726 increased AD dynamic fluctuations in the bare actin filament and bipolar
727 crosslinking models; this capability surpasses previous static structural studies
728 using X-ray diffraction[15,16] and cryo-EM[13,86]. This characteristic of actin filaments,
729 which was originally explored in our previous studies[25] and further demonstrated
730 in various crosslinking models here, may play a crucial role in regulating the
731 binding and function of myosin II, cofilin and other ABPs. Ultimately, this integration
732 addresses the spatial and temporal limitations of experimental AFM data and
733 facilitates the study of the atomic conformational dynamics of more complex
734 protein assemblies.
735 Apparently, SimHS-AFMfit still faces challenges in bridging the temporal gaps
736 between millisecond AFM imaging and microsecond MD simulations, highlighting
737 the need for future improvements to address these discrepancies. Additionally, the
738 ability of AFMfit to fit large complex protein assemblies is still challenging because
739 of the complicated models used, necessitating the development of improved fitting
740 algorithms or models. However, the data obtained through SimHS-AFMfit can be
741 useful for developing force fields to simulate complex protein models, as
742 demonstrated in previous studies[49–52]. Force fields are crucial for accurately
743 validating the interatomic forces acting between the atoms composing the system
744 since they account for the intermolecular or interatomic interactions and energy
745 minimization[87,88]. Specifically, our workflow facilitates the use of AFMfit to analyze
746 the experimental AFM data of complex actin filaments crosslinked with alpha-
747 actinin. More broadly, the conformational libraries could also serve as training data
748 for the deep learning models[89–91] to predict the pseudoatomic structures across
749 different timescales (i.e., prediction of protein dynamics) and help bridge the gap
750 between the experimental and computational methods. In this context, recent
751 advancements in three-dimensional localization AFM (3D-LAFM) have

752 successfully transformed the AFM data into 3D density data[92], facilitating large-
753 scale 3D atomic AFM data generation through the integration with the MD
754 simulations.
755 In conclusion, SimHS-AFMfit provides an innovative approach for overcoming the
756 spatial resolution limitations of AFM data. This method can be further developed,
757 such as by its integration with AI, NMR, cryo-EM, cryo-ET, or in silico AFM[93], to
758 bridge the spatiotemporal resolution gaps between HS-AFM and the MD
759 simulations and to predict protein dynamics; this has enabled real-time studies of
760 the atomic conformational dynamics of complex proteins and surpassing the
761 capabilities of individual techniques. Our approach facilitates new possibilities for
762 advancing the understanding of the atomic structural dynamics of complex protein
763 assemblies that mimic cellular machines.

Methods

Materials and methods are included in the Supplementary Information.

Data availability

All the data are included in the Supplementary Information or as source data. The conformation libraries, available in PDB format, can be accessed upon reasonable request and are open for AI-based training collaboration.

Code availability

https://gricad-gitlab.univ-grenoble-alpes.fr/GruLab/afmfit

Acknowledgments

The authors express their gratitude for the facility and financial support provided by the WPI Nano Life Science Institute (WPI NanoLSI), Kanazawa University; the instrumental assistance provided by Toshio Ando, Noriyuki Kodera, and Hiroki Konno (WPI NanoLSI); and the initial bipolar and unipolar models presented by Kenneth A. Taylor (Florida State University); and initial AFM data analysis by Thao Phuong Ngo and Thien Quang Huynh (WPI-NanoLSI). The authors also acknowledge the financial support from KAKENHI (Japan Society for the Promotion of Science) for K.X.N. (19K06581, 23K05713, 23H02452-01), T.S. (24K01308), and T.Q.P.U. (23H02452). The MD simulations were carried out on the supercomputers at the Research Center for Computational Science in Okazaki, Japan (Project: 24-IMS-096).

This study was also partially supported by the French National Research Agency (research grant ANR-23-CE45-0024-01) and within the framework of the "Investissements d'avenir" program (ANR-15-IDEX-02) for S.G.

Author Contributions:

K.X.N. designed the research; K.X.N., T.S., R.V. and S.G. performed the research; K.X.N., T.S., R.V., H.G.N., T.Q.P.U., N.T.P.L., and S.G. analyzed the data; K.X.N., T.S., R.V. and S.G. wrote the paper.

Declaration of interests:

The authors declare that they have no competing interests.

Declaration of generative AI and AI-assisted technology

During the preparation of this work, the authors used ChatGPT to enhance the clarity of the English in their writing. After utilizing this tool, they carefully reviewed and edited the content as necessary and take full responsibility for the final publication. Furthermore, the manuscript has been submitted for scientific and English editing through Nature Springer's service.

References

1. Fukami, K., Furuhashi, K., Inagaki, M., Endo, T., Hatano, S., and Takenawa, T. (1992). Requirement of phosphatidylinositol 4,5-bisphosphate for α-actinin function. Nature *359*, 150–152. https://doi.org/10.1038/359150a0.

2. Fraley, T.S., Tran, T.C., Corgan, A.M., Nash, C.A., Hao, J., Critchley, D.R., and Greenwood, J.A. (2003). Phosphoinositide binding inhibits α-actinin bundling activity. J. Biol. Chem. *278*, 24039–24045. https://doi.org/10.1074/jbc.M213288200.

3. Taylor, K. a, and Taylor, D.W. (1994). Formation of two-dimensional complexes of F-actin and crosslinking proteins on lipid monolayers: demonstration of unipolar alpha-actinin-F-actin crosslinking. Biophys. J. *67*, 1976–1983. https://doi.org/10.1016/S0006-3495(94)80680-0.

4. Young, P. (2000). The interaction of titin and alpha-actinin is controlled by a phospholipid-regulated intramolecular pseudoligand mechanism. EMBO J. *19*, 6331–6340. https://doi.org/10.1093/emboj/19.23.6331.

815 5. Ribeiro, E.D.A., Pinotsis, N., Ghisleni, A., Salmazo, A., Konarev, P. V.,
816 Kostan, J., Sjöblom, B., Schreiner, C., Polyansky, A.A., Gkougkoulia, E.A.,
817 et al. (2014). The structure and regulation of human muscle α-Actinin. Cell
818 *159*, 1447–1460. https://doi.org/10.1016/j.cell.2014.10.056.

819 6. Liu, J., Taylor, D.W., and Taylor, K.A. (2004). A 3-D reconstruction of smooth
820 muscle α-actinin by CryoEm reveals two different conformations at the actin-
821 binding region. J. Mol. Biol. *338*, 115–125.
822 https://doi.org/10.1016/j.jmb.2004.02.034.

823 7. Foley, K.S., and Young, P.W. (2014). The non-muscle functions of actinins:
824 An update. Biochem. J. *459*, 1–13. https://doi.org/10.1042/BJ20131511.

825 8. Pinotsis, N., Zielinska, K., Babuta, M., Arolas, J.L., Kostan, J., Khan, M.B.,
826 Schreiner, C., Salmazo, A., Ciccarelli, L., Puchinger, M., et al. (2020).
827 Calcium modulates the domain flexibility and function of an α-actinin similar
828 to the ancestral a-actinin. Proc. Natl. Acad. Sci. U. S. A. *117*, 22101–22112.
829 https://doi.org/10.1073/pnas.1917269117.

830 9. Tang, J., Taylor, D.W., and Taylor, K. a (2001). The three-dimensional
831 structure of alpha-actinin obtained by cryoelectron microscopy suggests a
832 model for Ca(2+)-dependent actin binding. J. Mol. Biol. *310*, 845–858.
833 https://doi.org/10.1006/jmbi.2001.4789.

834 10. Pollard, T.D., and Cooper, J.A. (2009). Actin, a central player in cell shape
835 and movement. Science *326*, 1208–1212.
836 https://doi.org/10.1126/science.1175862.

837 11. Fernandez, M.K., Sinha, M., Zidan, M., and Renz, M. (2024). Nuclear actin
838 filaments–a historical perspective. Nucleus *15*.
839 https://doi.org/10.1080/19491034.2024.2320656.

840 12. Egelman, E.H. (1994). Actin Filament Structure: The ghost of ribbons past.
841 Curr. Biol. *4*, 79–81. https://doi.org/10.1016/S0960-9822(00)00020-8.

842 13. Fujii, T., Iwane, A.H., Yanagida, T., and Namba, K. (2010). Direct
843 visualization of secondary structures of F-actin by electron cryomicroscopy.
844 Nature *467*, 724–728. https://doi.org/10.1038/nature09372.

845 14. Holmes, K.C., Popp, D., Gebhard, W., and Kabsch, W. (1990). Atomic model
846 of the actin filament. Nature *347*, 44–49. https://doi.org/10.1038/347044a0.

847 15. Lorenz, M., Popp, D., and Holmes, K.C. (1993). Refinement of the F-actin
848 model against x-ray fiber diffraction data by the use of a directed mutation
849 algorithm. J. Mol. Biol. *234*, 826–836.

850 16. Oda, T., Iwasa, M., Aihara, T., Maéda, Y., and Narita, A. (2009). The nature
851 of the globular- to fibrous-actin transition. Nature *457*, 441–445.
852 https://doi.org/10.1038/nature07685.

853 17. Uyeda, T.Q.P., Yamazaki, Y., Kijima, S.T., Noguchi, T.Q.P., and Ngo, K.X.
854 (2025). Multiple Mechanisms to Regulate Actin Functions : " Fundamental "
855 Versus Lineage-Specific Mechanisms and Hierarchical Relationships.
856 Biomolecules *15*, 1–37. https://doi.org/10.3390/biom15020279.

857 18. Tsuda, Y., Yasutake, H., Ishuima, A., and Yanaogida, T. (1996). Torsional
858 rigidity of single actin filaments and actin-actin bond breaking force under
859 torsion measured directly by in vitro micromanipulation. Proc. Natl. Acad.
860 Sci. U. S. A. *93*, 12937–12942. https://doi.org/10.1073/pnas.93.23.12937.

861 19. ben-Avraham, D., and Tirion, M.M. (1995). Dynamic and elastic properties
862 of F-actin: a normal-modes analysis. Biophys. J. *68*, 1231–1245.
863 https://doi.org/10.1016/S0006-3495(95)80299-7.

864 20. Okura, K., Matsumoto, T., Narita, A., and Tatsumi, H. (2023). Mechanical
865 Stress Decreases the Amplitude of Twisting and Bending Fluctuations of
866 Actin Filaments. J. Mol. Biol. *435*, 168295.
867 https://doi.org/10.1016/j.jmb.2023.168295.

868 21. Sun, Z.G., and Murrell, M. (2024). Cofilin-Mediated Filament Softening and
869 Crosslinking Counterbalance to Enhance Actin Network Flexibility. Phys.
870 Rev. Lett. *133*, 218402. https://doi.org/10.1103/PhysRevLett.133.218402.

871 22. Ngo, K.X., Kodera, N., Katayama, E., Ando, T., and Uyeda, T.Q. (2015).
872 Cofilin-induced unidirectional cooperative conformational changes in actin
873 filaments revealed by high-speed atomic force microscopy. Elife *4*, 1–22.
874 https://doi.org/10.7554/eLife.04806.

875 23. Hosokawa, N., Kuragano, M., Yoshino, A., Shibata, K., Uyeda, T.Q.P., and
876 Tokuraku, K. (2021). Unidirectional cooperative binding of fimbrin actin-
877 binding domain 2 to actin filament. Biochem. Biophys. Res. Commun. *552*,
878 59–65. https://doi.org/10.1016/j.bbrc.2021.02.139.

879 24. Ngo, K.X., Umeki, N., Kijima, S.T., Kodera, N., Ueno, H., Furutani-Umezu,
880 N., Nakajima, J., Noguchi, T.Q.P., Nagasaki, A., Tokuraku, K., et al. (2016).
881 Allosteric regulation by cooperative conformational changes of actin
882 filaments drives mutually exclusive binding with cofilin and myosin. Sci. Rep.
883 *6*, 1–11. https://doi.org/10.1038/srep35449.

884 25. Ngo, K.X., Vu, H.T., Umeda, K., Trinh, M.-N., Kodera, N., and Uyeda, T.
885 (2024). Deciphering the actin structure dependent preferential cooperative
886 binding of cofilin. Elife *13*, 1–37. https://doi.org/10.7554/eLife.95257.

887 26. Fineberg, A., Takagi, Y., Thirumurugan, K., Andrecka, J., Billington, N.,
888 Young, G., Cole, D., and Burgess, S.A. (2024). Myosin-5 varies its step
889 length to carry cargo straight along the irregular F-actin track. Proc. Natl.
890 Acad. Sci. *121*, 1–12. https://doi.org/10.1073/pnas.2401625121.

891 27. Ngo, K.X., Umeki, N., Kijima, S.T., Kodera, N., Ueno, H., Furutani-Umezu,
892 N., Nakajima, J., Noguchi, T.Q.P., Nagasaki, A., Tokuraku, K., et al. (2016).
893 Allosteric regulation by cooperative conformational changes of actin
894 filaments drives mutually exclusive binding with cofilin and myosin. Sci. Rep.

895 *6*, 1–11. https://doi.org/10.1038/srep35449.

896 28. Hayakawa, Y., Takaine, M., Ngo, K.X., Imai, T., Yamada, M., Behjat, A.B.,
897 Umeda, K., Hirose, K., Yurtsever, A., Kodera, N., et al. (2022). Actin binding
898 domain of Rng2 sparsely bound on F-actin strongly inhibits actin movement
899 on myosin II. Life Sci. Alliance *6*, e202201469.
900 https://doi.org/10.26508/lsa.202201469.

901 29. Uyeda, T.Q.P., Iwadate, Y., Umeki, N., Nagasaki, A., and Yumura, S. (2011).
902 Stretching actin filaments within cells enhances their affinity for the myosin ii
903 motor domain. PLoS One *6*, e26200.
904 https://doi.org/10.1371/journal.pone.0026200.

905 30. Sharma, S., Grintsevich, E.E., Phillips, M.L., Reisler, E., and Gimzewski, J.K.
906 (2011). Atomic Force Microscopy Reveals Drebrin Induced Remodeling of.
907 825–827.

908 31. Hanein, D., Matsudaira, P., and DeRosier, D.J. (1997). Evidence of a
909 conformational change in actin induced by fimbrin (N375) binding. J. Cell
910 Biol. *139*, 387–396. https://doi.org/10.1017/CBO9781107415324.004.

911 32. Ando, T., Kodera, N., Takai, E., Maruyama, D., Saito, K., and Toda, A.
912 (2001). A high-speed atomic force microscope for studying biological
913 macromolecules. Proc. Natl. Acad. Sci. U. S. A. *98*, 12468–12472.
914 https://doi.org/10.1073/pnas.211400898.

915 33. Ando, T., Uchihashi, T., Kodera, N., Yamamoto, D., Miyagi, A., Taniguchi,
916 M., and Yamashita, H. (2008). High-speed AFM and nano-visualization of
917 biomolecular processes. Pflugers Arch. Eur. J. Physiol. *456*, 211–225.
918 https://doi.org/10.1007/s00424-007-0406-0.

919 34. Ando, T., Fukuda, S., Ngo, K.X., and Flechsig, H. (2024). High-Speed
920 Atomic Force Microscopy for Filming Protein Molecules in Dynamic Action.
921 Annu. Rev. Biophys. *53*, 19–40. https://doi.org/10.1146/annurev-biophys-

922 030722-113353.

923 35. Homma, H., Ngo, K.X., Yoshioka, Y., Tanaka, H., Inotsume, M., Fujita, K.,
924 Ando, T., and Okazawa, H. (2024). PQBP3/NOL7 is an intrinsically
925 disordered protein. Biochem. Biophys. Res. Commun. *736*, 150453.
926 https://doi.org/10.1016/j.bbrc.2024.150453.

927 36. Kodera, N., Noshiro, D., Dora, S.K., Mori, T., Habchi, J., Blocquel, D., Gruet,
928 A., Dosnon, M., Salladini, E., Bignon, C., et al. (2021). Structural and
929 dynamics analysis of intrinsically disordered proteins by high-speed atomic
930 force microscopy. Nat. Nanotechnol. *16*, 181–189.
931 https://doi.org/10.1038/s41565-020-00798-9.

932 37. Fukuda, S., and Ando, T. (2021). Faster high-speed atomic force microscopy
933 for imaging of biomolecular processes. Rev. Sci. Instrum. *92*.
934 https://doi.org/10.1063/5.0032948.

935 38. Shimizu, M., Okamoto, C., Umeda, K., Watanabe, S., Ando, T., and Kodera,
936 N. (2022). An ultrafast piezoelectric Z-scanner with a resonance frequency
937 above 1.1 MHz for high-speed atomic force microscopy. Rev. Sci. Instrum.
938 *93*, 013701. https://doi.org/10.1063/5.0072722.

939 39. Zwier, M.C., and Chong, L.T. (2010). Reaching biological timescales with all-
940 atom molecular dynamics simulations. Curr. Opin. Pharmacol. *10*, 745–752.
941 https://doi.org/10.1016/j.coph.2010.09.008.

942 40. Hollingsworth, S.A., and Dror, R.O. (2018). Molecular dynamics simulation
943 for all. Neuron *99*, 1–29. https://doi.org/10.1016/j.neuron.2018.08.011.

944 41. Karplus, M., and McCammon, J.A. (2002). Molecular dynamics simulations
945 of biomolecules. Nat. Struct. Biol. *9*, 646–652.
946 https://doi.org/10.1038/nsb0902-646.

947 42. Kovermann, M., Rogne, P., and Wolf-Watz, M. (2016). Protein dynamics and

948 function from solution state NMR spectroscopy. Q. Rev. Biophys. *49*, e6.
949 https://doi.org/10.1017/S0033583516000019.

950 43. Hu, Y., Cheng, K., He, L., Zhang, X., Jiang, B., Jiang, L., Li, C., Wang, G.,
951 Yang, Y., and Liu, M. (2021). NMR-Based Methods for Protein Analysis.
952 Anal. Chem. *93*, 1866–1879.
953 https://doi.org/10.1021/acs.analchem.0c03830.

954 44. Golji, J., Collins, R., and Mofrad, M.R.K. (2009). Molecular mechanics of the
955 α-actinin rod domain: Bending, torsional, and extensional behavior. PLoS
956 Comput. Biol. *5*. https://doi.org/10.1371/journal.pcbi.1000389.

957 45. Adcock, S.A., and McCammon, J.A. (2006). Molecular dynamics: Survey of
958 methods for simulating the activity of proteins. Chem. Rev. *106*, 1589–1615.
959 https://doi.org/10.1021/cr040426m.

960 46. Sumino, A., Sumikama, T., Uchihashi, T., and Oiki, S. (2019). High-speed
961 AFM reveals accelerated binding of agitoxin-2 to a K+ channel by induced
962 fit. Sci. Adv. *5*, 1–10. https://doi.org/10.1126/sciadv.aax0495.

963 47. Chu, J.W., and Voth, G.A. (2005). Allostery of actin filaments: Molecular
964 dynamics simulations and coarse-grained analysis. Proc. Natl. Acad. Sci. U.
965 S. A. *102*, 13111–13116. https://doi.org/10.1073/pnas.0503732102.

966 48. Li, M., and Zheng, W. (2013). All-atom molecular dynamics simulations of
967 actin-myosin interactions: A comparative study of cardiac α myosin, β
968 myosin, and fast skeletal muscle myosin. Biochemistry *52*, 8393–8405.
969 https://doi.org/10.1021/bi4006896.

970 49. Yu, I., Mori, T., Ando, T., Harada, R., Jung, J., Sugita, Y., and Feig, M.
971 (2016). Biomolecular interactions modulate macromolecular structure and
972 dynamics in atomistic model of a bacterial cytoplasm. Elife *5*, 1–22.
973 https://doi.org/10.7554/eLife.19274.

974 50. Lindorff-Larsen, K., Piana, S., Dror, R.O., and Shaw, D.E. (2011). How fast-
975 folding proteins fold. Science (80-.). *334*, 517–520.
976 https://doi.org/10.1126/science.1208351.

977 51. Vakser, I.A., Grudinin, S., Jenkins, N.W., Kundrotas, P.J., and Deeds, E.J.
978 (2022). Docking-based long timescale simulation of cell-size protein systems
979 at atomic resolution. Proc. Natl. Acad. Sci. U. S. A. *119*, 1–8.
980 https://doi.org/10.1073/pnas.2210249119.

981 52. Feig, M., and Sugita, Y. (2019). Whole-cell models and simulations in
982 molecular detail. Annu. Rev. Cell Dev. Biol. *35*, 191–211.
983 https://doi.org/10.1146/annurev-cellbio-100617-062542.

984 53. Ando, T., Fukuda, S., Ngo, K.X., and Flechsig, H. (2024). High-Speed
985 Atomic Force Microscopy for Filming Protein Molecules in Dynamic Action.
986 Annu. Rev. Biophys. *53*, 19–39. https://doi.org/10.1146/annurev-biophys-
987 030722-113353.

988 54. Hoffmann, A., and Grudinin, S. (2017). NOLB: Nonlinear Rigid Block Normal-
989 Mode Analysis Method. J. Chem. Theory Comput. *13*, 2123–2134.
990 https://doi.org/10.1021/acs.jctc.7b00197.

991 55. Tama, F., and Sanejouand, Y.H. (2001). Conformational change of proteins
992 arising from normal mode calculations. Protein Eng. *14*, 1–6.
993 https://doi.org/10.1093/protein/14.1.1.

994 56. Tama, F., Valle, M., Frankt, J., and Brooks, C.L. (2003). Dynamic
995 reorganization of the functionally active ribosome explored by normal mode
996 analysis and cryo-electron microscopy. Proc. Natl. Acad. Sci. U. S. A. *100*,
997 9319–9323. https://doi.org/10.1073/pnas.1632476100.

998 57. Vuillemot, R., Pellequer, J., and Grudinin, S. (2024). AFMfit : Deciphering
999 conformational dynamics in AFM data using fast nonlinear NMA and FFT-
1000 based search. bioRxiv. https://doi.org/10.1101/2024.06.03.597083.

1001 58. Shams, H., Golji, J., Garakani, K., and Mofrad, M.R.K. (2016). Dynamic
1002 Regulation of α-Actinin's Calponin Homology Domains on F-Actin. Biophys.
1003 J. *110*, 1444–1455. https://doi.org/10.1016/j.bpj.2016.02.024.

1004 59. Skwarek-Maruszewska, A., Hotulainen, P., Mattila, P.K., and Lappalainen,
1005 P. (2009). Contractility-dependent actin dynamics in cardiomyocyte
1006 sarcomeres. J. Cell Sci. *122*, 2119–2126.
1007 https://doi.org/10.1242/jcs.046805.

1008 60. Martin, T.G., and Kirk, J.A. (2020). Under construction: The dynamic
1009 assembly, maintenance, and degradation of the cardiac sarcomere. J. Mol.
1010 Cell. Cardiol. *148*, 89–102. https://doi.org/10.1016/j.yjmcc.2020.08.018.

1011 61. Tojkander, S., Gateva, G., and Lappalainen, P. (2012). Actin stress fibers -
1012 Assembly, dynamics and biological roles. J. Cell Sci. *125*, 1855–1864.
1013 https://doi.org/10.1242/jcs.098087.

1014 62. Rajan, S., Kudryashov, D.S., and Reisler, E. (2023). Actin Bundles
1015 Dynamics and Architecture. Biomolecules *13*.
1016 https://doi.org/10.3390/biom13030450.

1017 63. Taylor, K.A., Taylor, D.W., and Schachat, F. (2000). Isoforms of α-actinin
1018 from cardiac, smooth, and skeletal muscle form polar arrays of actin
1019 filaments. J. Cell Biol. *149*, 635–645. https://doi.org/10.1083/jcb.149.3.635.

1020 64. Taylor, K. a, and Taylor, D.W. (2008). Formation of 2-D paracrystals of F-
1021 actin on phospholipid layers mixed with quaternary ammonium surfactants.
1022 J. Struct. Biol. *108*, 140–147.

1023 65. Ando, T. (2012). High-speed atomic force microscopy coming of age.
1024 Nanotechnology *23*, 1–27. https://doi.org/10.1088/0957-4484/23/6/062001.

1025 66. Ando, T., Uchihashi, T., and Fukuma, T. (2008). High-speed atomic force
1026 microscopy for nano-visualization of dynamic biomolecular processes. Prog.

1027 Surf. Sci. *83*, 337–437. https://doi.org/10.1016/j.progsurf.2008.09.001.

1028 67. David A. Begg, Richard Rodewald, L.I.R. (1978). The VISUALIZATION OF
1029 ACTIN FILAMENT POLARITY IN THIN SECTIONS Evidence for the
1030 Uniform Polarity of Membrane-Associated Filaments. J. Cell Biol. *79*, 846–
1031 852.

1032 68. Andrianantoandro, E., and Pollard, T.D. (2006). Mechanism of Actin
1033 Filament Turnover by Severing and Nucleation at Different Concentrations
1034 of ADF/Cofilin. Mol. Cell *24*, 13–23.
1035 https://doi.org/10.1016/j.molcel.2006.08.006.

1036 69. Egelman, E.H., Francis, N., and DeRosier, D.J. (1982). F-actin is a helix with
1037 a random variable twist. Nature *298*, 131–135.
1038 https://doi.org/10.1038/298131a0.

1039 70. McGough, A., Pope, B., Chiu, W., and Weeds, A. (1997). Cofilin changes
1040 the twist of F-actin: implications for actin filament dynamics and cellular
1041 function. J. Cell Biol. *138*, 771–781.

1042 71. Galkin, V.E., Orlova, A., Kudryashov, D.S., Solodukhin, A., Reisler, E.,
1043 Schröder, G.F., and Egelman, E.H. (2011). Remodeling of actin filaments by
1044 ADF/cofilin proteins. Proc. Natl. Acad. Sci. U. S. A. *108*, 20568–20572.
1045 https://doi.org/10.1073/pnas.1110109108.

1046 72. Tanaka, K., Takeda, S., Mitsuoka, K., Oda, T., Kimura-Sakiyama, C.,
1047 Maéda, Y., and Narita, A. (2018). Structural basis for cofilin binding and actin
1048 filament disassembly. Nat. Commun. *9*, 1–3. https://doi.org/10.1038/s41467-
1049 018-04290-w.

1050 73. Reynolds, M.J., Hachicho, C., Carl, A.G., Gong, R., and Alushin, G.M.
1051 (2022). Bending forces and nucleotide state jointly regulate F-actin structure.
1052 Nature. https://doi.org/10.1038/s41586-022-05366-w.

1053 74. Voss, J.M., Harder, O.F., Olshin, P.K., Drabbels, M., and Lorenz, U.J.
1054 (2021). Rapid melting and revitrification as an approach to microsecond
1055 time-resolved cryo-electron microscopy. Chem. Phys. Lett. *778*, 138812.
1056 https://doi.org/10.1016/j.cplett.2021.138812.

1057 75. Bongiovanni, G., Harder, O.F., Drabbels, M., and Lorenz, U.J. (2022).
1058 Microsecond melting and revitrification of cryo samples with a correlative
1059 light-electron microscopy approach. Front. Mol. Biosci. *9*, 1–7.
1060 https://doi.org/10.3389/fmolb.2022.1044509.

1061 76. Lorenz, U.J. (2024). Microsecond time-resolved cryo-electron microscopy.
1062 Curr. Opin. Struct. Biol. *87*, 102840.
1063 https://doi.org/10.1016/j.sbi.2024.102840.

1064 77. Vuillemot, R., Miyashita, O., Tama, F., Rouiller, I., and Jonic, S. (2022).
1065 NMMD: Efficient Cryo-EM Flexible Fitting Based on Simultaneous Normal
1066 Mode and Molecular Dynamics atomic displacements. J. Mol. Biol. *434*,
1067 167483. https://doi.org/10.1016/j.jmb.2022.167483.

1068 78. Boehr, D.D., Dyson, H.J., and Wright, P.E. (2006). An NMR perspective on
1069 enzyme dynamics. Chem. Rev. *106*, 3055–3079.
1070 https://doi.org/10.1021/cr050312q.

1071 79. Wolf-Watz, M., Thai, V., Henzler-Wildman, K., Hadjipavlou, G.,
1072 Eisenmesser, E.Z., and Kern, D. (2004). Linkage between dynamics and
1073 catalysis in a thermophilic-mesophilic enzyme pair. Nat. Struct. Mol. Biol. *11*,
1074 945–949. https://doi.org/10.1038/nsmb821.

1075 80. Purslow, J.A., Khatiwada, B., Bayro, M.J., and Venditti, V. (2020). NMR
1076 Methods for Structural Characterization of Protein-Protein Complexes.
1077 Front. Mol. Biosci. *7*, 1–8. https://doi.org/10.3389/fmolb.2020.00009.

1078 81. Camacho-Zarco, A.R., Schnapka, V., Guseva, S., Abyzov, A., Adamski, W.,
1079 Milles, S., Jensen, M.R., Zidek, L., Salvi, N., and Blackledge, M. (2022).

1080 NMR Provides Unique Insight into the Functional Dynamics and Interactions
1081 of Intrinsically Disordered Proteins. Chem. Rev. *122*, 9331–9356.
1082 https://doi.org/10.1021/acs.chemrev.1c01023.

1083 82. Moraes, A.H., and Valente, A.P. (2023). Conformational dynamics and
1084 kinetics of protein interactions by nuclear magnetic resonance. J. Magn.
1085 Reson. Open *14–15*, 100093. https://doi.org/10.1016/j.jmro.2023.100093.

1086 83. Murata, K., and Wolf, M. (2018). Cryo-electron microscopy for structural
1087 analysis of dynamic biological macromolecules. Biochim. Biophys. Acta -
1088 Gen. Subj. *1862*, 324–334. https://doi.org/10.1016/j.bbagen.2017.07.020.

1089 84. Gauto, D.F., Estrozi, L.F., Schwieters, C.D., Effantin, G., Macek, P., Sounier,
1090 R., Sivertsen, A.C., Schmidt, E., Kerfah, R., Mas, G., et al. (2019). Integrated
1091 NMR and cryo-EM atomic-resolution structure determination of a half-
1092 megadalton enzyme complex. Nat. Commun. *10*, 1–12.
1093 https://doi.org/10.1038/s41467-019-10490-9.

1094 85. Schanda, P., and Haran, G. (2024). NMR and Single-Molecule FRET
1095 Insights into Fast Protein Motions and Their Relation to Function. Annu. Rev.
1096 Biophys. *53*, 247–273. https://doi.org/10.1146/annurev-biophys-070323-
1097 022428.

1098 86. Murakami, K., Yasunaga, T., Noguchi, T.Q.P., Gomibuchi, Y., Ngo, K.X.,
1099 Uyeda, T.Q.P., and Wakabayashi, T. (2010). Structural basis for actin
1100 assembly, activation of ATP hydrolysis, and delayed phosphate release. Cell
1101 *143*, 275–287. https://doi.org/10.1016/j.cell.2010.09.034.

1102 87. González, M.A. (2011). Force fields and molecular dynamics simulations.
1103 Collect. SFN *12*, 169–200. https://doi.org/10.1051/sfn/201112009.

1104 88. Chmiela, S., Sauceda, H.E., Müller, K.R., and Tkatchenko, A. (2018).
1105 Towards exact molecular dynamics simulations with machine-learned force
1106 fields. Nat. Commun. *9*, 1–10. https://doi.org/10.1038/s41467-018-06169-2.

1107 89. Bhavna, R., and Sonawane, M. (2023). A deep learning framework for
1108 quantitative analysis of actin microridges. npj Syst. Biol. Appl. *9*, 1–15.
1109 https://doi.org/10.1038/s41540-023-00276-7.

1110 90. Degenhardt, M.F.S., Degenhardt, H.F., Bhandari, Y.R., Lee, Y., Ding, J., Yu,
1111 P., Heinz, W.F., Stagno, J.R., Schwieters, C.D., Watts, N.R., et al. (2025).
1112 Determining structures of RNA conformers using AFM and deep neural
1113 networks. Nature *637*. https://doi.org/10.1038/s41586-024-07559-x.

1114 91. Vinh, T., Nguyen, T., Ly, N.Q., Thi, N., and Le, P. (2025). Developing the
1115 Computational Image Processing Method for Quantitative Analysis of
1116 Nanopore Structure Obtained from HS-AFM (AFMnanoQ). bioRxiv.
1117 https://doi.org/10.1101/2025.02.26.640237.

1118 92. Jiang, Y., Wang, Z., and Scheuring, S. (2025). A structural biology
1119 compatible file format for atomic force microscopy. Nat. Commun. *16*, 1–16.
1120 https://doi.org/10.1038/s41467-025-56760-7.

1121 93. Sumikama, T., Fukuma, T., Canova, F.F., Gao, D.Z., Penedo, M., Miyazawa,
1122 K., and Foster, A.S. (2022). Computed Three-Dimensional Atomic Force
1123 Microscopy Images of Biopolymers Using the Jarzynski Equality. J. Phys.
1124 Chem. Lett. *13*, 5365–5371. https://doi.org/10.1021/acs.jpclett.2c01093.

1125 94. Amyot, R., and Flechsig, H. (2020). BioAFMviewer: An interactive interface
1126 for simulated AFM scanning of biomolecular structures and dynamics. PLoS
1127 Comput. Biol. *16*, 1–12. https://doi.org/10.1371/journal.pcbi.1008444.

1128

1129

1130

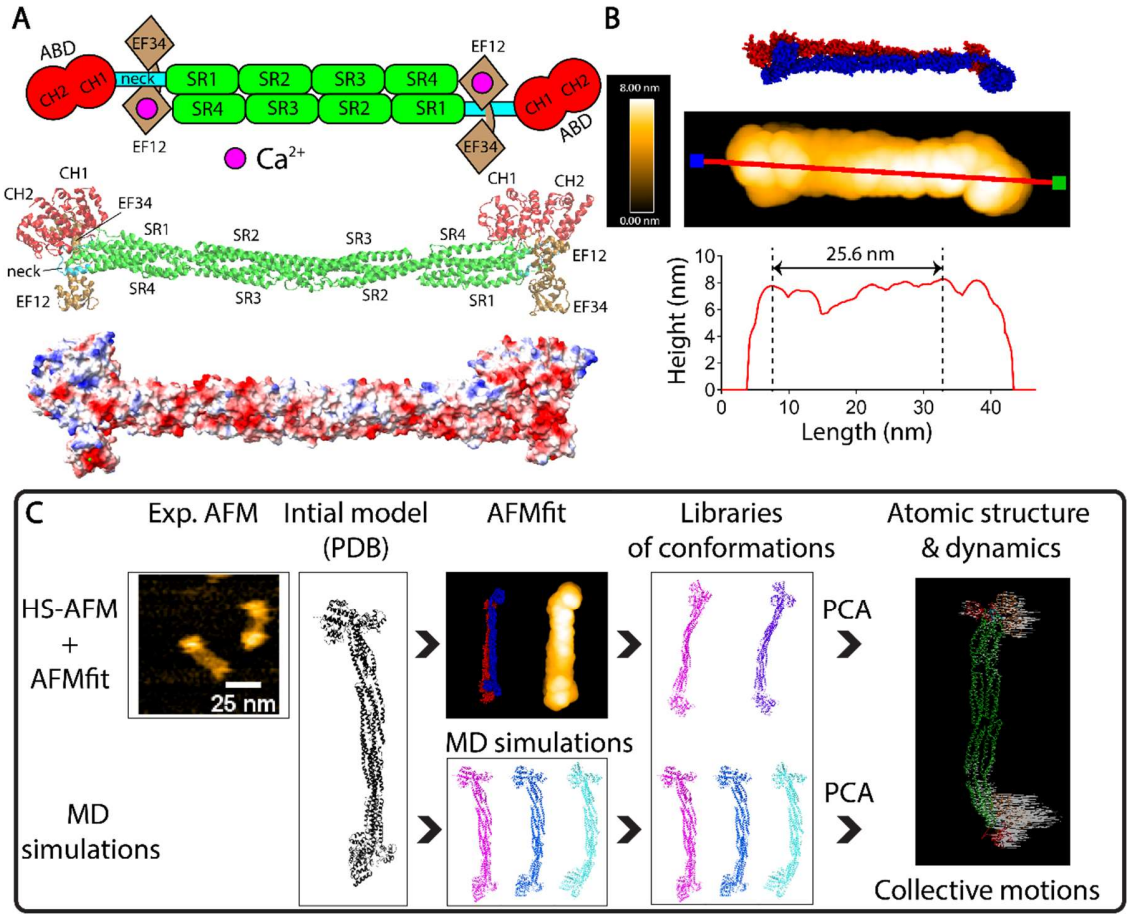

Figure 1 Novel workflow for analyzing the dynamics and atomic structures of alpha-actinin through the integration of HS-AFM with the AFMfit and MD simulations.

1135 (**A**) Domain composition and structure of chicken gizzard smooth muscle alpha-
1136 actinin (PDB: 1SJJ) depicted in a ribbon model and an electrostatic surface
1137 potential model. In the latter, red and blue represent negative and positive charges,
1138 respectively. Alpha-actinin is an antiparallel homodimer with a molecular weight
1139 exceeding 200 kDa. It comprises an N-terminal actin binding domain (ABD), in
1140 which the two calponin homology 1 and 2 (CH1, CH2) domains are in extensive
1141 contact, a central region containing four spectrin-like repeat (SR1-SR4) or rod
1142 domains, and a C-terminal calmodulin-like domain (CaMD) that includes two pairs
1143 of EF-hand motifs (EF12 and EF34). The EF12 domain is responsible for the Ca^{2+}
1144 binding. The two ABDs undergo a 90-degree rotation, enabling alpha-actinin to
1145 crosslink the actin filaments in nearly any orientation.
1146 (**B**) Pseudo-AFM images and topographic cross-sectional profile of alpha-actinin
1147 generated with the AFM viewer[94]. The pseudo-AFM images were obtained with
1148 the following scan parameters: step size, 0.1 nm; cone angle, 5°; and tip radius,
1149 2.0 nm. The cross-sectional profile in the bottom panel corresponds to the red line
1150 in the middle panel.
1151 (**C**) Workflow for developing libraries of conformations, storing them as PDB files,
1152 and analyzing the dynamics and atomic structures of alpha-actinin through the
1153 integration of HS-AFM with the AFMfit and molecular dynamics (MD) simulations.
1154 This process is followed by principal component analysis (PCA) to identify and
1155 classify dynamic atomic structures into distinct modes of collective motion
1156 (indicated by white arrows).

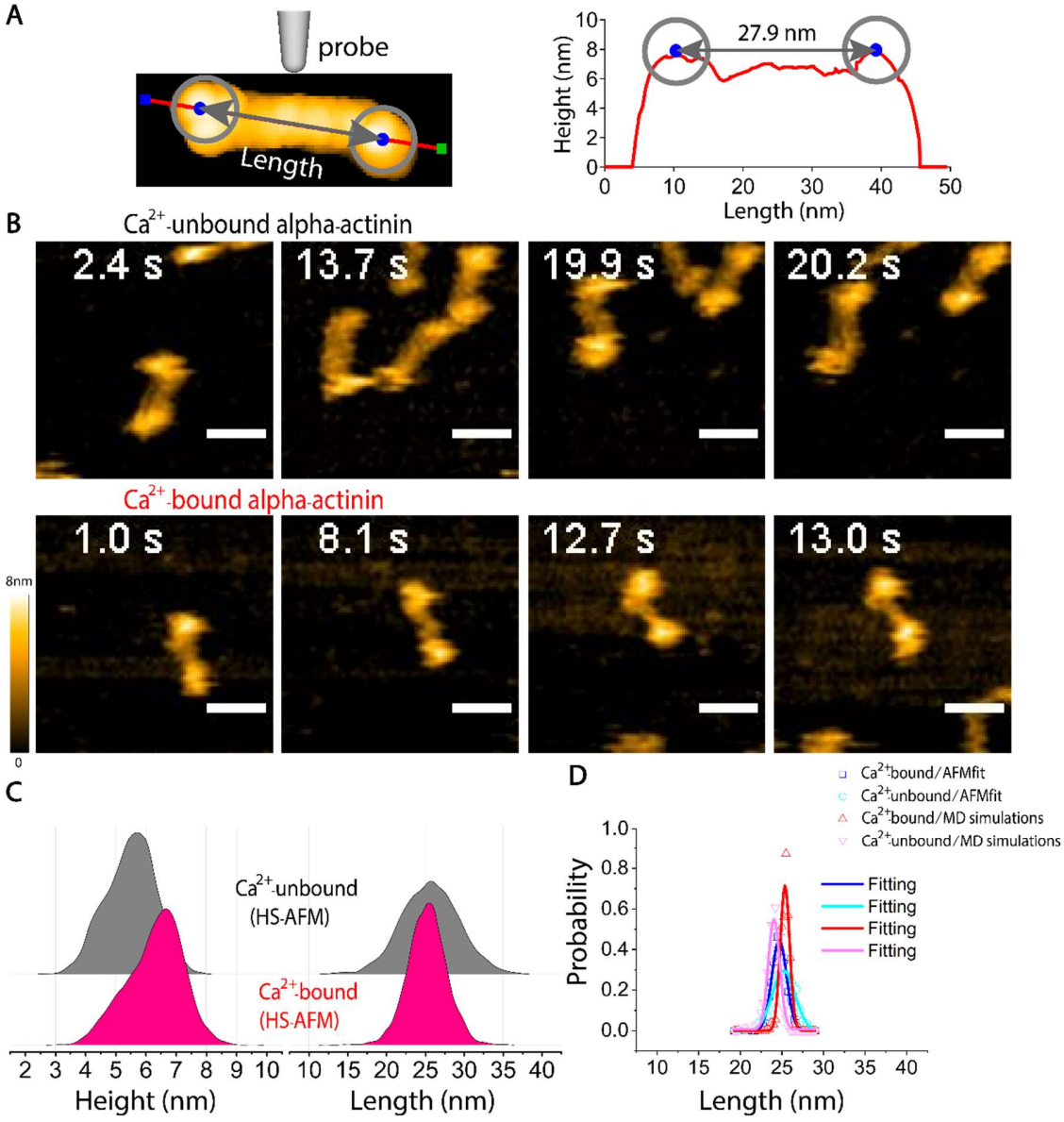

Figure 2 Ca^{2+} binding influencing the flexibility of the length of smooth muscle alpha-actinin, as analyzed using HS-AFM combined with the AFMfit and MD simulations.

(**A**) Illustration of the measurement of the length between the two spheres on the opposite sides of alpha-actinin, as shown in **Figure 1B**. The distance is calculated between the two peaks (blue), which are automatically detected within the region of interest (circles). The longitudinal section profile (right) displays the height and length measurements along the red line (left).

(**B**) HS-AFM still images showing the various physical motions of alpha-actinin, such as twisting and bending, with and without Ca^{2+} binding. Scale bars: 25 nm. Color scale: 0–8 nm.

(**C**) Ridgeline plots displaying the distribution of the peak heights and lengths between the two ABDs for Ca^{2+}-bound and Ca^{2+}-unbound alpha-actinin obtained with HS-AFM. A two-sample *t test* ($p \leq 0.05$) indicates that the differences in the distributions of the height and length between the bound and unbound states are significant ($p = 0$ for height, $p = 7.45454 \times 10^{-7}$ for length).

(**D**) Plot showing the length distributions between the two centers of mass of the CH1-CH2 and EF12-EF34 domains located on the opposite sides of alpha-actinin using data from the atomic conformations obtained from the AFMfit and MD simulations for both the Ca^{2+}-bound and Ca^{2+}-unbound states. The mean ± SD lengths were determined through single Gaussian fitting. A two-sample *t test* ($p \leq 0.05$) confirmed that the differences in the distributions of the length between the Ca^{2+}-bound and Ca^{2+}-unbound states were statistically significant ($p = 8.9 \times 10^{-28}$ for the AFMfit data; $p = 0$ for the MD simulations).

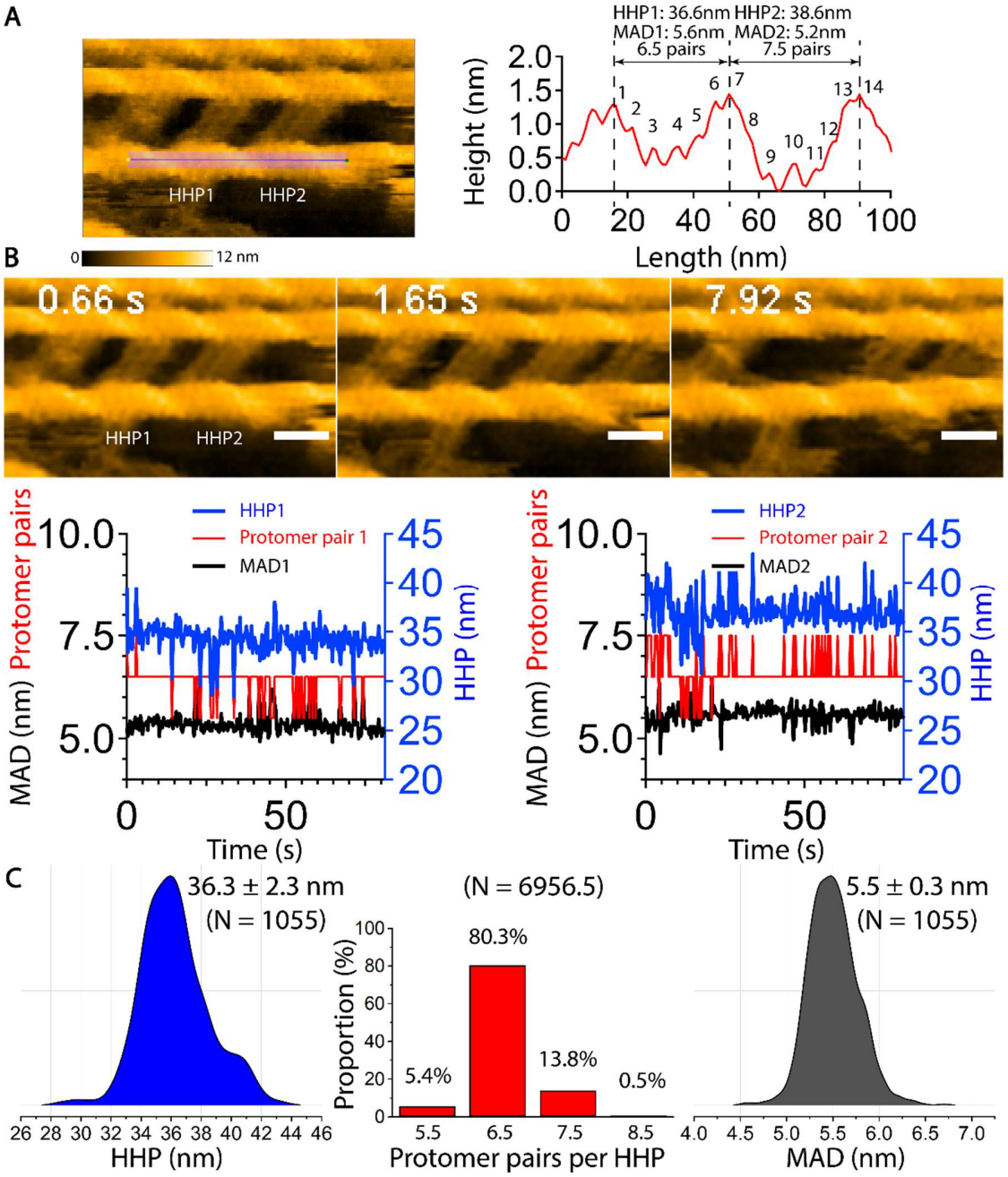

Figure 3 HS-AFM-based analysis of the dynamic conformation of the actin filaments crosslinked with alpha-actinin in a unipolar configuration in the presence of ATP, Ca^{2+}, and S1.

(**A**) Longitudinal section profile illustrating the analysis of the magnitudes of the two adjacent HHPs, the number of protomer pairs per HHP, and the MADs in various actin filaments captured at different time points with still AFM images. The analytic methods employed were developed previously[25].
(B) Time-dependent changes in the magnitudes of two adjacent HHPs, the number of protomer pairs per HHP, and the MADs in the actin filaments crosslinked with 50 nM α-actinin in the presence of 1 mM ATP, 0.1 mM $CaCl_2$, and 1 μM S1 but without $MgCl_2$. Scale bars: 25 nm. Color scale: 0–12 nm.
(C) Ridgeline and bar plots displaying the distribution of the magnitude of the HHPs, the number of the protomer pairs per HHP, and the MADs, as well as the corresponding number of events (N) (1055, 6956.5, and 1055, respectively).

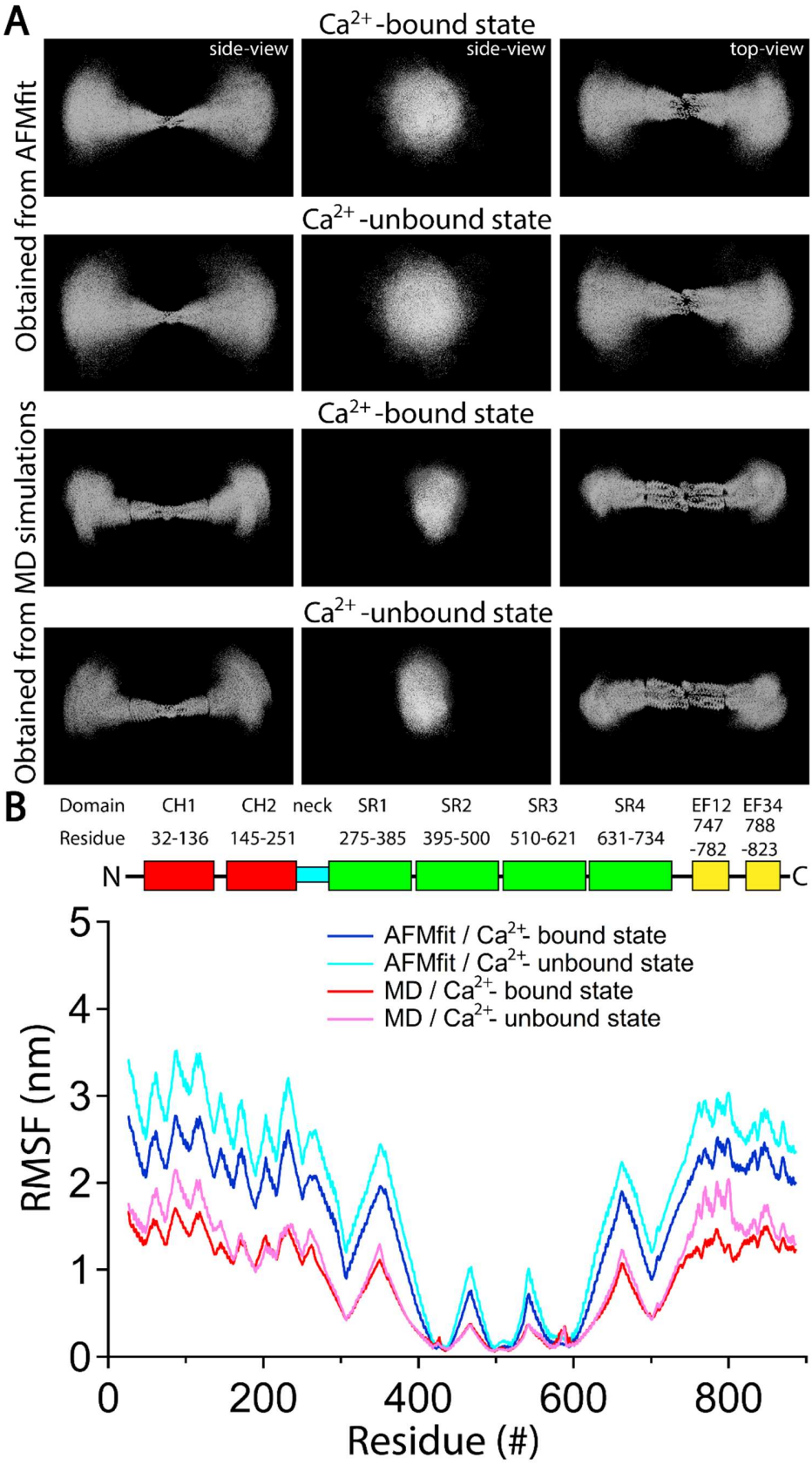
A
Ca2+-bound state
side-view
side-view
top-view
Ca2+-unbound state
Obtained from AFMfit
Ca2+-bound state
Ca2+-unbound state
Obtained from MD simulations
B
Domain
CH1
CH2
neck
SR1
SR2
SR3
SR4
EF12
EF34
Residue
32-136
145-251
275-385
395-500
510-621
631-734
747 -782
788 -823
N
C
AFMfit / Ca2+- bound state
AFMfit / Ca2+- unbound state
MD / Ca2+- bound state
MD / Ca2+- unbound state
RMSF (nm)
0
1
2
3
4
5
0
200
400
600
800
Residue (#)

1223

1224 **Figure 4** Analyses of the dynamics and atomic structure of the Ca^{2+}-bound and
1225 unbound alpha-actinin using HS-AFM combined with the AFMfit and MD
1226 simulations.
1227 (**A**) Positions of the Cα atoms from the libraries of the Ca^{2+}-bound and Ca^{2+}-
1228 unbound alpha-actinin conformations obtained from the AFMfit and MD
1229 simulations. The conformations were aligned, assuming that the helical elements
1230 in the SR2 and SR3 domains (residues 485-525) exhibited the lowest root mean
1231 square fluctuation (RMSF). Top views and two different side views are presented
1232 to compare the molecular dynamics among the states and conformation libraries.
1233 (**B**) RMSF values plotted against the residue number. The illustration of the alpha-
1234 actinin domains, along with their corresponding amino acid residues, is based on
1235 PDB ID 1SJJ, using colors consistent with those in **Figure 1**. From the N-terminus
1236 to the C-terminus: CH1, CH2: calponin homology 1 and 2; SR1-SR4: spectrin-like
1237 repeat 1-4; and EF12, EF34: EF hand motifs 12, 34.
1238
1239
1240
1241
1242
1243
1244

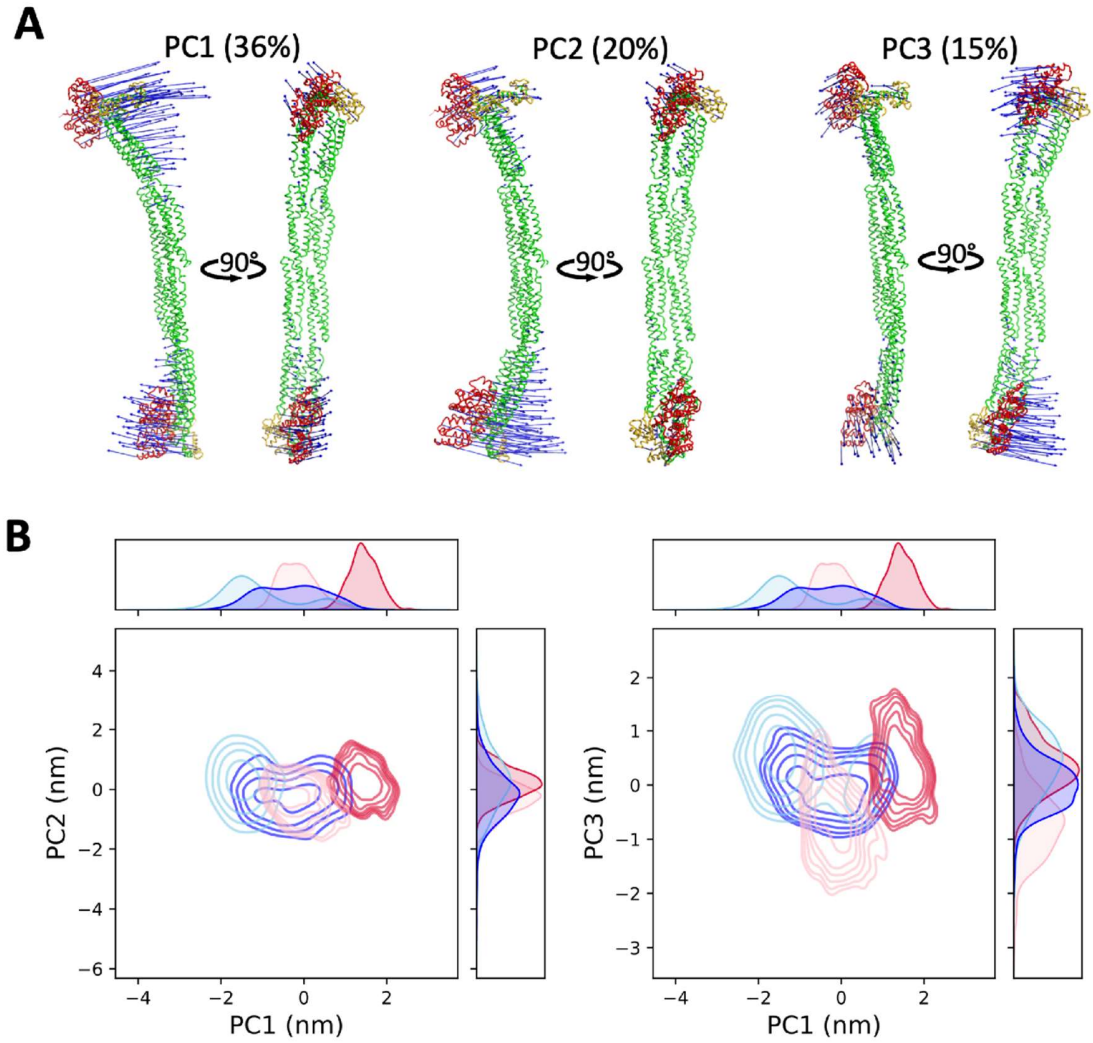

Figure 5 AFMfit and MD simulations projected onto a common PCA space consistently capturing the ensemble motions of the atomic conformations and distributions of alpha-actinin in the Ca^{2+}-bound and Ca^{2+}-unbound states.

1249 (**A**) Ensemble motions of the atomic conformations of alpha-actinin projected onto
1250 a common PCA space according to the conformational libraries of Ca^{2+}-bound and
1251 Ca^{2+}-unbound alpha-actinin obtained from the AFMfit and MD simulations. The
1252 eigenvalues of the principal components (PC1, PC2, PC3) were used to calculate
1253 the contributions (in percentages) of each motion to the total motions of alpha-
1254 actinin in the two states. The alpha-actinin structures are illustrated in the tube
1255 conformations, with the ABD, neck, rod, and EF12-EF34 domains represented in
1256 red, cyan, green, and yellow, respectively; the eigenvectors indicating the direction
1257 of motion are shown with blue arrows.
1258 (**B**) Distributions of PC1 and PC2 (left) and PC1 and PC3 (right). The values
1259 derived from the conformational libraries obtained from the AFMfit and MD
1260 simulations are plotted in blue and red, respectively. Light blue and light red
1261 represent the PCs obtained from the libraries corresponding to the Ca^{2+}-unbound
1262 state, whereas dark blue and dark red represent the PCs obtained from the
1263 libraries corresponding to the Ca^{2+}-bound state.
1264
1265
1266
1267
1268
1269
1270
1271
1272
1273
1274
1275
1276
1277
1278
1279

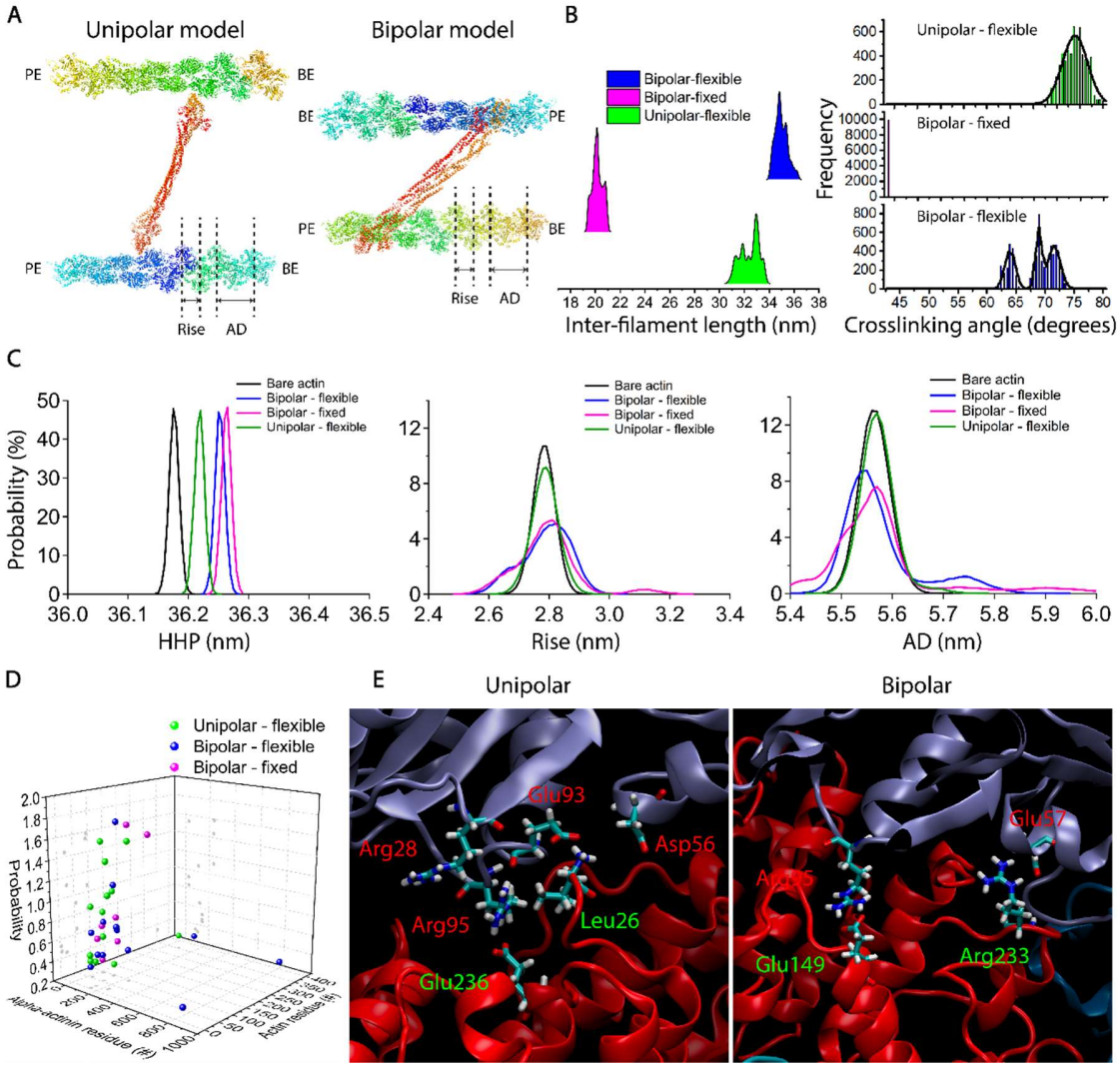

Figure 6 Differences in the conformational changes in the actin filaments crosslinked with alpha-actinin in unipolar and bipolar models, including rise, AD, and residue-level interactions. (**A**) Illustrations of the unipolar and bipolar crosslinking models of the actin filaments with alpha-actinin. The unipolar crosslinking configuration occurs when the actin filaments share the same polarity, whereas the bipolar crosslinking configuration appears when the actin filaments align with opposite polarities. The rise and AD analyses were performed using conformations obtained from MD simulations. See the definitions of rise and AD in the Supplementary Methods.

(**B**) Quantitative analysis of the inter-filament lengths and alpha–actin crosslinking angles relative to the filament axis in the unipolar-flexible, bipolar-flexible, and bipolar-fixed models obtained from the MD simulations. In these models, the flexible condition allowed all Cα atoms in alpha-actinin to vibrate freely, while the fixed condition computationally constrained them.

(**C**) Analysis of the HHP, rise, and AD in the bare actin filaments and in the unipolar-flexible, bipolar-flexible, and bipolar-fixed models using the conformations derived from the MD simulations.

(**D, E**) Characterization of the residue-level interactions between the alpha-actinin ABDs and actin protomers during crosslinking in the unipolar-flexible and bipolar-flexible models. If an atom of one residue was in contact within 2 Å of an atom of another residue, these two residues were considered to be interacting. The probability of the residue contacts, time averaged contact probability, was calculated as the combined sum of interactions between the two alpha-actinin ABDs (green texts) and actin (red texts) residues, resulting in a maximum value of 2. Related to **Table S10**.

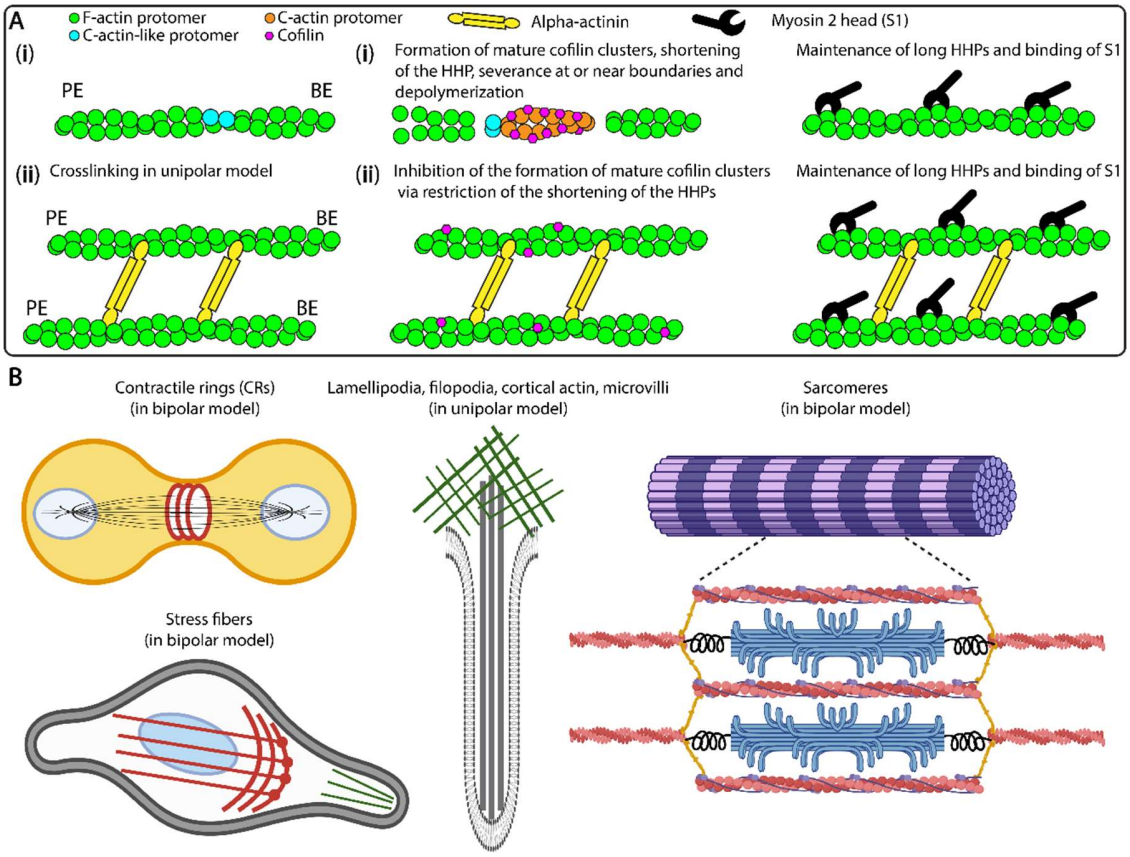

Figure 7 Hypothesis outlining the configurations, functions, and localizations of the actin filaments and their crosslinking with alpha-actinin in both unipolar and bipolar models.

(**A**) Summary of our experimental findings on how the actin filaments and crosslinking of the unipolar actin filaments with alpha-actinin regulate the binding of S1 and cofilin.

(**B**) Illustration depicting the unipolar and bipolar crosslinking conformations, highlighting their distinct localizations and functions within cells. This figure was created using BioRender.com. Related to **Table S2**.

Supplementary Information for

Atomic Conformational Dynamics and Actin-Crosslinking Function of Alpha-Actinin Revealed by SimHS-AFMfit

Kien Xuan Ngo, Takashi Sumikama, Rémi Vuillemot, Han Gia Nguyen, Taro QP Uyeda, Ngan Thi Phuong Le, Sergei Grudinin

Email:

ngoxuankien@staff.kanazawa-u.ac.jp

sumi@staff.kanazawa-u.ac.jp

remi.vuillemot@univ-grenoble-alpes.fr

sergei.grudinin@univ-grenoble-alpes.fr

This PDF file includes:

- Supplementary Information Text
- Figures S1 to S14
- Tables S1 to S10
- Videos S1 to S20
- Supplementary References

Source Video

https://drive.google.com/drive/folders/1OX7NmnHoftt5swuxmw1WlzegKFTV6bJE?usp=sharing

1365 **Supplementary Information**

1366 **Materials and Methods**

1367 ***Proteins and lipids***

1368 Rabbit skeletal actin and human (hs) cofilin 1 were prepared following the
1369 same protocol as in our previous study[1]. Chicken gizzard smooth muscle alpha-
1370 actinin (isoform 2)[2] was obtained from Cytoskeletons (Sigma, Japan).
1371 Subfragment-1 (S1) was prepared from smooth muscle myosin using the method
1372 described by Asakasa et al[3].

1373 The lipid compositions used in this study consisted of neutral 1,2-
1374 dipalmitoyl-sn-glycero-3-phosphocholine (DPPC, Avanti) and positively charged
1375 1,2-dipalmitoyl-3-trimethylammonium-propane (DPTAP, Avanti). Liposomes were
1376 prepared with a DPPC/DPTAP ratio of 90:10 (wt%), and the lipid membrane was
1377 subsequently formed on mica[1].

1378 ***HS-AFM Analysis***

1379 We employed high-speed atomic force microscopy (HS-AFM), as
1380 previously described[1,4,5], to capture the dynamic conformations of alpha-actinin in
1381 various states, providing high-speed imaging and two-dimensional (2D) surface
1382 structure of the protein at nanometer resolution. Chicken gizzard smooth muscle
1383 alpha-actinin, an isoform 2 (Sigma, Japan), was diluted to 30 nM and imaged in F-
1384 buffer containing 20 mM KCl, 10 mM PIPES-KOH (pH 6.8), 0.5 mM $MgCl_2$, 0.25
1385 mM EGTA, 0.25 mM DTT, and 0.5 mM ATP. To observe the dynamic
1386 conformational changes in alpha-actinin with $CaCl_2$, the proteins were imaged in
1387 the same F-buffer with addition of 0.1-0.2 mM $CaCl_2$.

1388 To investigate the dynamic conformational changes in actin filaments
1389 crosslinked solely by alpha-actinin, actin filaments were gently immobilized on a
1390 lipid membrane and F-buffer consisting of 0.5 mM $MgCl_2$, 0.5 mM ATP, and 50 nM
1391 alpha-actinin, but without $CaCl_2$, was employed for HS-AFM imaging. In all
1392 experiments, actin filaments were immobilized on DPPC/DPTAP ratio of 90:10
1393 (wt%) for HS-AFM imaging, as done in our previous study[1].

1394 To study the dynamic conformational changes in actin filaments crosslinked
1395 by alpha-actinin in the presence of myosin II heads (S1), actin filaments were
1396 gently immobilized on a lipid membrane and immersed in F-buffer containing 1 mM
1397 ATP, 0.1 mM $CaCl_2$, 50 nM alpha-actinin, and 1 μM S1, but without $MgCl_2$, for HS-
1398 AFM imaging.

1399 To study the competitive interactions between cofilin and S1, which utilize
1400 distinct short and long helical structures on the same actin filament to form their
1401 respective clusters, actin filaments were gently immobilized on a lipid membrane.
1402 HS-AFM imaging was performed in an F-buffer initially containing 1 mM ADP, 0.01
1403 mM ATP, and 300 nM S1, followed by the addition of 100 nM cofilin.

1404 To explore the binding and supertwisting activities of cofilin clusters on the
1405 half-helices of actin filaments without and with alpha-actinin crosslinking, actin
1406 filaments were gently immobilized on a lipid membrane, either without or with 400
1407 nM alpha-actinin crosslinking in F-buffer containing 1 mM ATP, followed by the
1408 addition of 600 nM hs cofilin, for HS-AFM imaging.

1409 The half helical pitch (HHP), the number of protomer pairs per HHP, and
1410 the mean axial distance (MAD) between adjacent actin protomers along the same
1411 long-pitch strand within individual HHPs were analyzed for actin filaments
1412 crosslinked by alpha-actinin under conditions containing Ca^{2+}, ATP, and S1, but
1413 without $MgCl_2$ were analyzed using HS-AFM (**Figures 3, S1**). The analytical
1414 methods used in this study were adapted from our previous research[1,4].

1415 ***AFMfit Analysis***

1416 AFMfit was originally developed for fitting 3D atomic structures into 2D AFM
1417 images[6]. In this study, AFMfit utilized the same PDB files as the initial models used
1418 in MD simulations. The models were derived from PDB entry 1SJJ[7] for both Ca^{2+}-
1419 bound and Ca^{2+}-unbound states, serving as a reference atomic model.

1420 AFMfit started by cropping AFM images into sub-images (referred to as
1421 particles) that corresponded to the molecule of interest. This operation was semi-
1422 automatic, a first automatic process identifies putative particles using the particle-
1423 tracking toolkit TrackPy (Allan, D. B., Caswell, T., Keim, N. C., van der Wel, C. M.,

& Verweij, R. W. (2021). soft-matter/trackpy: Trackpy v0.5.0 (v0.5.0). Zenodo. https://doi.org/10.5281/zenodo.4682814), then, we performed a manual double check to remove false positives.

The extracted particles were processed with AFMfit. It estimated the optimal rigid and flexible alignments of the model that maximize the similarity between the particles and pseudo-AFM images calculated from the atomic model. The calculation of pseudo-AFM images needed to be adjusted to experimental conditions. Particularly, the shape of the experimental probe tip needed to be estimated to accurately account for the tip-convolution effect. We performed this estimation by an exhaustive search of a smoothness parameter of the pseudo-AFM image calculation over the entire set of particles.

AFMfit proceeded in two steps. In the first step, it performed a rigid-body pre-alignment of the model to the particles using an FFT-accelerated 5D exhaustive search that estimated the relative position (two translational degrees of freedom) and orientation (three rotational degrees of freedom) of each particle. The angular step for rotational search was set to 10° and restricted to flat orientations of alpha-actinin to accelerate the computations. The translational step in the z-direction was set to 1 Å.

In the second step, it combined the continuous rigid and flexible alignments of the model to the particle using the non-linear normal mode analysis method NOLB[8]. NOLB calculated normal modes using the Rotation-Translation of Blocks (RTB) approximation on an Elastic Network Model (ENM). The interaction cutoff in the ENM is set to 8 Å. We restricted the possible motions of our model to the sixteen lowest frequency normal modes, among which, ten modes were the flexible motions describing the most collective motions of alpha-actinin including bending and twisting. The six normal modes left corresponded to rigid translations and rigid rotations in 3D, which were used to account for continuous rigid rearrangement that could be necessary when flexibly deformating the model. According to the AFMfit method, we iteratively calculated the optimal linear approximation of the normal mode displacement that fitted the particle. Then, we carried out a non-linear

extrapolation of the motion following the NOLB methodology. We iterated over the linear approximation and non-linear extrapolation until convergence, which in practice was obtained in five iterations.

The flexible fitting procedure balanced between minimizing the deformations toward the initial model (to preserve the structure and avoid unfeasible distortions) and maximized the similarity to the data. This balance was controlled by a hyperparameter λ. We estimated λ with an exhaustive search by performing the flexible fitting over a sample of particles with the objective of allowing a maximum of 10 Å of average root-mean-square deviation (RMSD) toward the initial model. The value of 10 Å was set to roughly adjust to the range of motion typically observed in MD simulations of alpha-actinin. The optimal value was obtained for λ=7.5 (**Figure S6**).

MD Simulations

Molecular dynamics (MD) simulations were performed to generate libraries of conformations for Ca^{2+}-bound and Ca^{2+}-unbound alpha-actinin and bipolar and unipolar crosslinking models.

The initial models for alpha-actinin with and without Ca^{2+} in the bulk system were made from the PDB entry 1SJJ. The alpha-actinin was solvated in a 30 mM KCl solution. The system without Ca^{2+} consists of one alpha-actinin, 182 K^+, 128 Cl^-, and 251,756 water molecules. In the system with Ca^{2+}, four K^+ were removed and two Ca^{2+} were placed at the center of C_γ of Asp768 and Asp771. It was confirmed that Ca^{2+} ions are stably bound to Asp residues during the simulation. The histidine residues were assumed to be in the protonation state at pH = 7, since they face the bulk solution. The size of the system was 168.856 × 325.387 × 144.838 $Å^3$. AMBER ff19SB[9], TIP3P[10], the Li and Merz 12-6[11], the Li and Merz 12-6-4[12] models were employed for the proteins, water molecules, monovalent ions, and divalent ions, respectively. The system was equilibrated by 1 ns MD simulations with constant temperature (300 K) and pressure conditions (1 bar), followed by 10 ns MD simulations with constant temperature (300 K) and volume conditions. All MD simulations were performed using AMBER22 (D. A. Case, H.

M. Aktulga, K. Belfon, I. Y. Ben-Shalom, J. T. Berryman, S. R. Brozell, D. S. Cerutti, T. E. Cheatham, I. G. A. Cisneros, V. W. D. Cruzeiro, T. A. Darden, N. Forouzesh, G. Giambasу, T. Giese, M. K. Gilson, H. Gohlke, A. W. Goetz, J. Harris, S. Izadi, S. A. Izmailov, et al., AMBER22; University of California: San Francisco, 2022). A Berendsen thermostat[13] was used to control the temperature, and a Monte Carlo barostat with anisotropic scaling was used to control the pressure. The SHAKE algorithm[14] was used to keep the bond length having H atoms constant, enabling the use of a time step of 2 fs. The periodic boundary condition was imposed, and long-range interactions were calculated by the particle mesh Ewald method[15] with a 10 Å cutoff in real space. After the equilibration, the MD simulation was performed for 500 ns with constant temperature at 300 K and volume conditions using the Berendsen thermostat[13]. The trajectories were saved at each 1 ns to generate 500 configuration libraries, which were used to analyse principal component (PC) modes using principal component analysis (PCA) to capture the bending and twisting angles, and distances between domains.

For the unipolar and bipolar systems, two actin fibers crosslinked by an alpha-actinin, the initial coordinates were originally given in the Liu and Taylor' paper[7]. The link in the paper to download the structures is not available now, so a corresponding author, Kenneth A. Taylor, gifted them to us. In the previous calculation using QM/MM[16], water coordination around Mg^{2+} and ADP in the actin protomer was investigated. First, a protomer (PDB code: 8d15)[17] was solvated in a 20 mM NaCl solution with one Mg^{2+} and one ADP. The system consists of one protomer, 73 Na^{+}, 63 Cl^{-}, 1 Mg^{2+}, one ADP, and 23,442 water molecules. For the protein, water molecules, monovalent ions, and divalent ions, the same force fields as in the case of alpha-actinin simulations were used. The Carlson model was employed for ADP[18]. The system was equilibrated by 100 ps MD simulation with constant temperature (300 K) and pressure conditions (1 bar). The actin protomer, ADP, and Mg^{2+} were constrained with a force constant of 10 kcal/mol/$Å^2$ to their original positions. Then, 3 μs MD simulation with constant temperature (300 K) and volume conditions (1 bar) was performed. The actin protomer, ADP, and Mg^{2+} were

1514 weakly constrained with a force constant of 0.2 kcal/mol/Å^2 to prevent unwanted
1515 large structural change in the bulk solution. Water molecules gradually entered the
1516 protomer over 2 μs. The coordination of water molecules around Mg^{2+} and ADP
1517 was confirmed to be similar to the previous configuration obtained by QM/MM
1518 calculation[16]. In the remaining 1 μs simulation, the number of water molecules
1519 around Mg^{2+} has fluctuated but did not change. The protomer, ADP, Mg^{2+}, and 27
1520 water molecules around Mg^{2+} were picked up and aligned to the Liu and Taylor'
1521 configuration by minimizing RMSD between C_α atoms[7]. Then, protomers were
1522 elongated while considering the symmetry to form 36 nm fiber, and the fiber in a
1523 vacuum while the periodic boundary condition was imposed was minimized to
1524 remove bad contacts. In the Liu and Taylor' configuration, a part of the neck
1525 domain in the alpha-actinin (residue 251-260) was missing, which was
1526 complemented by the Modeller package[19]. The system consisting of two actin
1527 fibers and alpha-actinin in a vacuum while the periodic boundary condition was
1528 imposed was minimized and then solvated in a 40 mM KCl solution. The final
1529 system of unipolar configuration consists of two actin fibers (26 protomers), one
1530 alpha-actinin, 1032 K^+, 718 Cl^-, 26 Mg^{2+}, 26 ADP, and 1,433,011 water molecules,
1531 and total number of atoms in the system was 4,479,739. The system was shortly
1532 optimized with 1000 step minimization and was equilibrated by 130 ps MD
1533 simulation with constant temperature (300 K) and pressure conditions (1 bar). The
1534 temperature gradually increased up to 300 K. The pressure was anisotropically
1535 controlled so that only the box size in z direction was allowed to move, in which
1536 the actin fiber was placed along the x direction. During the equilibration, the actin
1537 fiber, the alpha-actinin, Mg^{2+}, ADP, and water molecules inside the actin were
1538 constrained with a force constant of 2 kcal/mol/Å^2. The size of the equilibrated
1539 system was 360.000 × 480.809 × 260.784 Å^3. Then, the constraint was turned off
1540 and only the box size along the x direction was allowed to move to observe the
1541 fluctuation of half helical pitch (HHP), rise, and axial distance (AD) between
1542 adjacent protomers along the same long-pitch strand. 100 ns MD simulation was
1543 similarly performed for flexible and frozen alpha-actinin in the unipolar crosslinking

model, and the trajectories saved at 100 ps were used for the analyses. In the same way, the system was built and the simulation was performed for the bipolar configuration, but the number of water molecules was 1,432,853. To build a bare actin fiber system, the alpha-actinin was removed from the unipolar system, and 100 ps MD simulation with constant temperature (300 K) and pressure conditions (1 bar) was performed to fill the space originally located by the alpha-actinin. MD simulations were similarly performed for 100 ns.

Principal component analysis

Before the PCA, the configuration of alpha-actinin was aligned assuming that C_α atoms in the center part of the rod domain (residue 485-525) have the lowest root mean square fluctuation (RMSF).

To compare the conformational library of AFMfit and MD simulations for Ca^{2+}-bound and Ca^{2+}-unbound states, we chose to reduce the dimensionality of the libraries using PCA. We normalized the number of elements in the four conformational libraries of AFMfit and MD simulations for Ca^{2+}-bound and Ca^{2+}-unbound states, ensuring each library contains 1,000 conformations. We combined these libraries to obtain a total library of 4,000 conformations. These conformations were then projected onto the same subspace using PCA. Then PCA was performed using singular value decomposition (SVD)[20] on the mean-subtracted C_α coordinates of the combined libraries. We reduced the dimension to three principal components by retaining only the principal components (PCs) that have the most impact on the variance, more precisely the PCs that have an explained variance ratio (i.e. the normalized squared singular values) of more than 10%. To obtain a subspace on a per-atom basis, the eigenvectors were normalized by the number of C_α atoms in the system.

After performing MD simulations, we also conducted the analyses of alpha-actinin conformations obtained from both unipolar and bipolar models using PCA. This approach allowed us to capture their atomic conformational dynamics, enabling an evaluation of the physical motion effects such as bending, twisting,

1573 and rotation of alpha-actinin on fluctuations of the rise or AD in the crosslinked
1574 actin filaments.

1575 ***Analyses of domain distances and twisting and bending angles in alpha-***
1576 ***actinin***

1577 The ABD was divided into two domains: CH1, residue 26-138; CH2, residue
1578 139-251. EF12 is residue 749-818, and EF34 is residue 819-888. The center of C_α
1579 of each domain was used to compute domain distances. Since there are four
1580 centers, there are six distances.

1581 For the analyses of bending and twisting angles, the alpha-actinin was
1582 aligned as described in PCA. The C_α atoms in residue 485-525 were placed on the
1583 xy-plane and their average coordinate was set to be the origin. The rod domain
1584 was placed along the x-axis (**Figure S8A**). The position of the center of C_α atoms
1585 of CH1 and CH2 in one chain and EF12 and EF34 in the other chain is denoted as
1586 (x_1, y_1, z_1) (end 1), and that of the other end (end 2) is denoted as (x_2, y_2, z_2). x_1 is
1587 chosen so that $x_1 > 0$, so $x_2 < 0$. The bending angle for end 1 was calculated by
1588 $\tan^{-1}(z_1/x_1)$, and that for end 2 by $-\tan^{-1}(z_2/x_2)$. In this definition, the bending angles
1589 in alpha-actinin (PDB ID: 1SJJ) were −1.4 and 8.5 degrees.

1590 For the twisting angle calculation, the position of the center of Cα atoms of
1591 CH1 and CH2 at end 1 is denoted as (x_{1c}, y_{1c}, z_{1c}), and that of EF12 and EF34 at
1592 end 1 is denoted as (x_{1e}, y_{1e}, z_{1e}). The twisting angle for end 1 was defined as the
1593 angle between a vector from the center of EF12 and EF34 to the center of CH1
1594 and CH2 in the yz-plane and y axis (**Figure S8B**): that is, $\tan^{-1}((z_{1c} - z_{1e})/(y_{1c} -$
1595 $y_{1e}))$. For end 2, considering the orientation, it was calculated by $\tan^{-1}(-(z_{2c} -$
1596 $z_{2e})/(y_{2c} - y_{2e}))$. When the twisting angle became less than −100 degrees, 360
1597 degrees was added to the angle, since it is a part of the fluctuation over 180
1598 degrees. In this definition, the twisting angles in alpha-actinin (PDB ID: 1SJJ) were
1599 −12.8 and 20.5 degrees.

1600 ***Analyses of half helical pitch, rise and axial distance***

1601 We analyzed HHP, rise, and AD in bare actin filaments and in actin
1602 filaments crosslinked with flexible and frozen alpha-actinin, comprising both bipolar

and unipolar crosslinking models obtained by MD simulations. In the MD simulations of actin filaments, the box along the filaments was allowed to move. The HHP corresponds to the box length along this direction. The rise was defined as the average distance between the centers of mass of two adjacent protomers along the double-strand filament axis. Whereas, the AD was determined as the average distance between the centers of mass between adjacent protomers along the same long-pitch strand or the same protofilament axis (**Figures 6A, C**).

Methods for measuring alpha-actinin crosslinking angles and inter-filament spacing

Alpha-actinin molecules crosslink two actin filaments in either a parallel (unipolar) or anti-parallel (bipolar) configuration. In this study, we analyzed the crosslinking angles (both small and large) relative to the filament axis and inter-filament spacing between actin filaments based on unipolar crosslinking conformations obtained from HS-AFM (**Figure S14**) and based on unipolar and bipolar configurations from MD simulations (**Figures 6A, B**). Two alpha-actinin molecules consistently intercalated between actin filaments at every half-helical turn, forming a parallelogram-like configuration.

To analyze the conformations derived from HS-AFM, we tracked the center of mass (CoM) positions of four crossover points (e.g., A, B, C, and D in **Figure S14A**) in a parallelogram, using their vertex coordinates. This process was performed with the Kodec software to semi-automatically detect the CoM positions (including its source code)[1].

To compute the interior angles of a parallelogram when the vertex coordinates were known, we followed these steps:

Given four vertices—A (x1, y1), B (x2, y2), C (x3, y3), and D (x4, y4)—arranged sequentially around the parallelogram, the first step was to determine the four vectors representing its sides:

$$\overrightarrow{AB} = (x2 - x1), (y2 - y1)$$

$$\overrightarrow{AD} = (x4 - x1), (y4 - y1)$$

$$\overrightarrow{BC} = (x3 - x2), (y3 - y2)$$

$$\overrightarrow{CD} = (x4 - x3), (y4 - y3)$$

Second, the angle between two vectors were calculated as:

Angle at A: between $\overrightarrow{AD}$ and $\overrightarrow{AB}$

Angle at B: between $\overrightarrow{AB}$ and $\overrightarrow{BC}$

Angle at C: between $\overrightarrow{BC}$ and $\overrightarrow{CD}$

Angle at D: between $\overrightarrow{CD}$ and $\overrightarrow{AD}$

For example, an angle θ (rad) at A:

$$\theta = \arccos \frac{(\mathrm{x}2 - x1)(x4 - x1) + (y2 - y1)(y4 - y1)}{\sqrt{(x2 - x1)^2 + (y2 - y1)^2}.\sqrt{(x4 - x1)^2 + (y4 - y1)^2}}$$

The angle (degrees) at A was then calculated:

$$\theta\ (deg) = \theta\ (rad) \frac{180}{\pi}$$

The angles at B, C, and D were calculated using the same approach. Finally, the physical lengths of AB, BC, CD, and DA segments were similarly determined and converted the lengths from pixel to nm unit.

Length of AB segment: $L\ (nm) = \frac{\mathrm{nm*pixel}}{\mathrm{pixel}} \sqrt{(x2 - x1)^2 + (y2 - y1)^2}$

The similar approach was utilized to analyze the unipolar and bipolar crosslinking conformations obtained from MD simulations. We noted that the definition of inter-filament measurements in HS-AFM and MD simulation data differed slightly, as described in their respective captions (**Figure S14**).

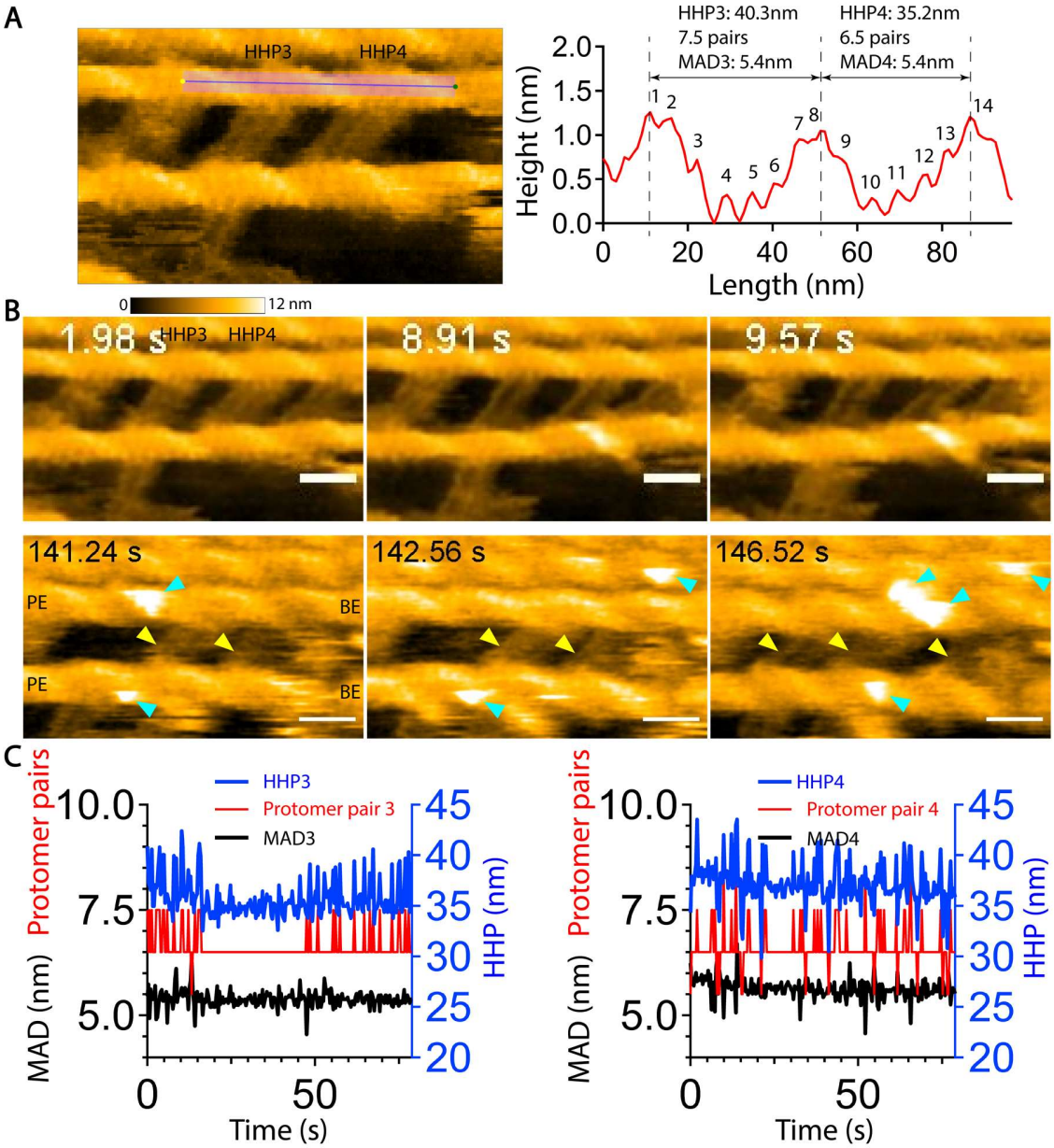

Figure S1 Analysis of the dynamic conformations of actin filaments crosslinked by alpha-actinin in unipolar configuration in the presence of ATP, Ca^{2+}, and S1 using HS-AFM.

(**A**) A longitudinal section profile illustrating for the analysis of two consecutive HHPs, the number of protomer pairs per HHP, and MADs in various actin filaments captured at different time points. The analytic methods used were developed in our previous study[4].

1660 (**B**) Still AFM images with time labels were shown for conditions with ATP present
1661 and after ATP depletion (primarily converted into ADP and inorganic phosphate in
1662 solution) to observe the binding of S1 on actin filaments. As ATP levels gradually
1663 declined or nearly depleted due to ATP hydrolysis (ATP → ADP + Pi) during the
1664 actomyosin reaction, S1 binding to actin filaments persisted for longer durations,
1665 enabling capture by HS-AFM at an imaging rate of 330 ms per frame. All actin
1666 filaments in the imaging field were aligned with the pointed end (PE) on the left
1667 and the barbed end (BE) on the right, reflecting the actual unipolar crosslinking
1668 configuration. As similarly done in our previous study[1] by referring to the EM
1669 study[21], the polarity of actin filaments was confirmed by observing the tilted angles
1670 of S1, with its head pointing toward the pointed (minus) end (PE), resembling an
1671 arrowhead along the filament. This characteristic orientation allowed differentiation
1672 between the PE and the barbed (plus) end (BE). Yellow and cyan arrowheads
1673 indicate alpha-actinin and S1 molecules, respectively. Scale bars: 25 nm. Color
1674 scale: 0-12 nm.
1675 **(C)** Time-dependent changes in two consecutive HHPs, the number of protomer
1676 pairs per HHP, and MADs in actin filaments crosslinked by 50 nM α-actinin in the
1677 presence of 1 mM ATP, 0.1 mM $CaCl_2$, and 1 μM S1, but without $MgCl_2$.
1678 **Related to Figure 3 and Video S2**.
1679
1680
1681
1682
1683
1684
1685
1686
1687
1688
1689

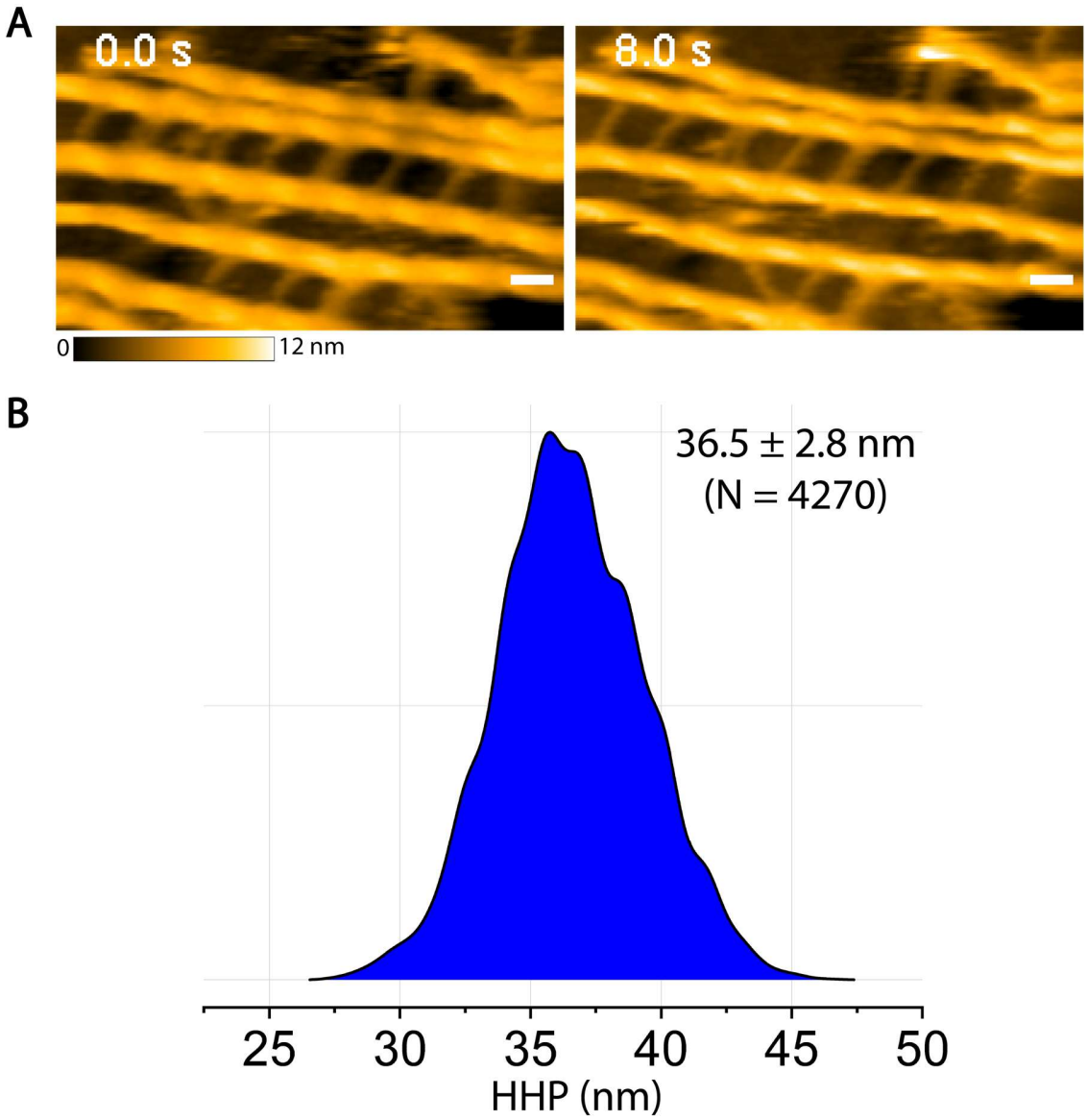

Figure S2 A ridgeline plot illustrating the fluctuation of HHP in actin filaments crosslinked by alpha-actinin.

1693 (**A**) Still AFM images of actin filaments crosslinked using 50 nM alpha-actinin and
1694 imaged in F-buffer with 0.5 mM $MgCl_2$ and 0.5 mM ATP, but without $CaCl_2$. The
1695 polarity of the crosslinking configuration was determined based on a previous
1696 study [22]. Accordingly, the crosslinking of actin filaments by alpha-actinin was
1697 determined as unipolar configuration in this case. It is because no changes were
1698 observed in the preferred attachment angle of the crosslinkers once the filament
1699 spacing stabilized, indicating that the filaments were incorporated in the same
1700 polarity as previously crosslinked filaments (an unipolar configuration). Scale bars:
1701 25 nm. Color scale: 0-12 nm. Related to **Video S3**.
1702 **B**) A histogram of HHP measured for actin filaments crosslinked with alpha-actinin.
1703 A total of 4270 HHPs were counted.
1704
1705
1706

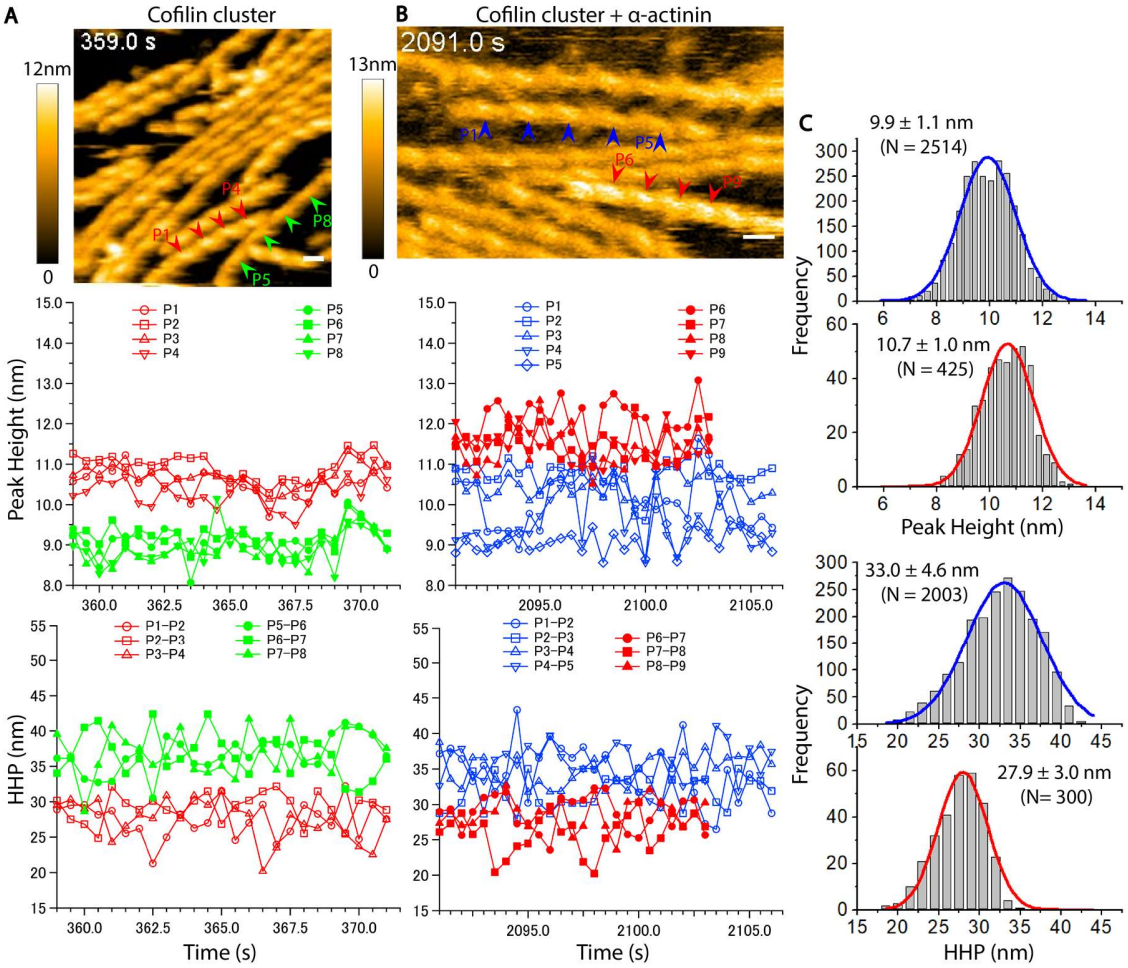

Figure S3 The crosslinking of actin filaments by alpha-actinin inhibits both the development of mature cofilin clusters and shortening of HHP in actin filaments. (**A**) Time-dependent changes in the peak heights and HHPs of actin filaments incubated with only 600 nM hs cofilin 1 and 1mM ATP. A ~25% decrease in HHP and the formation of mature cofilin clusters on actin filaments in the absence of alpha-actinin served as positive controls, providing a basis for comparison with the cofilin clusters and HHP shown in **B**. Red and green arrowheads indicate the peaks in mature cofilin clusters and bare actin segments (served as negative controls), respectively. Time label indicates the time after adding cofilin. Scale bars: 25 nm. Color scale: 0-12 nm. **Related to Video S4A.**

(**B**) Time-dependent changes in the peak heights and HHPs of actin filaments incubated 400 nM α-actinin and 1 mM ATP, and subsequently added with 600 nM cofilin. The cofilin binding and formation of mature cofilin clusters, and the shortening of HHP were significantly suppressed by crosslinking of alpha-actinin. Red arrowheads denote the peaks in mature cofilin clusters within the supertwisted half helices of actin segments (cofilactin) without alpha-actinin, and blue arrowheads indicate those in immature cofilin clusters within the long half helices of actin segments crosslinked with alpha-actinin (cofilactin-actinin), respectively. Scale bars: 25 nm. Color scale: 0-13 nm. **Related to Video S4B.**

(**C**) Histograms of the peak height and HHP measured from various actin filaments with and without alpha-actinin crosslinking, showing the presence of both mature and immature cofilin clusters. These clusters corresponded to short and long HHPs, respectively. Notably, their categorization as mature or immature clusters was based on their differences in peak heights and length of corresponding HHPs, and their comparisons with bare actin (i.e., peak height of 8.6 ± 0.8 nm, HHP of 36.8 ± 4.3 nm), as reported in our previous studies[1]. The mean ± SD heights and lengths are 10.7 ± 1.0 nm (N = 425) and 27.9 ± 3.0 nm (N= 300) for mature clusters of cofilactin segment without alpha-actinin, and 9.9 ± 1.1 nm (N = 2514) and 33.0 ± 4.6 nm (N = 2003) for immature clusters of cofilactin segment with alpha-actinin crosslinking (cofilactin-actinin). A two-population *t-test* ($p < 0.05$) indicates that the differences in height and HHP distribution between the clusters of cofilactin segments without and with alpha-actinin crosslinking are significant ($p = 2.9\times10^{-38}$ for height, $p = 8.5\times10^{-68}$ for HHP).

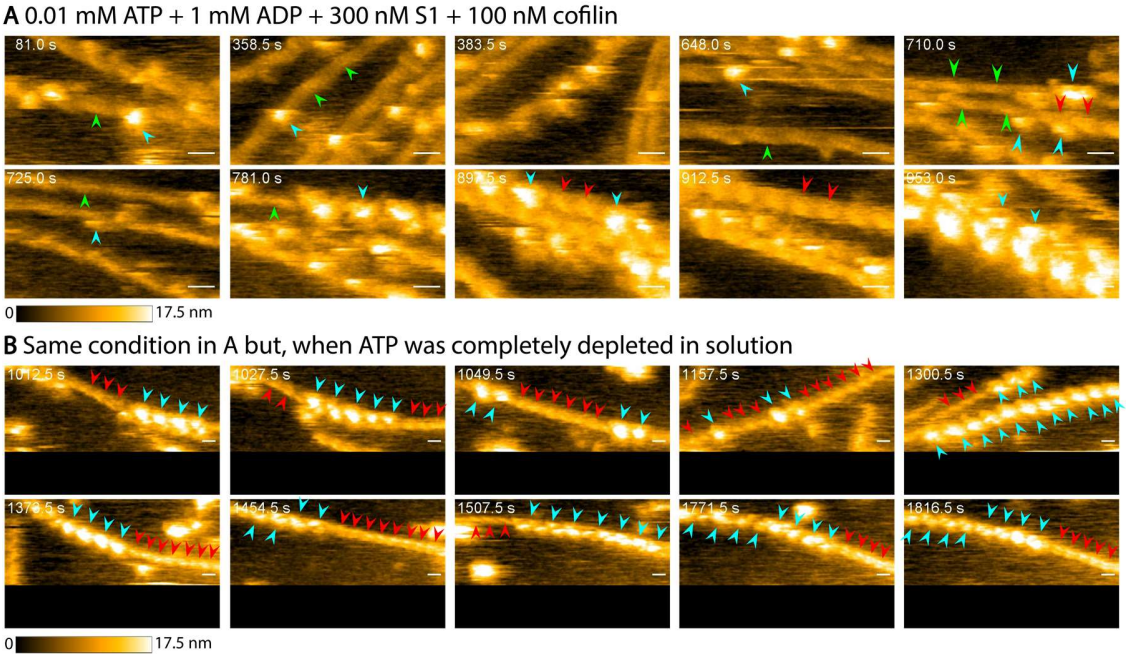

Figure S4 HS-AFM imaging reveals how cofilin and S1 competitively interact, utilizing different HHP structures on the same actin filament to form their respective clusters. Green, cyan, and red arrowheads denote bare actin (lowest height, normal HHP), S1-actin (highest height, normal HHP), and cofilactin (intermediate height between bare actin and S1-actin, with a ~25% reduction in HHP) those are represented in these still AFM images. Actin filaments were initially imaged in F-buffer containing 0.01 mm ATP, 1 mM ADP, and 300 nM S1, followed by adding 100 nM cofilin. As ATP levels gradually declined due to ATP hydrolysis (ATP → ADP + Pi) during the actomyosin reaction, S1 binding to actin filaments persisted for longer durations and formed stable its clusters when ATP was completely depleted. Time indicates the time after adding cofilin before (**A**) and after (**B**) ATP was completely depleted in solution. Scale bars: 25 nm. Color scales: 0-17.5 nm. **Related to Figures S4-S5 and Videos S5 and S6**.

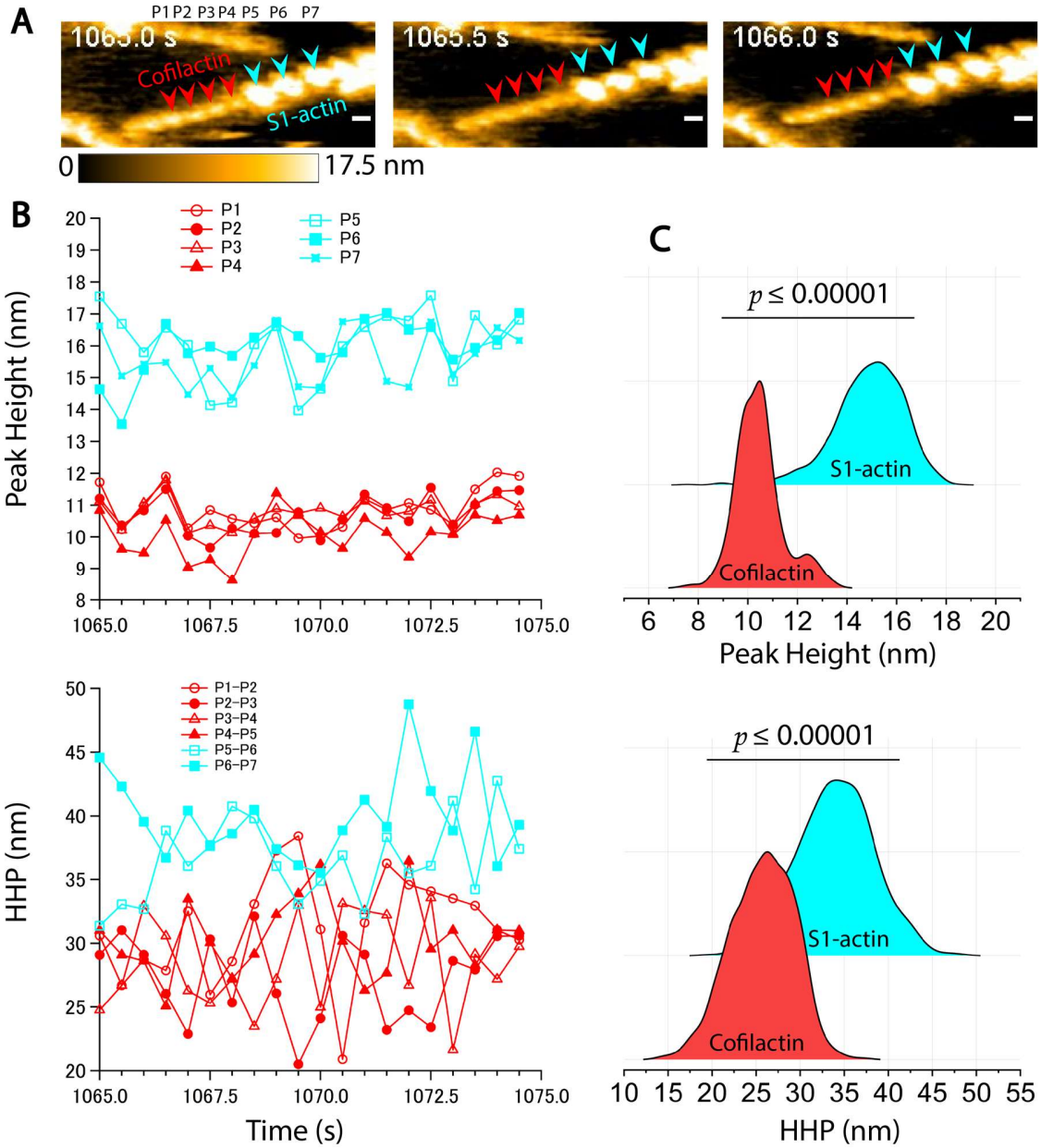

Figure S5 Segregation of cofilin and S1 clusters, as identified by their distinct short and long HHP conformations and corresponding peak-height differences, visualized using HS-AFM.

(A) Still AFM images show actin filaments with distinct short and long HHP regions where cofilin (cofilactin) and S1 (S1-actin) clusters bind. These filaments represented one of the configurations in **Figure S4B**. Red and cyan arrowheads mark cofilactin and S1-actin regions, respectively. Time labels correspond to frames in **Video S6** after the addition of 100 nM cofilin, during which stable S1 clusters were formed near cofilin clusters on actin filaments when ATP levels were depleted. Scale bars: 25 nm. Color scale: 0-17.5 nm.

(B) Time-dependent variations in peak heights and HHP within cofilactin and S1-actin clusters.

(C) Ridgeline plots displaying the distribution of peak heights and HHP in cofilactin and S1-actin cluster regions. The average peak heights (mean ± SD) are 10.5 ± 1.0 nm (N = 935) for cofilactin and 14.9 ± 1.4 nm (N = 1051) for S1-actin segments. The average HHPs (mean ± SD) are 25.7 ± 3.6 nm (N = 767) for cofilactin and 33.9 ± 4.4 nm (N = 805) for S1-actin. Statistical differences between mean values were analyzed using a two-population *t-test* and significant at (p<0.00001).

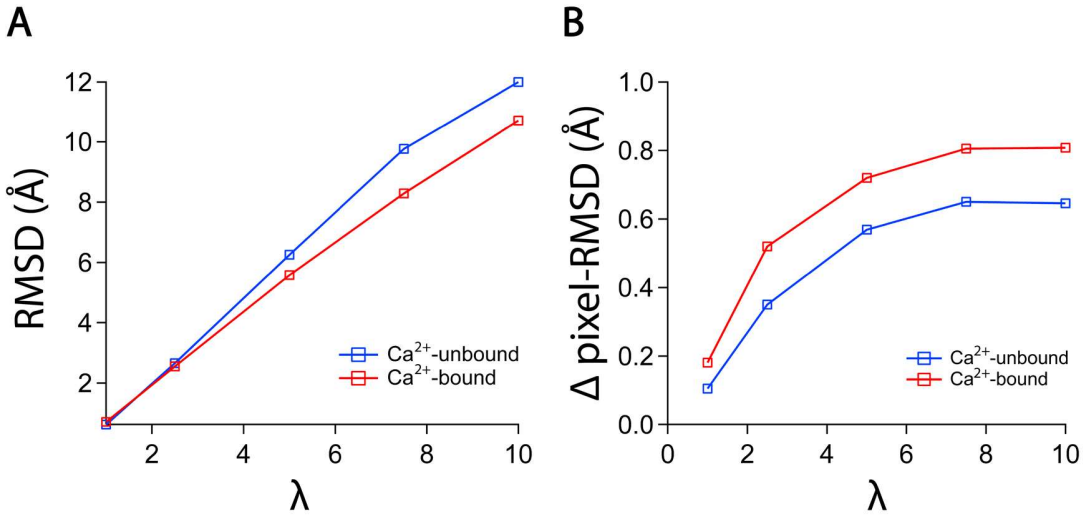

Figure S6 Results of the exhaustive search for the optimal value of a hyperparameter (λ).

(**A**) Average root mean square deviation (RMSD): This represented the average amplitude of the flexible deformation, calculated as the RMSD between the final and initial states. The largest λ value tested that keeps the average RMSD below 10 Å is λ = 7.5.

(**B**) Average Pixel-RMSD Difference: This corresponded to the criterion used by AFMfit to evaluate the goodness of fit. Beyond λ = 7.5, the fitting ceases to improve and reaches a plateau, indicating the onset of overfitting (See Supplementary Methods). **Related to Videos S7-S8.**

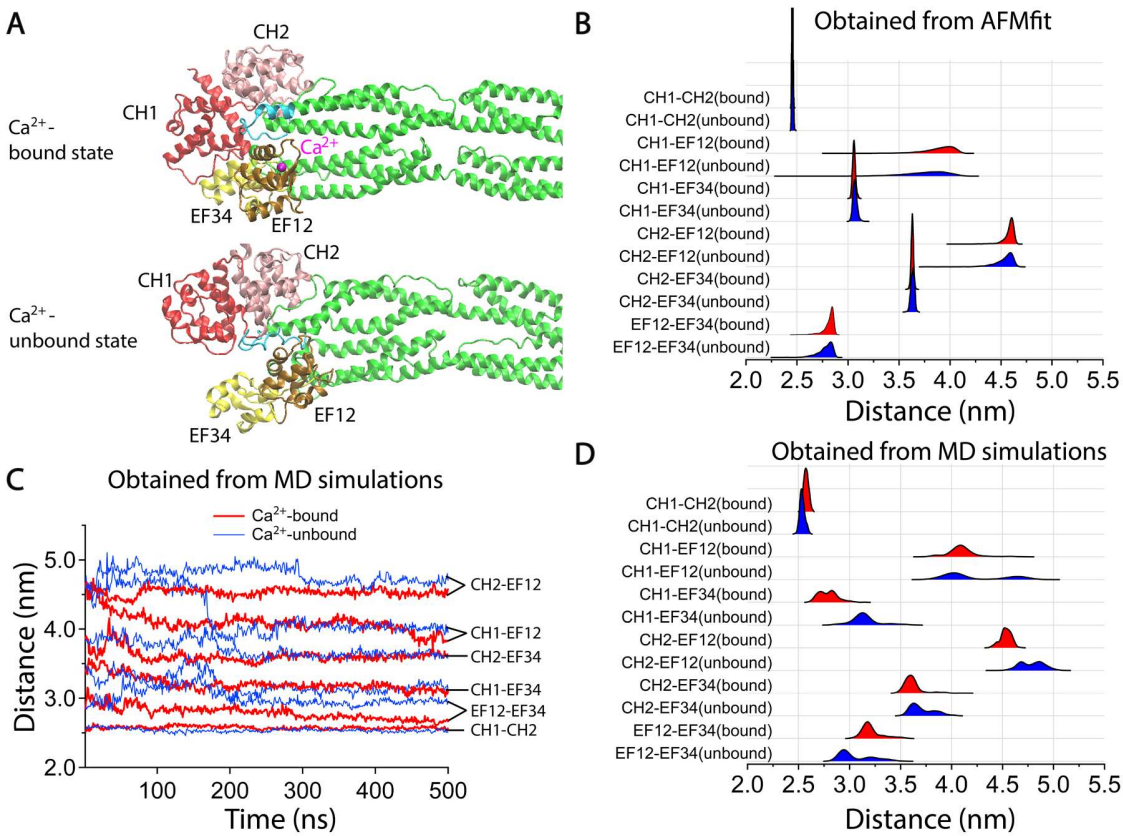

Figure S7 Analysis of domain distances in Ca^{2+}-bound and Ca^{2+}-unbound alpha-actinin based on conformations obtained from AFMfit and MD simulations.

(**A**) Structural comparison of Ca^{2+}-bound and Ca^{2+}-unbound alpha-actinin, showing the positions of the CH1, CH2, EF12, and EF34 domains.

(**B**) Distribution of distances between the CH1, CH2, EF12, and EF34 domains in Ca^{2+}-bound (N = 1466) and Ca^{2+}-unbound (N = 1140) alpha-actinin derived from AFMfit conformations. The domain distances were measured separately for chain 1 and chain 2 in individual conformations (stored as PDB files) for both Ca^{2+}-bound and Ca^{2+}-unbound states. The final data represent the averaged values of the two chains. Related to **Table S5**.

(**C, D**) Time-dependent variations and distributions of domain distances between the CH1, CH2, EF12, and EF34 domains in Ca^{2+}-bound (N = 500) and Ca^{2+}-unbound (N = 500) alpha-actinin, based on conformations from MD simulations. The domain distances were similarly measured for chain 1 and chain 2 in individual conformations for both Ca^{2+}-bound and Ca^{2+}-unbound states. The final data represent the averaged values of the two chains. Related to **Table S5**.

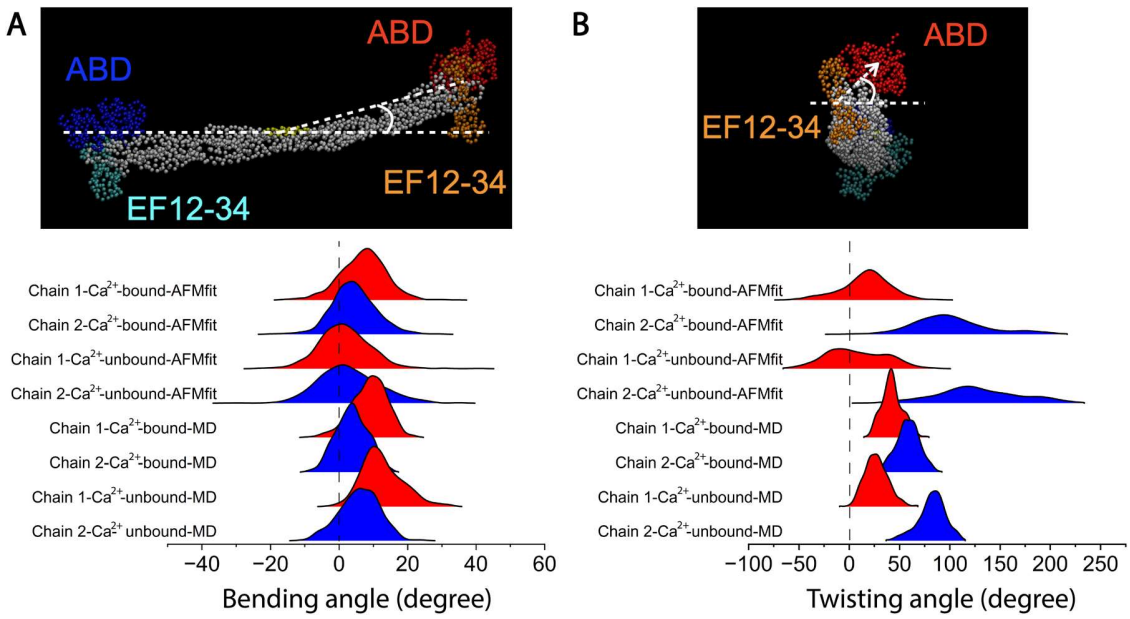

Figure S8 Analysis of the bending and twisting angles of the ABD relative to the rod domain of Ca^{2+}-bound and Ca^{2+}-unbound alpha-actinin using the conformations obtained from (**A**) AFMfit and (**B**) MD simulations (MD). PCA of the conformations confirmed the rigidity of the rod domain (SR2-SR3). To calculate the bending and twisting angles, a reference vector (dashed line) was aligned along the Cα positions within the SR2-SR3 domain, defining 0 degrees. The bending angles were then determined relative to the center of mass of the Cα atoms in the CH1, CH2, EF12, and EF34 domains near the neck domain in chain 1 (red) and chain 2 (blue), as shown in the upper panels (A). For the twisting angles, a vector was defined by connecting the centers of mass of the Cα atoms between the EF12-EF34 and CH1-CH2 domains. These twisting angles were then measured relative to a reference vector aligned along the SR2-SR3 domain, as shown in the upper panel (B). Positive and negative bending or twisting angles corresponded to angles in the upper and lower reference vectors, respectively, for both (A) and (B). A two-population *t-test* was conducted to evaluate the statistical difference ($p < 0.05$) between the mean values of the Ca^{2+}-bound and Ca^{2+}-unbound states. Related to **Table S6**.

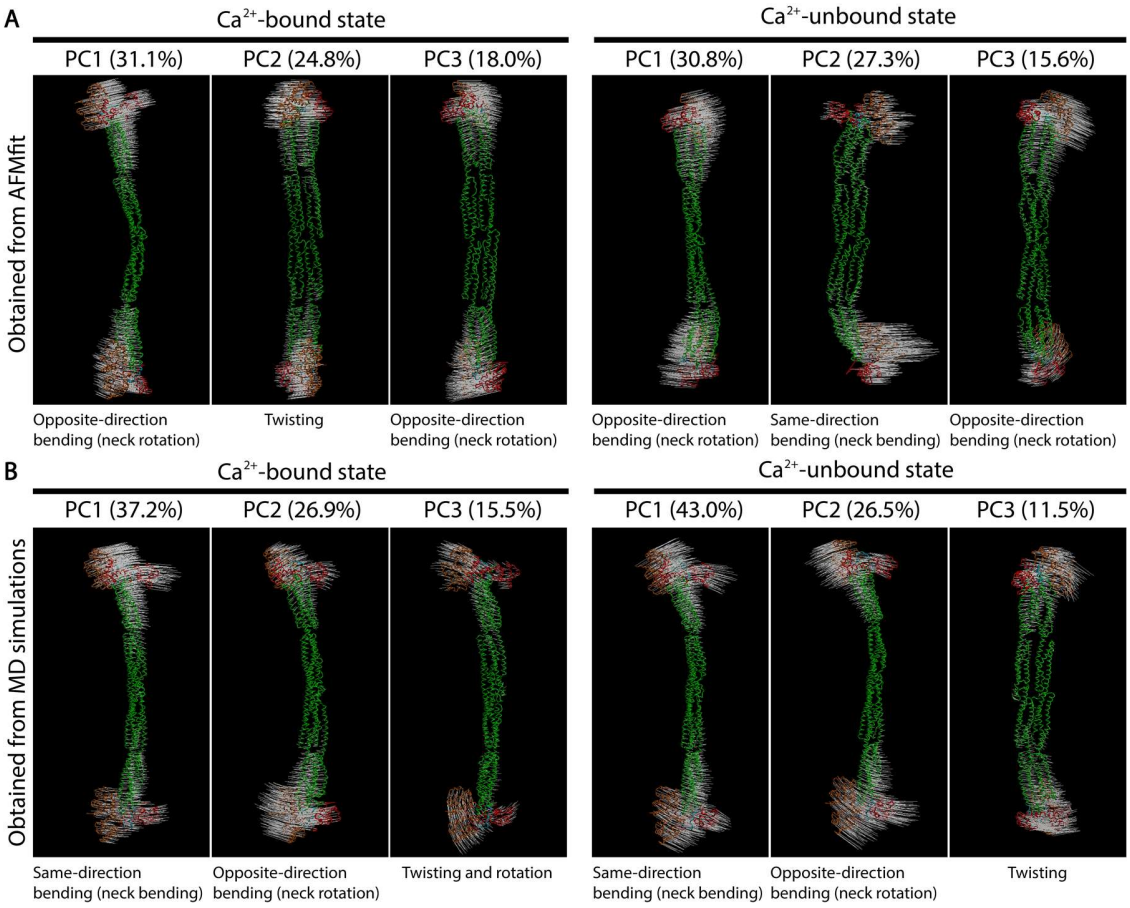

Figure S9 PCA of atomic structures and physical motions of Ca^{2+}-bound and Ca^{2+}-unbound alpha-actinin using conformational libraries obtained from AFMfit and MD simulations. The PCA was conducted using conformations of Ca^{2+}-bound and Ca^{2+}-unbound states, obtained from AFMfit (**A**) and MD simulations (**B**). Eigenvalues of the principal components (PC1, PC2, PC3) were used to calculate the contribution in percentage of each physical motion for these states. The alpha-actinin structures are illustrated in tube conformations, with the ABD, neck, rod, and EF12-EF34 domains represented in red, cyan, green, and yellow, respectively. Eigenvectors indicating the direction of motion are shown with white arrows. Related to **Videos S12-S15**.

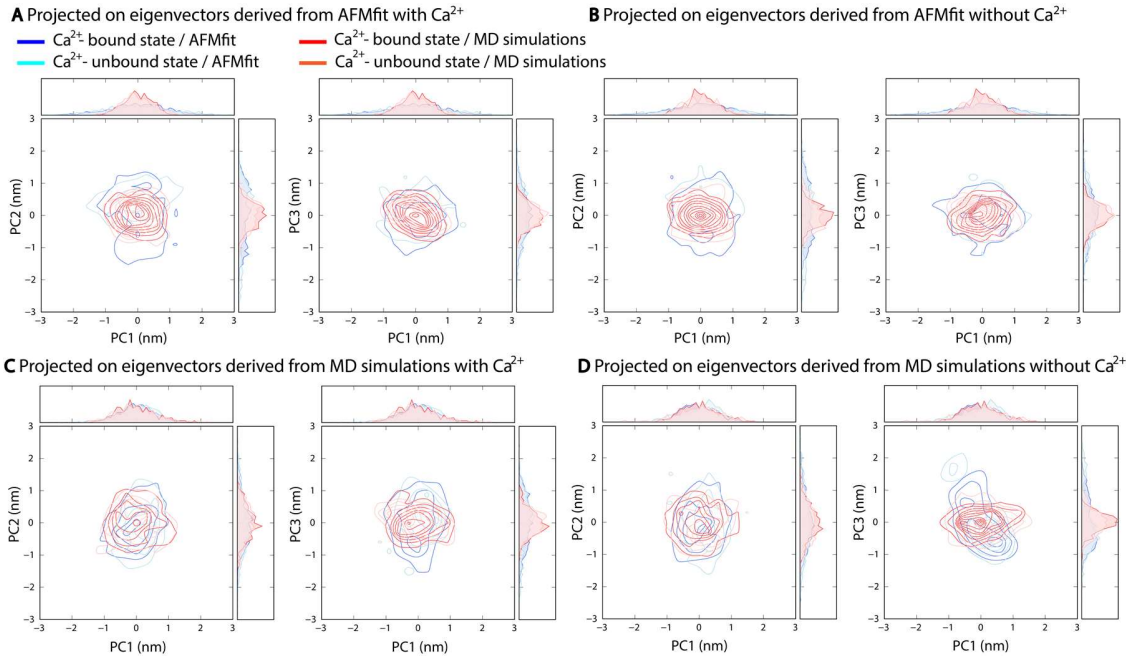

Figure S10 The ensemble motions of atomic conformations and distributions of principal components of alpha-actinin with Ca^{2+}-bound and Ca^{2+}-unbound states obtained from AFMfit and MD simulations projected onto four PCA spaces. All the libraries of conformations with and without Ca^{2+} obtained from AFMfit and MD simulations were projected onto eigenvectors derived from either the data with Ca^{2+} obtained from AFMfit (**A**), or from the data without Ca^{2+} obtained from AFMfit (**B**), or from the data with Ca^{2+} obtained from MD simulations (**C**), or from the data without Ca^{2+} obtained from MD simulations (**D**). The plots in dark blue, light blue, dark red, and light red are the projections of the conformations with Ca^{2+} obtained from AFMfit, without Ca^{2+} obtained from AFMfit, with Ca^{2+} obtained from MD simulations, and without Ca^{2+} obtained from MD simulations, respectively. Related to **Figure S9**.

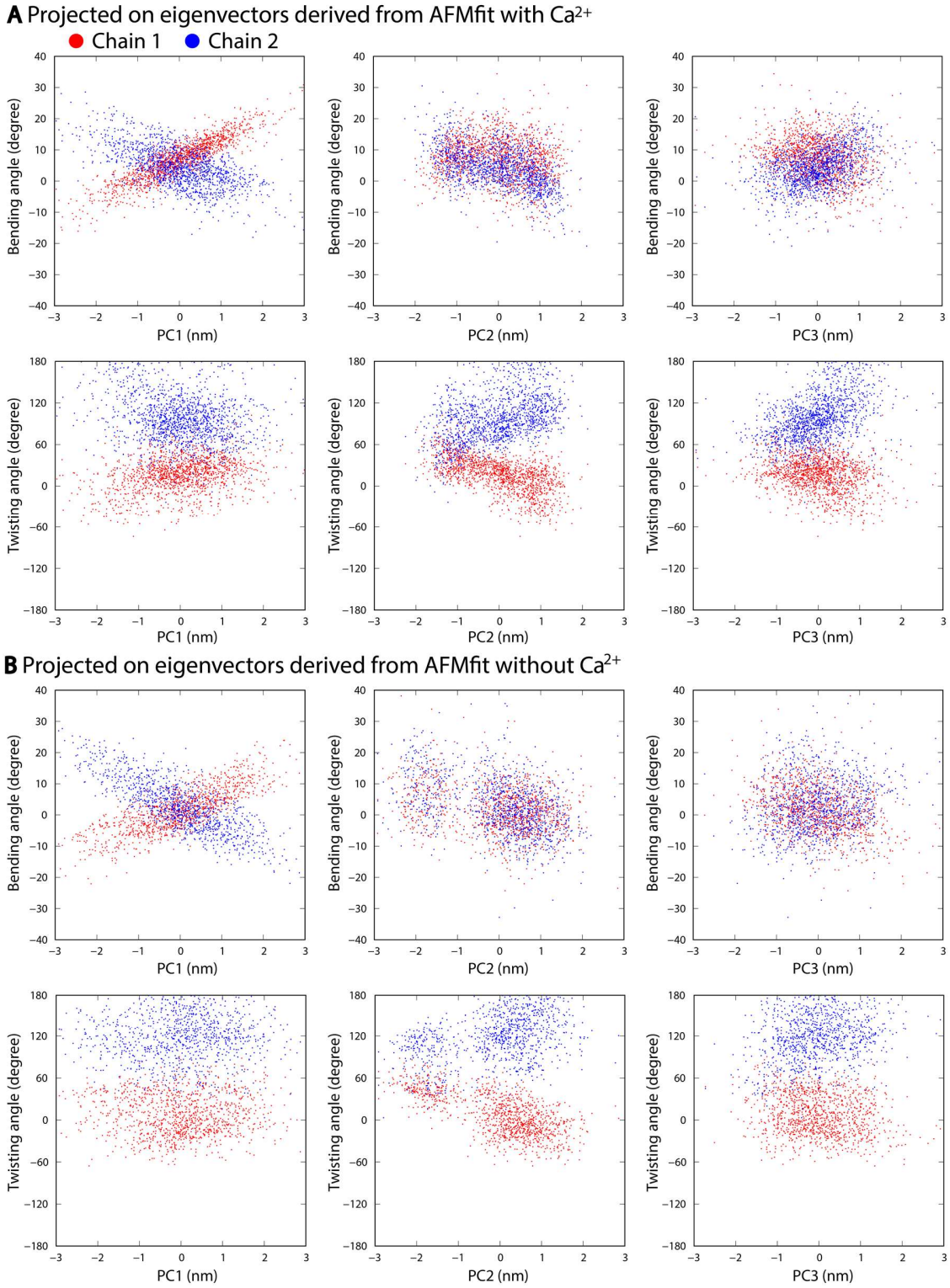
A Projected on eigenvectors derived from AFMfit with Ca2+
Chain 1
Chain 2
Bending angle (degree)
Twisting angle (degree)
PC1 (nm)
PC2 (nm)
PC3 (nm)
B Projected on eigenvectors derived from AFMfit without Ca2+

1916

Figure S11 Correlation between principal components (PC1, PC2, PC3) and bending and twisting angles in Ca^{2+}-bound and Ca^{2+}-unbound alpha-actinin using conformations obtained from AFMfit. Related to **Figures S10A, B**.

(**A, B**) The plots of the correlation between PC1, PC2, PC2 and bending and twisting angles in chain 1 (red dots) and chain 2 (blue dots) of Ca^{2+}-bound and Ca^{2+}-unbound alpha-actinin obtained from AFMfit.

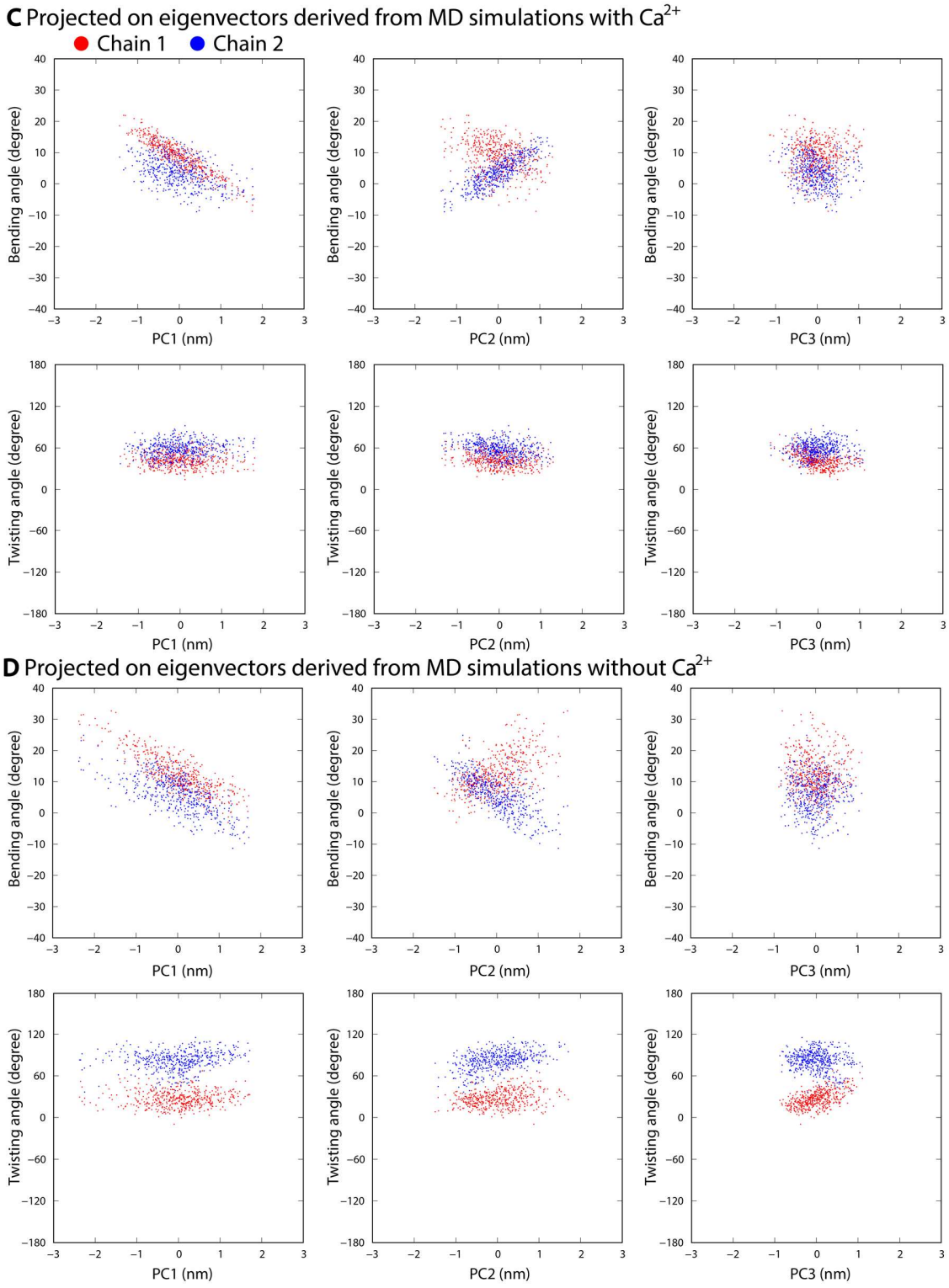
C Projected on eigenvectors derived from MD simulations with Ca2+
Chain 1
Chain 2
Bending angle (degree)
Twisting angle (degree)
PC1 (nm)
PC2 (nm)
PC3 (nm)
D Projected on eigenvectors derived from MD simulations without Ca2+

1947

Figure S12 Correlation between principal components (PC1, PC2, PC3) and bending and twisting angles in Ca^{2+}-bound and unbound alpha-actinin using conformations obtained from MD simulations. Related to **Figures S10C, D**.

(**C, D**) The plots of the correlation between PC1, PC2, PC2 and bending and twisting angles in chain 1 (red dots) and chain 2 (blue dots) of Ca^{2+}-bound and Ca^{2+}-unbound alpha-actinin obtained from MD simulations.

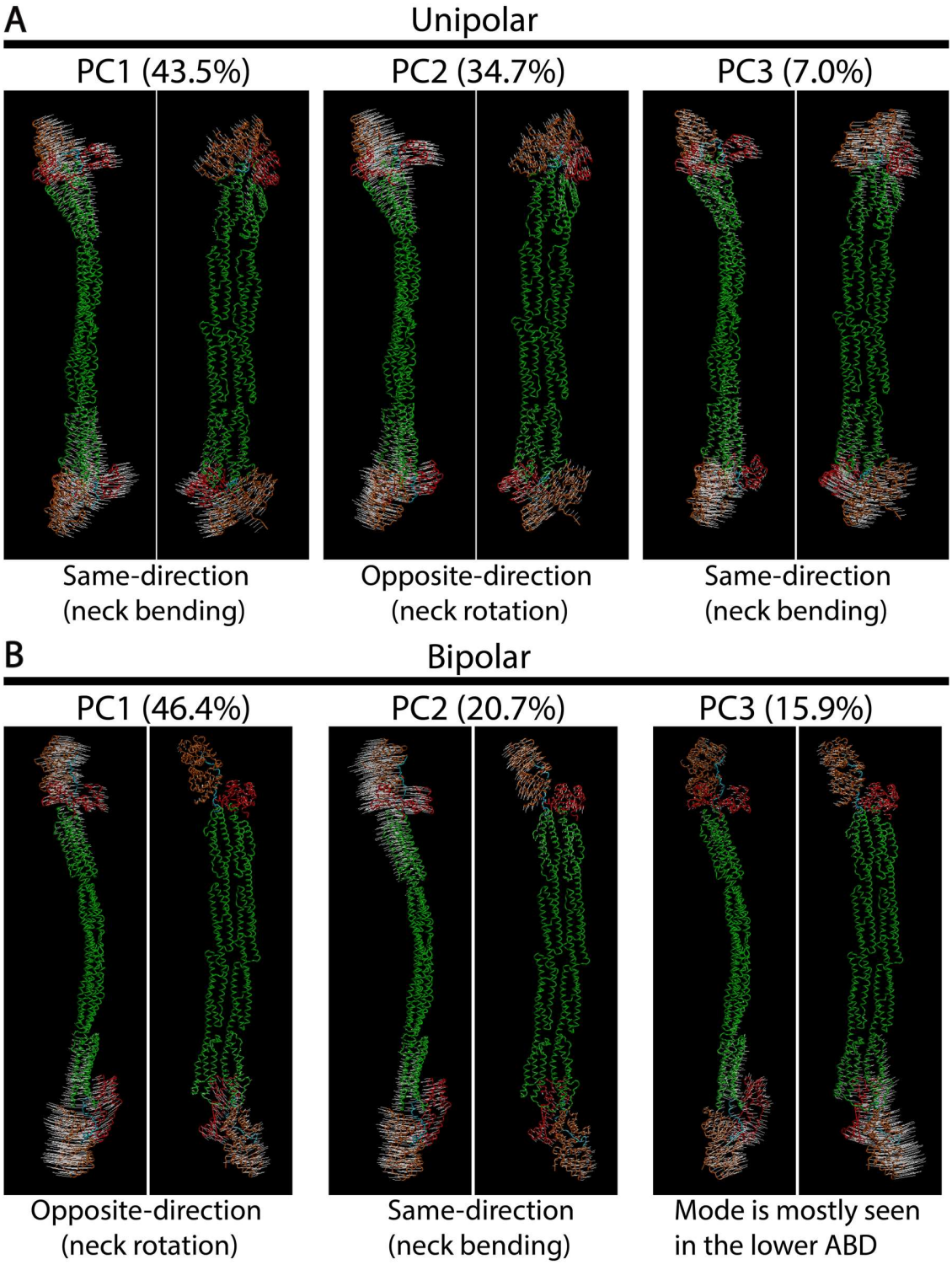
A
Unipolar
PC1 (43.5%)
PC2 (34.7%)
PC3 (7.0%)
Same-direction
(neck bending)
Opposite-direction
(neck rotation)
Same-direction
(neck bending)
B
Bipolar
PC1 (46.4%)
PC2 (20.7%)
PC3 (15.9%)
Opposite-direction
(neck rotation)
Same-direction
(neck bending)
Mode is mostly seen
in the lower ABD

1978

1979 **Figure S13** PCA of the atomic structures and physical motions of alpha-actinin
1980 molecules on the basis of conformational libraries derived from unipolar (**A**) and
1981 bipolar (**B**) crosslinking models obtained with MD simulations. The alpha-actinin
1982 structures are illustrated in tube conformations, with the ABD, neck, rod, and EF12-
1983 EF34 domains represented in red, cyan, green, and yellow, respectively.
1984 Eigenvectors indicating the direction of motion are shown with white arrows. The
1985 final system of unipolar configurations consisted of two actin fibers (26 protomers),
1986 one alpha-actinin molecule, 1032 K^+ atoms, 718 Cl^- atoms, 26 Mg^{2+} atoms, 26 ADP
1987 molecules, and 1,433,011 water molecules, for a total number of 4,479,739 atoms
1988 in the system. The bipolar model was constructed similarly, differing only in the
1989 inclusion of 1,432,853 water molecules (see Supplementary Methods). Related to
1990 **Videos S16-S17**.
1991
1992
1993
1994
1995
1996
1997
1998
1999
2000
2001
2002
2003
2004
2005
2006
2007
2008

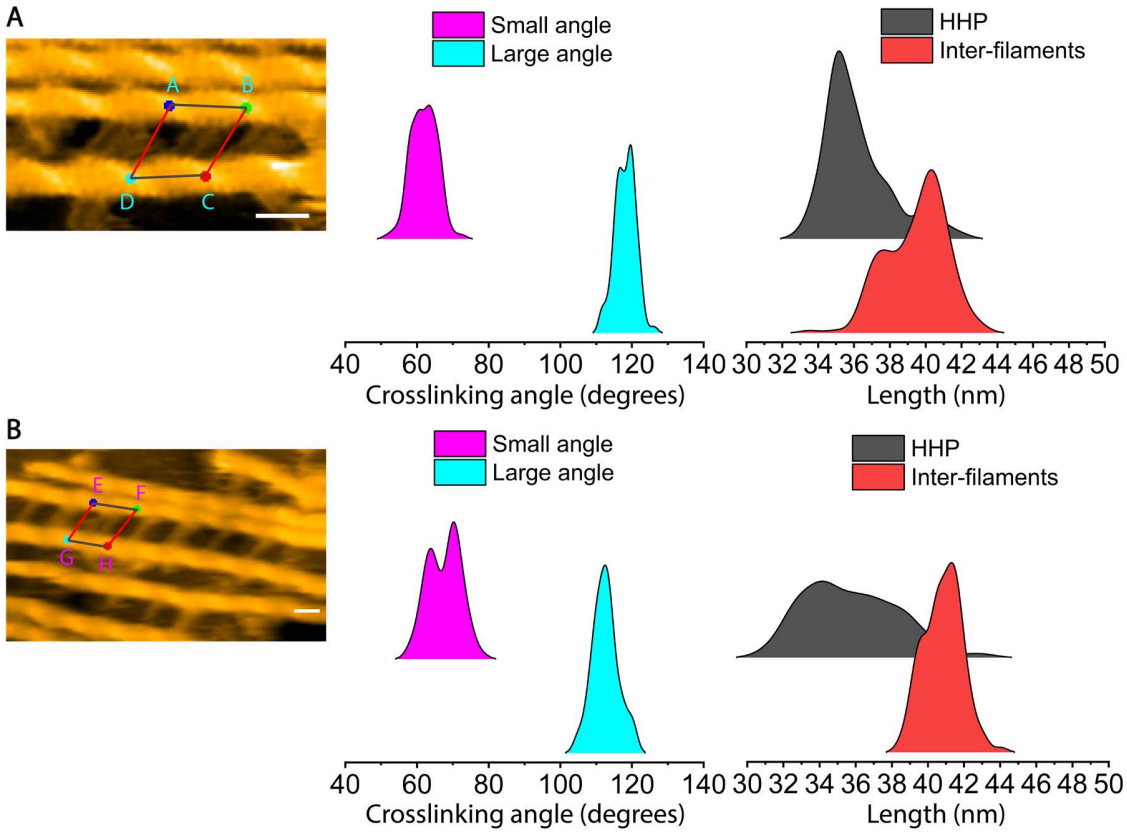
A
A
B
D
C
Small angle
Large angle
HHP
Inter-filaments
40 60 80 100 120 140
Crosslinking angle (degrees)
30 32 34 36 38 40 42 44 46 48 50
Length (nm)
B
E
F
G
H
Small angle
Large angle
HHP
Inter-filaments
40 60 80 100 120 140
Crosslinking angle (degrees)
30 32 34 36 38 40 42 44 46 48 50
Length (nm)

2009

2010 **Figure S14** Quantitative analysis of spacious inter-filament lengths, HHP, and
2011 alpha-actinin crosslinking angles relative to the filament axis, based on
2012 experimental HS-AFM data for actin filaments crosslinked by alpha-actinin, both in
2013 the presence (A) and absence (B) of S1. In our HS-AFM data, alpha-actinin
2014 crosslinked the actin filaments in a unipolar configuration. Two alpha-actinin
2015 molecules consistently intercalated between actin filaments at every half-helical
2016 turn, forming a parallelogram-like configuration. The segments AB, CD, EF, and
2017 HG correspond to HHP, while AD, BC, EG, and FH represent inter-filament spaces
2018 or lengths. It is noted that the definition of inter-filament spacing differs slightly from
2019 that in the MD simulation data (**Figure 6B**). In the MD simulation, spacing was
2020 measured by a vertical line connecting between the two filaments, whereas in the
2021 AFM data, it is determined by measuring the parallel sides of a parallelogram. As
2022 a result, the inter-filament lengths measured in AFM data were larger than that in
2023 MD simulations. Statistical differences were assessed using a two-population t-
2024 test, with a significant difference confirmed at $p \leq 0.05$. See our analysis in
2025 Supplementary Methods for details. Related to **Figures 3, S1, S2, Table S8, and**
2026 **Videos S2–S3**.
2027
2028 **Table S1** Summary of the height and length (mean ± SD) distributions of ABDs in
2029 Ca^{2+}-bound and Ca^{2+}-unbound alpha-actinin analyzed using conformations
2030 obtained from HS-AFM, AFMfit, and MD simulations. ND: not determined.
2031 Statistical differences were assessed using a two-population *t-test*, with a
2032 significant difference confirmed at $p \leq 0.05$. Related to **Figure 2.**

	Height (nm) (N)	Length (nm) (N)
Ca^{2+}-bound state (HS-AFM)	6.3 ± 0.9 (7236)	25.2 ± 2.3 (3516)
Ca^{2+}-unbound state (HS-AFM)	5.5 ± 0.8 (4043)	25.6 ± 3.6 (2016)
p-value (*t-test*) (HS-AFM)	0	7.45454×10^{-7}
Ca^{2+}-bound state (AFMfit)	ND	24.7 ± 0.9 (1466)
Ca^{2+}-unbound state (AFMfit)	ND	25.2 ± 1.4 (1140)
p-value (*t-test*) (AFMfit)	ND	8.98×10^{-28}
Ca^{2+}-bound state (MD simulations)	ND	25.4 ± 0.6 (500)
Ca^{2+}-unbound state (MD simulations)	ND	24.1 ± 0.7 (500)
p-value (*t-test*) (MD simulations)	ND	0

2033

2034 **Table S2** A brief comparison of structure, localization, and functions of actin
2035 filaments crosslinked by alpha-actinin in bipolar and unipolar configurations within
2036 cells[21–25]. Related to **Figure 7B**.

Feature	Bipolar configuration	Unipolar configuration
Polarity	Opposite at each end	All barbed (plus) ends face the same direction
Crosslinking by alpha-actinin	Forms contractile networks	Forms stable, non-contractile bundles
Myosin interaction	Strong (contractile activity)	Weak (non-contractile activity)
Cellular function	Force generation, contraction	Protrusion, structural support, migration
Localization in cells	Stress fibers, contractile rings, sarcomeres	Lamellipodia, filopodia, cortical actin, microvilli

2037

2038 **Table S3** Summary of the peak height and HHP (mean ± SD) in mature cofilin
2039 clusters (cofilactin) without alpha-actinin and immature cofilin clusters within actin
2040 segments crosslinked with alpha-actinin (cofilactin-actinin). Statistical differences
2041 were assessed using a two-population *t-test*, with a significant difference confirmed
2042 at $p \leq 0.05$. Related to **Figure S3C.**

Clusters of	Height (nm) (N)	HHP (nm) (N)
Cofilactin	10.7 ± 1.0 (425)	27.9 ± 3.0 (300)
Cofilactin-actinin	9.9 ± 1.1 (2514)	33 ± 4.6 (2003)
p-value (*t-test*)	2.9×10^{-38}	8.5×10^{-68}

2043

2044 **Table S4** Summary of the peak height and HHP (mean ± SD) in cofilin clusters
2045 (cofilactin) and S1 clusters (S1-actin) formed and segregated on the same actin
2046 filaments. Statistical differences between the mean values were assessed using a
2047 two-population *t-test*, with a significant difference confirmed at $p \leq 0.05$. Related to
2048 **Figure S5C**.

Clusters of	Peak Height (nm) (N)	HHP (nm) (N)
S1-actin	14.9 ± 1.4 (1051)	33.9 ± 4.4 (805)
Cofilactin	10.5 ± 1.0 (935)	25.7 ± 3.6 (767)
p-value (*t-test*)	0	3.3×10^{-245}

2049

2050 **Table S5** Summary of the distances between domains (mean ± SD) in Ca^{2+}-bound
2051 and Ca^{2+}-unbound alpha-actinin, derived from conformational libraries obtained
2052 from AFMfit and MD simulations. The domain distances were measured separately
2053 for chain 1 and chain 2 in individual conformations (stored as PDB files) for both
2054 Ca^{2+}-bound and Ca^{2+}-unbound states. The final data represent the averaged
2055 values of the two chains. A two-population *t-test* was conducted to evaluate the
2056 statistical difference ($p \leq 0.05$) between the mean values of the Ca^{2+}-bound and
2057 Ca^{2+}-unbound states. **Related to Figure S7.**

Domain distance (nm)	Ca^{2+}-bound/ AFMfit	Ca^{2+}-unbound/ AFMfit	*t-test* (*p*-value)
CH1-CH2	2.45 ± 0.01	2.46 ± 0.01	4.6×10^{-10}
CH1-EF12	3.89 ± 0.16	3.76 ± 0.21	1.9×10^{-62}
CH1-EF34	3.06 ± 0.01	3.07 ± 0.02	8.7×10^{-38}
CH2-EF12	4.58 ± 0.06	4.53 ± 0.09	1.8×10^{-49}
CH2-EF34	3.63 ± 0.01	3.63 ± 0.02	1.5×10^{-08}
EF12-EF34	2.81 ± 0.05	2.78 ± 0.07	7.7×10^{-48}
N	1466	1140	
Domain distance (nm)	Ca^{2+}-bound/ MD simulations	Ca^{2+}-unbound/ MD simulations	*t-test* (*p*-value)
CH1-CH2	2.58 ± 0.02	2.54 ± 0.03	7.0×10^{-105}
CH1-EF12	4.10 ± 0.15	4.22 ± 0.30	9.7×10^{-15}
CH1-EF34	2.79 ± 0.09	3.15 ± 0.14	1.4×10^{-260}
CH2-EF12	4.53 ± 0.06	4.79 ± 0.12	2.9×10^{-237}
CH2-EF34	3.62 ± 0.09	3.71 ± 0.12	2.4×10^{-42}
EF12-EF34	3.21 ± 0.10	3.06 ± 0.16	1.0×10^{-61}
N	500	500	

2059 **Table S6** Summary of the bending and twisting angles of the ABD (mean ± SD)
2060 near the neck domain relative to the rod domain in Ca^{2+}-bound and Ca^{2+}-unbound
2061 alpha-actinin, derived from conformational libraries obtained from AFMfit and MD
2062 simulations. A two-population *t-test* was conducted to evaluate the statistical
2063 difference ($p \leq 0.05$) between the mean values of the Ca^{2+}-bound and Ca^{2+}-
2064 unbound states obtained from AFMfit or MD simulations. **Related to Figure S8**.

Figure S8A	Bending angle (degree)	N	*p*-value
Chain 1-Ca^{2+}-bound-AFMfit	7.0 ± 6.7	1466	2.7×10^{-28}
Chain 2-Ca^{2+}-bound-AFMfit	4.3 ± 6.5	1466	4.7×10^{-7}
Chain 1-Ca^{2+}-unbound-AFMfit	1.7 ± 7.7	1140	2.7×10^{-28}
Chain 2-Ca^{2+}-unbound-AFMfit	2.8 ± 8.9	1140	4.7×10^{-7}
Chain 1-Ca^{2+}-bound-MD simulations	8.8 ± 5.1	500	2.8×10^{-25}
Chain 2-Ca^{2+}-bound-MD simulations	3.8 ± 4.6	500	4.6×10^{-11}
Chain 1-Ca^{2+}-unbound-MD simulations	12.6 ± 6.0	500	2.8×10^{-25}
Chain 2-Ca^{2+}-unbound-MD simulations	6.0 ± 5.8	500	4.6×10^{-11}
Figure S8B	Twisting angle (degree)	N	*p*-value
Chain 1-Ca^{2+}-bound-AFMfit	16.7 ± 24.6	1466	6.8×10^{-18}
Chain 2-Ca^{2+}-bound-AFMfit	101.2 ± 37.5	1466	9.7×10^{-66}
Chain 1-Ca^{2+}-unbound-AFMfit	7.5 ± 29.4	1140	6.8×10^{-18}
Chain 2-Ca^{2+}-unbound-AFMfit	128.6 ± 41.5	1140	9.7×10^{-66}
Chain 1-Ca^{2+}-bound-MD simulations	42.7 ± 10.4	500	2.8×10^{-25}
Chain 2-Ca^{2+}-bound-MD simulations	58.4 ± 11.3	500	6.7×10^{-142}
Chain 1-Ca^{2+}-unbound-MD simulations	27.0 ± 11.6	500	2.8×10^{-25}
Chain 2-Ca^{2+}-unbound-MD simulations	82.1 ± 13.5	500	6.7×10^{-142}

2065

2066 **Table S7** Summary of HHP, rise, and AD (mean ± SD) values measured from bare
2067 actin filaments and actin filaments in bipolar-flexible, bipolar-fixed, and unipolar-
2068 flexible models conducted by MD simulations. The statistical difference ($p \leq 0.05$)
2069 between the values of bare actin filaments and their conformations in the unipolar
2070 and bipolar models was assessed using a one-way *ANOVA* and a two-population
2071 *t-test*. Related to **Figure 6C.**

Model	HHP (nm)	Rise (nm)	AD (nm)
Bare actin	36.2 ± 0.0 (N = 14)	2.8 ± 0.1 (N = 33)	5.6 ± 0.1 (N = 34)
Bipolar-flexible	36.3 ± 0.0 (N = 14)	2.8 ± 0.2 (N = 58)	5.7 ± 0.2 (N = 59)
Bipolar-fixed	36.3 ± 0.0 (N = 13)	2.9 ± 0.2 (N = 81)	5.7 ± 0.2 (N = 78)
Unipolar-flexible	36.2 ± 0.0 (N = 14)	2.8 ± 0.1 (N = 42)	6.0 ± 0.3 (N = 37)
One-way ANOVA (*p*-value) for all values	1.9×10^{-14}	0.00325	2.6×10^{-5}
Bare actin vs. bipolar-flexible, *t-test* (*p*-value)	0.00158	0.87644	0.00158
Bare actin vs. bipolar-fixed, *t-test* (*p*-value)	5.6×10^{-5}	0.02016	5.6×10^{-5}
Bare actin vs. unipolar-flexible, *t-test* (*p*-value)	0.02957	0.34058	0.02957
Bipolar-flexible vs. unipolar-flexible, *t-test* (*p*-value)	7.9×10^{-4}	0.33007	0.11681

Bipolar-flexible vs. Bipolar-fixed, *t-test* (*p*-value)	0.34514	0.0043	0.0681
Unipolar-flexible vs. Bipolar-fixed, *t-test* (*p*-value)	6.1×10^{-5}	0.057	0.00413

Table S8 A summary of alpha-actinin crosslinking angles relative to the filament axis and inter-filament spaces or lengths of actin filaments crosslinked by alpha-actinin, as determined from MD simulation experiments. Statistical differences were assessed using a two-population *t-test*, with a significant difference confirmed at ($p \leq 0.05$). Related to **Figure 6B**.

Figure 6B (MD simulations)	Inter-filament length (nm)(mean ± SD)	Crosslinking angle (degrees) (mean ± SD)
Bipolar-flexible	35 ± 0.5 (N = 6100)	68.4 ± 3.3 (N = 6100)
Bipolar-fixed	20.2 ± 0.4 (N = 10000)	42.9 ± 0.0 (N = 10000)
Unipolar-flexible	32.4 ± 0.8 (N = 6100)	75.0 ± 2.0 (N = 6100)
One-way ANOVA (*p*-value)	0	0

2078 **Table S9** A summary of alpha-actinin crosslinking angles relative to the filament
2079 axis, HHP, and inter-filament spaces or lengths of actin filaments crosslinked by
2080 alpha-actinin, as determined from HS-AFM experiments. Statistical differences
2081 were assessed using a two-population *t-test*, with a significant difference confirmed
2082 at ($p \leq 0.05$). Related to **Figure S14**.

Figure S14A (HS-AFM)	Mean ± SD	N	*t-test* (*p*-value)
Small angle (degrees)	61.2 ± 3.6	200	1.4×10^{-28}
Large angle (degrees)	118.1 ± 2.8	200	2.9×10^{-41}
HHP (nm)	36.2 ± 1.8	200	0.05
Inter-filament length (nm)	39.5 ± 1.7	200	1.7×10^{-14}
Figure S14B (HS-AFM)	Mean ± SD	N	*t-test* (*p*-value)
Small angle (degrees)	67.6 ± 4.5	124	1.4×10^{-28}
Large angle (degrees)	112.5 ± 3.6	124	2.9×10^{-41}
HHP (nm)	35.7 ± 2.5	124	0.05
Inter-filament length (nm)	40.8 ± 1.1	124	1.7×10^{-14}

2083

2084 **Table S10** A summary of residue-level contact probability maps between alpha-
2085 actinin and actin subunits, derived from all-atom MD simulations using three
2086 crosslinking models. The unipolar-flexible crosslinking model represents parallel
2087 actin filaments with the same polarity, crosslinked by alpha-actinin, which flexibly
2088 adjusted their conformation during simulations. In contrast, the bipolar-flexible and
2089 bipolar-fixed crosslinking models describe anti-parallel actin filaments with
2090 opposite polarity, also crosslinked by alpha-actinin, but either allowing flexible
2091 conformational changes or maintaining fixed Cα positions during simulations. This

2092 crucial biochemical data, computed by all-atoms MD simulations, can be served
2093 as a foundational source for further biochemical experiments aimed at
2094 investigating the binding residues in unipolar and bipolar crosslinking models
2095 within cells. Key amino acid residues involved in contacts with a probability greater
2096 than 0.9 were highlighted in green for alpha-actinin and in red for actin. Related to
2097 **Figure 6D**.

Alpha-actinin	Actin	Unipolar-flexible	Bipolar-flexible	Bipolar-fixed
Leu26	Asp56	0.919180	0.656393	
Leu26	Asn92			0.339100
Leu26	Glu93	1.535082	0.386230	
Asp27	Asn92			0.688600
Asp27	Arg95	0.830000		
Ala29	Lys50		0.311148	
Glu31	Arg95		0.728852	
Arg87	Gln354	0.339344		
Lys107	Glu99	0.316557		
Ser110	Arg95	1.065246		
Ser110	Glu99		1.124098	
Lys122	Glu57	0.651639		
Glu144/	Thr5	0.526721		
Glu144	Thr6	0.470820		
Thr145	Ala22	0.446230		
Ser146	Arg95		0.687705	
Glu149	Arg28		0.510492	0.669700
Glu149	Arg95		1.750000	0.573700
Glu226	Ser350		0.388033	
Arg233	Asp25	1.443115		

Arg233	Asp56			0.882200
Arg233	Glu57		0.787869	
Arg233	Glu167			1.600600
Asp235	Arg96		0.516066	
Glu236	Arg28	1.119016		
Glu236	Arg95	1.585246		1.740300
Asp842	Thr5		0.327213	
Arg866	Glu364		0.340820	

2098 **Video S1** HS-AFM imaging of structure and dynamic conformational changes of
2099 Ca^{2+}-bound and Ca^{2+}-unbound alpha-actinin in solution. The AFM images were
2100 smoothed with Gaussian filter (σ = 1). Imaging rate was done at 100 ms per frame.
2101 Video plays at 5 fps. Scale bars: 25 nm. Related to **Figure 2**.
2102 **Video S2** HS-AFM imaging of the dynamic conformational changes in actin
2103 filaments crosslinked by alpha-actinin in the presence of ATP, Ca^{2+}, and S1. Actin
2104 filaments were incubated with 50 nM α-actinin under conditions containing 1 mM
2105 ATP, 0.1 mM $CaCl_2$, and 1 μM S1, but without $MgCl_2$. As ATP levels gradually
2106 declined or nearly depleted due to ATP hydrolysis (ATP → ADP + Pi) during the
2107 actomyosin reaction, S1 binding to actin filaments persisted for longer durations,
2108 enabling capture by HS-AFM at an imaging rate of 330 ms per frame. All actin
2109 filaments in the imaging field were aligned with the pointed end (PE) on the left
2110 and the barbed end (BE) on the right, reflecting the actual unipolar crosslinking
2111 configuration. The polarity of actin filaments was determined using S1, as similarly
2112 done in our previous study[1] by referring to the EM study[21]. The AFM images were
2113 processed using a Gaussian filter (σ = 1). The Video plays at 5 frames per second.
2114 Scale bar: 25 nm. Related to **Figures 3 and S1**.
2115 **Video S3** HS-AFM imaging of the dynamic conformational changes in actin
2116 filaments crosslinked by alpha-actinin in the presence of ATP and Mg^{2+}. Actin
2117 filaments were crosslinked with 50 nM alpha-actinin and observed in F-buffer
2118 supplemented with 0.5 mM $MgCl_2$ and 0.5 mM ATP, but without $CaCl_2$. The AFM
2119 images were recorded at an imaging rate of 500 ms per frame and processed using
2120 a Gaussian filter (σ = 1). The Video plays at 5 frames per second. Scale bar: 25
2121 nm. Related to **Figure S2**.

2122 **Video S4** HS-AFM analysis of helical structures in actin filaments without and with
2123 alpha-actinin crosslinking. Actin filaments were gently immobilized on a lipid
2124 membrane and imaged in F-buffer containing 1 mM ATP, 600 nM hs cofilin, and
2125 either (A) without or (B) with 400 nM alpha-actinin. Alpha-actinin crosslinking was
2126 found to suppress the shortening of half helices and the formation of mature cofilin
2127 clusters. AFM images were captured at an imaging rate of 500 ms per frame and
2128 processed with a Gaussian filter (σ = 1). Time labels indicate the elapsed time after
2129 cofilin addition. The Video plays at 5 frames per second. Scale bar: 25 nm. Related
2130 to **Figure S3**.
2131 **Video S5** HS-AFM imaging was conducted to explore the competitive interactions
2132 between cofilin and S1, focusing on how they utilize distinct helical structures on
2133 the same actin filament to form their respective clusters. Actin filaments were
2134 gently immobilized on a lipid membrane and imaged in F-buffer initially containing
2135 1 mM ADP, 0.01 mM ATP and followed by the addition of 100 nM cofilin. When
2136 ATP was gradually or nearly depleted, stable S1 clusters were formed near cofilin
2137 clusters on actin filaments. AFM images were acquired at a rate of 500 ms per
2138 frame and processed using a Gaussian filter (σ = 1). Time labels indicate the
2139 elapsed time after cofilin addition. The Video plays at 5 frames per second, with a
2140 scale bar of 25 nm. Related to **Figure S4**.
2141 **Video S6** HS-AFM imaging was performed to observe actin filaments utilizing
2142 distinct shorter and longer half-helices for the binding of cofilin clusters and S1
2143 clusters, respectively. Actin filaments were gently immobilized on a lipid membrane
2144 and imaged in F-buffer initially containing 1 mM ADP, 0.01 mM ATP, and 300 nM
2145 S1, followed by the addition of 100 nM cofilin. As ATP levels completely depleted,
2146 stable S1 clusters formed in proximity to cofilin clusters on the same actin
2147 filaments. AFM images were recorded at a rate of 500 ms per frame and processed
2148 using a Gaussian filter (σ = 1). Time labels indicate the elapsed time after cofilin
2149 addition. The Video plays at 5 frames per second. Scale bar: 25 nm. Related to
2150 **Figure S5A**.

2151 **Video S7** The HS-AFM Videos of Ca^{2+}-bound alpha-actinin (left) and the atomic
2152 model (right) that were obtained through rigid and flexible fitting using AFMfit. The
2153 initial model of the Ca^{2+}-bound state was constructed based on PDB entry 1SJJ.
2154 Related to **Figure 4A**.
2155 **Video S8** The HS-AFM Videos of Ca^{2+}-unbound alpha-actinin (left) and the atomic
2156 model (right) that were obtained through rigid and flexible fitting using AFMfit. The
2157 initial model of the Ca^{2+}-unbound state was generated based on PDB entry 1SJJ.
2158 Related to **Figure 4A**.
2159 **Video S9** PC1 captured the ensemble of opposite-direction bending motions or
2160 neck rotation. Related to **Figure 5**.
2161 **Video S10** PC2 represented same-direction bending motions or neck bending.
2162 Related to **Figure 5**.
2163 **Video S11** PC3 described a combination of opposite-direction bending and
2164 twisting motions. Related to **Figure 5**.
2165 **Video S12** PC1, PC2, PC3 described physical motions Ca^{2+}-bound alpha-actinin
2166 obtained from AFMfit. Related to **Figure S9A**.
2167 **Video S13** PC1, PC2, PC3 described physical motions Ca^{2+}-unbound alpha-
2168 actinin obtained from AFMfit. Related to **Figure S9A**.
2169 **Video S14** PC1, PC2, PC3 described physical motions Ca^{2+}-bound alpha-actinin
2170 obtained from MD simulations. Related to **Figure S9B**.
2171 **Video S15** PC1, PC2, PC3 described physical motions Ca^{2+}-unbound alpha-
2172 actinin obtained from MD simulations. Related to **Figure S9B**.
2173 **Video S16** PC1, PC2, PC3 described physical motions Ca^{2+}-unbound alpha-
2174 actinin, as derived from unipolar crosslinking model obtained from MD simulations.
2175 Related to **Figure S13A**.
2176 **Video S17** PC1, PC2, PC3 described physical motions Ca^{2+}-unbound alpha-
2177 actinin, as derived from bipolar crosslinking model obtained from MD simulations.
2178 Related to **Figure S13B**.

Video S18 Molecular dynamics of unipolar-flexible crosslinking model obtained from MD simulations. All atoms were allowed to flexibly vibrate in the model and MD simulations were carried out for 100 ns. With fewer residue contacts locating in different domains on both sides of actin subunits than in the bipolar-flexible and bipolar-fixed models, alpha-actinin-unbound Ca^{2+} appeared to promote greater same-direction neck bending (PC1 + PC3: 50.5%) than opposite-direction neck rotation (PC2: 34%) in the unipolar-flexible model. This suggests that alpha-actinin's bending or rotation may have minimal impact on fluctuations in rise and AD in the unipolar model compared to the two bipolar models, which displayed stronger residue interactions. Moreover, the rise fluctuations were nearly identical to those observed in the bare actin filament, but AD fluctuations were significantly different ($p \leq 0.05$). **Note**: The simulation box remained unchanged. Consequently, slight drifting of the model in the box may cause the actin protomer to move in or out of the box. Related to **Figures 6, S13, Table S10**.

Video S19 Molecular dynamics of bipolar-flexible crosslinking model obtained from MD simulations. All atoms were allowed to flexibly vibrate in the model and MD simulations were carried out for 100 ns. With higher residue contacts locating in different domains on both sides of actin subunits than and different locations in the unipolar-flexible model, alpha-actinin-unbound Ca^{2+} appeared to induce greater opposite-direction neck rotation (PC1: 46.4%) than same-direction neck bending (PC2: 20.7%) in the bipolar-flexible model. This suggests that neck rotation in alpha-actinin has a stronger physical impact on fluctuations in rise and AD, whereas the unipolar-flexible model exhibited weaker fluctuations in this motion. It is possible that certain key contacting residues contribute to this effect, warranting further investigation in future studies. Additionally, the rise and AD fluctuations were higher than those observed in the bare actin filament. **Note**: The simulation box remained unchanged. Consequently, slight drifting of the model in the box may cause the actin protomer to move in or out of the box. Related to **Figures 6, S13, Table S10**.

2208 **Video S20** Molecular dynamics of bipolar-fixed crosslinking model obtained from
2209 MD simulations. In the model, all Cα atoms in alpha-actinin were computationally
2210 constrained to prevent vibrations, and MD simulations were performed for 100 ns.
2211 With higher residue contacts locating in different domains on both sides of actin
2212 subunits than and different locations in the unipolar-flexible model, alpha-actinin-
2213 unbound Ca^{2+} exhibited highly rigid in the bipolar-fixed model. This explains that
2214 strong binding of alpha-actinin to actin subunits in the bipolar model was sufficient
2215 to increase fluctuations in the rise and AD as compared to the unipolar-flexible
2216 model, which exhibited weaker residue interactions. Additionally, the rise and AD
2217 fluctuations were higher than those observed in the bare actin filament. **Note**: The
2218 simulation box remained unchanged. Consequently, slight drifting of the model in
2219 the box may cause the actin protomer to move in or out of the box. Related to
2220 **Figures 6, S13, Table S10**.
2221

2222 **Supplementary References**

2223 1. Ngo, K.X., Kodera, N., Katayama, E., Ando, T., and Uyeda, T.Q. (2015).
2224 Cofilin-induced unidirectional cooperative conformational changes in actin
2225 filaments revealed by high-speed atomic force microscopy. Elife *4*, 1–22.
2226 https://doi.org/10.7554/eLife.04806.
2227 2. Ribeiro, E.D.A., Pinotsis, N., Ghisleni, A., Salmazo, A., Konarev, P. V.,
2228 Kostan, J., Sjöblom, B., Schreiner, C., Polyansky, A.A., Gkougkoulia, E.A.,
2229 et al. (2014). The structure and regulation of human muscle α-Actinin. Cell
2230 *159*, 1447–1460. https://doi.org/10.1016/j.cell.2014.10.056.
2231 3. Tetsuya Asakawa, N.A. (1988). Preparation of Subfragment-1 from Abalone
2232 Smooth Muscle Myosin. *103*, 667–671.
2233 4. Ngo, K.X., Vu, H.T., Umeda, K., Trinh, M.-N., Kodera, N., and Uyeda, T.
2234 (2024). Deciphering the actin structure dependent preferential cooperative
2235 binding of cofilin. Elife *13*, 1–37. https://doi.org/10.7554/eLife.95257.
2236 5. Ando, T., Uchihashi, T., and Kodera, N. (2013). High-speed AFM and
2237 applications to biomolecular systems. Annu. Rev. Biophys. *42*, 393–414.

https://doi.org/10.1146/annurev-biophys-083012-130324.

6. Vuillemot, R., Pellequer, J., and Grudinin, S. (2024). AFMfit : Deciphering conformational dynamics in AFM data using fast nonlinear NMA and FFT-based search. bioRxiv. https://doi.org/10.1101/2024.06.03.597083.

7. Liu, J., Taylor, D.W., and Taylor, K.A. (2004). A 3-D reconstruction of smooth muscle α-actinin by CryoEm reveals two different conformations at the actin-binding region. J. Mol. Biol. *338*, 115–125. https://doi.org/10.1016/j.jmb.2004.02.034.

8. Hoffmann, A., and Grudinin, S. (2017). NOLB: Nonlinear Rigid Block Normal-Mode Analysis Method. J. Chem. Theory Comput. *13*, 2123–2134. https://doi.org/10.1021/acs.jctc.7b00197.

9. Tian, C., Kasavajhala, K., Belfon, K.A.A., Raguette, L., Huang, H., Migues, A.N., Bickel, J., Wang, Y., Pincay, J., Wu, Q., et al. (2020). Ff19SB: Amino-Acid-Specific Protein Backbone Parameters Trained against Quantum Mechanics Energy Surfaces in Solution. J. Chem. Theory Comput. *16*, 528–552. https://doi.org/10.1021/acs.jctc.9b00591.

10. William L. Jorgensen, Jayaraman Chandrasekhar, and J.D.M. (1983). Comparison of simple potential functions for simulating liquid water. J. Chem. Phys. *79*, 926–935. https://doi.org/10.1080/00268977700101881.

11. Li, P., Song, L.F., and Merz, K.M. (2015). Systematic parameterization of monovalent ions employing the nonbonded model. J. Chem. Theory Comput. *11*, 1645–1657. https://doi.org/10.1021/ct500918t.

12. Li, P., and Merz, K.M. (2014). Taking into account the ion-induced dipole interaction in the nonbonded model of ions. J. Chem. Theory Comput. *10*, 289–297. https://doi.org/10.1021/ct400751u.

13. Berendsen, H.J.C., Postma, J.P.M., Van Gunsteren, W.F., Dinola, A., and Haak, J.R. (1984). Molecular dynamics with coupling to an external bath. J. Chem. Phys. *81*, 3684–3690. https://doi.org/10.1063/1.448118.

14. Ryckaert, J.P., Ciccotti, G., and Berendsen, H.J.C. (1977). Numerical integration of the cartesian equations of motion of a system with constraints:

molecular dynamics of n-alkanes. J. Comput. Phys. *23*, 327–341. https://doi.org/10.1016/0021-9991(77)90098-5.

15. Essmann, U., Perera, L., Berkowitz, M.L., Darden, T., Lee, H., and Pedersen, L.G. (1995). A smooth particle mesh Ewald method. J. Chem. Phys. *103*, 8577–8593. https://doi.org/10.1063/1.470117.
16. Kanematsu, Y., Narita, A., Oda, T., Koike, R., Ota, M., Takano, Y., Moritsugu, K., Fujiwara, I., Tanaka, K., Komatsu, H., et al. (2022). Structures and mechanisms of actin ATP hydrolysis. Proc. Natl. Acad. Sci. U. S. A. *119*, 1–12. https://doi.org/10.1073/pnas.2122641119.
17. Reynolds, M.J., Hachicho, C., Carl, A.G., Gong, R., and Alushin, G.M. (2022). Bending forces and nucleotide state jointly regulate F-actin structure. Nature. https://doi.org/10.1038/s41586-022-05366-w.
18. Meagher, K.L., Redman, L.T., and Carlson, H.A. (2003). Development of polyphosphate parameters for use with the AMBER force field. J. Comput. Chem. *24*, 1016–1025. https://doi.org/10.1002/jcc.10262.
19. Andrej Sali, T.L.B. (1993). Comparative Protein Modelling by Satisfaction of Spatial Restraints. J. Mol. Biol. *234*, 779–815.
20. Wall, M.E., Rechtsteiner, A., and Rocha, L.M. (2005). Singular Value Decomposition and Principal Component Analysis. In A Practical Approach to Microarray Data Analysis, pp. 91–109. https://doi.org/10.1007/0-306-47815-3_5.
21. David A. Begg, Richard Rodewald, L.I.R. (1978). The VISUALIZATION OF ACTIN FILAMENT POLARITY IN THIN SECTIONS Evidence for the Uniform Polarity of Membrane-Associated Filaments. J. Cell Biol. *79*, 846–852.
22. Taylor, K.A., Taylor, D.W., and Schachat, F. (2000). Isoforms of α-actinin from cardiac, smooth, and skeletal muscle form polar arrays of actin filaments. J. Cell Biol. *149*, 635–645. https://doi.org/10.1083/jcb.149.3.635.
23. Hampton, C.M., Taylor, D.W., and Taylor, K.A. (2007). Novel structures for α-actinin: F-actin interactions and their implications for actin-membrane

attachment and tension sensing in the cytoskeleton. J. Mol. Biol. *368*, 92–104.

24. Tojkander, S., Gateva, G., and Lappalainen, P. (2012). Actin stress fibers - Assembly, dynamics and biological roles. J. Cell Sci. *125*, 1855–1864. https://doi.org/10.1242/jcs.098087.

25. Rajan, S., Kudryashov, D.S., and Reisler, E. (2023). Actin Bundles Dynamics and Architecture. Biomolecules *13*. https://doi.org/10.3390/biom13030450.